ELECTROCHEMICAL PERFORMANCE OF BINDER-FREE POLYANILINE BASED ELECTRODE FOR SUPERCAPACITOR APPLICATION

SYAZA AMIRA BINTI RAZALI

FACULTY OF SCIENCE
UNIVERSITY OF MALAYA
KUALA LUMPUR

2019

ELECTROCHEMICAL PERFORMANCE OF BINDER-FREE POLYANILINE BASED ELECTRODE FOR SUPERCAPACITOR APPLICATION

SYAZA AMIRA BINTI RAZALI

DISSERTATION SUBMITTED IN FULFILMENT OF THE REQUIREMENTS FOR THE DEGREE OF MASTER

DEPARTMENT OF PHYSICS
FACULTY OF SCIENCE
UNIVERSITY OF MALAYA
KUALA LUMPUR

2019

UNIVERSITY OF MALAYA

ORIGINAL LITERARY WORK DECLARATION

Name: **SYAZA AMIRA BINTI RAZALI**

Registration/Matric No: **SGR 150088**

Name of Degree: **MASTER OF SCIENCE**

Title of Project Paper/Research Report/Dissertation/Thesis ("this Work"):

ELECTROCHEMICAL PERFORMANCE OF BINDER-FREE POLYANILINE BASED ELECTRODE FOR SUPERCAPACITOR APPLICATION

Field of Study: **EXPERIMENTAL PHYSICS**

I do solemnly and sincerely declare that:

(1) I am the sole author/writer of this Work;
(2) This Work is original;
(3) Any use of any work in which copyright exists was done by way of fair dealing and for permitted purposes and any excerpt or extract from, or reference to or reproduction of any copyright work has been disclosed expressly and sufficiently and the title of the Work and its authorship have been acknowledged in this Work;
(4) I do not have any actual knowledge nor do I ought reasonably to know that the making of this work constitutes an infringement of any copyright work;
(5) I hereby assign all and every rights in the copyright to this Work to the University of Malaya ("UM"), who henceforth shall be owner of the copyright in this Work and that any reproduction or use in any form or by any means whatsoever is prohibited without the written consent of UM having been first had and obtained;
(6) I am fully aware that if in the course of making this Work I have infringed any copyright whether intentionally or otherwise, I may be subject to legal action or any other action as may be determined by UM.

Candidate's Signature Date:

Subscribed and solemnly declared before,

Witness's Signature Date:

Name:

Designation:

ELECTROCHEMICAL PERFORMANCE OF BINDER FREE POLYANILINE BASED ELECTRODE FOR SUPERCAPACITOR APPLICATION

ABSTRACT

This project focuses on improving the cycle stability of composite electrode consisting of conducting polymer and metal oxides. Two electrode systems were fabricated, namely polyaniline and polyaniline-nickel oxide composite (PANI and NiO-PANI) deposited on etched carbon cloth. PANI was deposited on electro-etched carbon fiber cloth by simple chronoamperometry electrodeposition method with various applied potentials. The results demonstrate that the effects of applied deposition potential significantly influence the electrochemical performance of electrodes. From the first electrode system, deposited PANI on etched carbon cloth at 1.4 V exhibited optimum specific capacitance of 357.14 F g^{-1}. The energy density and power density was 40.18 mW h kg^{-1} and 1.28 W kg^{-1} respectively at current density of 200 mA g^{-1} in 0.5 M H_2SO_4 electrolyte. Symmetrical cell was also assembled and showed good specific capacitance retention of 88% after 2000 cycles with PVA+0.5 M H_2SO_4 electrolyte at current density of 200 mA g^{-1}. In order to enhance the cycle stability and reversibility of deposited PANI on etched carbon cloth electrode, NiO was introduced by conventional heating process at different temperatures. The optimum performance of NiO-PANI on etched carbon cloth electrode was achieved when the heating temperature of 300 °C was applied. The specific capacitance obtained was 192.39 F g^{-1} at current density of 200 mA g^{-1} in 0.5 M H_2SO_4. The symmetrical cell employing NiO-PANI on etched carbon cloth electrode exhibited good electrochemical reversibility when discharged at different current densities over 4500 cycles. The cell was able to retain 72% of its initial specific capacitance after undergone various current density. The cell successfully restored 13.87 mW h kg^{-1} of its energy density after 4500 cycles. The preparation of electrodes in this work using electrodeposition method is

simple, low-cost, and environmental-friendly. It holds great potential to produce cost-effective and high energy density supercapacitors.

Keywords: supercapacitor, polyaniline, nickel oxide, electrodeposition, hydrothermal, gel polymer electrolyte

PRESTASI ELEKTROKIMIA ELEKTROD BERASASKAN POLIANILIN BEBAS PENGIKAT UNTUK APLIKASI SUPERKAPASITOR

ABSTRAK

Projek ini memfokuskan pada peningkatan kestabilan kitaran elektrod komposit yang terdiri daripada polimer konduktif dan logam oksida. Dua sistem elektrod telah dihasilkan, iaitu polianilin dan komposit polianilin-nikel oksida (PANI dan NiO-PANI) yang didepositkan pada permukaan kain karbon. PANI didepositkan pada kain karbon dengan kaedah elektrodeposisi kronoamperometri dengan menggunakan beberapa nilai potensi. Keputusan kajian menunjukkan bahawa kesan yang terhasil antara potensi pemendapan yang digunakan dengan ketara mempengaruhi prestasi elektrokimia elektrod superkapasitor. Berdasarkan sistem elektrod pertama, PANI didepositkan pada kain karbon dengan menggunakan potensi 1.4 V menunjukkan kapasitan spesifik optimum sebanyak 357.14 F g^{-1}. Ketumpatan tenaga dan ketumpatan kuasa masing-masing adalah 40.18 mW h kg^{-1} dan 1.28 W kg^{-1} pada ketumpatan arus 200 mA g^{-1} dalam elektrolit 0.5 M asid sulfurik. Sel simetri telah dipasang dan mempamerkan 95% daripada kapasitif spesifik dapat dikekalkan selepas 1000 kitaran dalam elektrolit polivinil alkohol dan 0.5 M asid sulfurik pada ketumpatan arus 200 mA g^{-1}. Sel simetri juga telah dipasang dan mempamerkan pengekalan sebanyak 88% kadar kapasitan spesifik selepas 2000 kitaran menggunakan elektrolit PVA+0.5 M pada ketumpatan arus 200 mA g^{-1}. Untuk meningkatkan kestabilan dan kebolehulangan semula kitaran elektrod PANI pada kain karbon, nikel oksida diperkenalkan melalui proses pemanasan konvensional pada suhu berbeza. Prestasi optimum elektrod NiO-PANI pada kain karbon diperoleh dengan menggunakan suhu pemanasan 300 ° C. Kapasitan spesifik yang diperoleh adalah 192.39 F g^{-1} pada ketumpatan arus 200 mA g^{-1} dalam 0.5 M asid sulfurik. Sel simetri yang direka menggunakan elektrod NiO-PANI pada kain karbon juga memperlihatkan

kemerosotan elektrokimia yang sedikit apabila dinyahcas pada ketumpatan arus yang berbeza untuk 4500 kitaran. 72% daripada kapasiti awal dapat dikekalkan selepas melalui ketumpatan arus berbeza. Sel tersebut berjaya mengekalkan 13.87 mW h kg^{-1} ketumpatan tenaga selepas 4500 kitaran. Penyediaan elektrod dalam kajian ini menggunakan kaedah elektrodeposisi yang mudah, murah, dan mesra alam sekitar. Oleh yang demikian, ia berpotensi besar untuk menghasilkan superkapasitor yang kos efektif dan berketumpatan tenaga tinggi.

Kata kunci: superkapasitor, polianilin, nikel oksida, elektrodeposit, hidrotermal, elektrolit polimer gel

ACKNOWLEDGEMENTS

First of all, I would like to show my earnest respect and gratitude to my supervisor Assoc. Prof Dr. Siti Rohana Majid for her continues guidance, patience, advice and warm encouragement. She imparts her knowledge and experience to me and gives me good suggestions in my experiments, manuscript and thesis preparation.

I also want thank my fellow members of Center for Ionics University of Malaya (CIUM), Dr. Farhana, Dr. Rusi, Dr. Chan Pei Yi, Sim Cheng Kim, Nurul Najla, Nur Adillah, Nurul Syuhada, Ammar, Anwar and the rest for their support, advices, laughter and friendship throughout these years.

My acknowledgments are also extended to all technicians and officers of University of Malaya for their efforts in helping me to accomplish my research works. I am also thankful to IPPP program (grant no. FG034-17AFR, RP001B-13AFR and PG 010-2013A) for the financial support.

Lastly, my deepest gratitude goes towards my beloved family for their endless love, pray, support and motivation in numerous way.

TABLE OF CONTENTS

LIST OF FIGURES

LIST OF TABLES

LIST OF SYMBOLS AND ABBREVIATIONS

AC	:	Activated carbon
Al	:	Aluminium foil
EC	:	Electro-etched carbon fiber cloth
CDC	:	Charge and discharge
CE	:	Counter electrode
CFC	:	Carbon fiber cloth
CNT	:	Carbon nanotube
Co_3O_4	:	Cobalt oxide
CoO	:	Cobalt oxide
C_s	:	Specific capacitance
Cu	:	Copper
CV	:	Cyclic voltammetry
EC	:	Eletroetched carbon fiber cloth
EC-NiO	:	Nickel-cobalt oxide on EC
EDX	:	Energy dispersive X-ray spectroscopy
EIS	:	Electroimpedance spectroscopy
FESEM	:	Field-emission scanning electron microscopy
FTIR	:	Fourier transfer infrared spectroscopy
LIB	:	Lithium ion battery
LiC	:	Lithium ion capacitor
MnO	:	Manganese oxide
Ni	:	Nickel
NiCd	:	Nickel-cadmium battery
NiCoOH	:	Nickel-cobalt hydroxide

NiMH	:	Nickel-metal hybride
NiO	:	Nickel oxide
$Ni(OH)_2$	:	Nickel hydroxide
NiOOH	:	Nickel oxide hydroxide
Pac	:	Polyacetylene
PANI	:	Polyaniline
PAT	:	Poly(3-alkylthiophene)
PPy	:	Polypyrrole
PEDOT	:	Poly(3,4-ethylenedioxythiophene)
PEDOT-PSS	:	Polystyrene sulfonate
PPP	:	Poly(p-phenylene)
PPS	:	Poly-p-phenylyne-sulphide)
PPTA	:	Poly(p-phenylene-terephthalamide)
PPV	:	Poly(p-phenylenevinylene)
PTh	:	Polythiophene
PTh-V	:	Polythiophene-vinylene
PTV	:	Poly(2,5-thienylenevinylene)
RE	:	Reference electrode
RuO_2	:	Ruthenium oxide
SIB	:	Sulphur ion battery
SS	:	Stainless steel
TEM	:	Transmission electron microscopy
Ti	:	Titanium
WE	:	Working electrode
XRD	:	X-ray diffraction

CHAPTER 1: INTRODUCTION

1.1 Background

Over the past decades, energy demand has increased proportionally to development of technologies. This may lead to energy depletion due to unsubstantial supply of fossil fuels considering the expanding market for electric vehicle, portable electronic devices smart grid and off-grid energy storage. Due to this issue, renewable continuous energy are being actively researched and developed to cater to the requirement of having clean, portable and efficient energy storage devices (Simotwo & Kalra, 2016; Wang, et al., 2012).

Sources such as solar and wind power are highly needed in order to produce renewable energy that is required in progressive energy storage system with both high power and energy density. Due to the periodic behavior of the sun and the wind, electrochemical energy conversion and storage devices such as rechargeable batteries and supercapacitors are seen to be effective, practical and stable to ensure that energy can be easily stored and utilised (Xin, et al., 2017).

Battery is one of the most widely used electrochemical cell nowadays. It produces electrical energy from conversion of chemical energy. The expansion of research in batteries has led to the existence of various types of battery for specific purposes. For example, nickel-cadmium (NiCd) battery, nickel-metal-hybrid (NiMH) battery, sulfur ion battery (SIB), lithium ion battery (LIB) and lead acid battery. Rechargeable LIB are categorized as the most popular energy storage device since it can be easily found in laptop, mobile phone, portable medical equipment as well as electric vehicle because of the high energy density and viable power supply.

In comparison with supercapacitor, LIB has higher capacity value for energy storage. However, batteries have other constraints. Having high energy density comes with long

process taken for the energy conversion (Nie, et al., 2019; Qu, et al., 2019; Zhang, et al., 2019). Therefore, batteries are unsuitable for applications that require short-term power.

In recent years, much attention has been given to supercapacitor as it has the ability to operate in simple systems, long cycle life and progressively reproduce charge (Zhang & Zhao, 2009). In comparison with the conventional capacitor, supercapacitor has comparatively large energy density along with high power efficiency which provides the means of it being implemented in energy storage systems (Cheng, et al., 2011). The utilization of supercapacitor has been considered to be used in certain applications such as electric hybrid vehicles and digital communication devices (Capasso, et al., 2018; Xiong, et al., 2018).

One of the factors that play a big role in the electrochemical performance of supercapacitor is the choice of electrodes. Electrode materials have to be able to exhibit high capacitance, have great stability along with good mechanical properties as these properties are essential for a long cycle life. There are three major classes of electrode material which are (1) carbon (e.g. graphene, activated carbons (ACs) (Manoj, et al., 2019; Xu, et al., 2019b), carbon nanotubes (CNTs) (Jeong, et al., 2019; Ma & Kang, 2019), and carbon fibers (CFCs) (Mu, et al., 2019; Wang, et al., 2019b)); (2) metal oxide (e.g. manganese oxide (MnO) (Wei, et al., 2011), nickel oxide (NiO) (Sun, et al., 2019; Wang, et al., 2019a), cobalt oxide (CoO) (Duan, et al., 2019; Kannan, et al., 2018) and ruthenium oxide (RuO_2) (Kumar, et al., 2018; Prataap, et al., 2018; Yang, et al., 2018) and conducting polymer (e.g. polyaniline (PANI) (Moyseowicz & Gryglewicz, 2019; Mu, et al., 2013; Neelgund & Oki, 2011; Ryu, et al., 2002; Simotwo & Kalra, 2016; Zhang, et al., 2013a), polypyrrole (PPy) (Kai, et al., 2014; Ramya, et al., 2013; Xiao, et al., 2009), polythiophene (PTh) (Snook, et al., 2011; Wallace & Spinks, 2007), and polystyrene sulfonate (PEDOT-PSS)) (Du, et al., 2018; Jingbin, et al., 2013; Kim, et al., 2007).

Therefore, the main focal point of this thesis will be directed on the potential of the electrode material to be applied in energy storage devices.

1.2 Problem statement

The most crucial factor for fabricating flexible supercapacitors is the development of flexible electrodes with high capacitance and high electrical conductivity to ensure fast charge-discharge.

A common method to make flexible electrode is by depositing electroactive materials on soft and flexible substrates with porous structure. For example, carbon dispersions (carbon nanotubes, graphene oxide etc.) have been deposited as inks on cellulose papers (Islam, et al., 2018; Zhang, et al., 2018b), porous cotton (Hong, et al., 2019; Wang, et al., 2018) and synthetic polymer sponges (Dubal, et al., 2015; Wei, et al., 2017).

Conducting polymers, such as polypyrrole, polyaniline or poly(3,4-ethylenedioxythiophene)(PEDOT) have been directly deposited on soft and porous substrates via chemical or electrochemical polymerization. Despite their high flexibility and good ion accessibility, the electrical conductivity of these electrodes has been limited by insulating properties of substrates that affect the charge-discharge rate of supercapacitors. In addition, the total supercapacitors device weight increased due to the usage of insulating substrates, leading to a decrease of capacitance.

Another factor that has contributed in the performance of flexible supercapacitor is the structure and morphology of the electrode material. The effect of electrochemical properties of supercapacitor based on the size of the surface area of the material is widely studied (Alqahtani, et al., 2019). The effects of calcination temperature of metal oxide are one of the generally studied fields which are believed to be able to produce different

structures and morphologies of the material. This would eventually influence the electrochemical performance of the electrode (Xiao, et al., 2016).

1.3 Objectives of research

- To determine the characteristics and performance of binder-free polyaniline on etched carbon fiber cloth substrate.
- To evaluate the electrochemical performance of polyaniline based composite as active material in supercapacitor.

1.4 Organization of thesis

This thesis is divided into five chapters. Chapter 1 which consists of the overview of energy storage devices and supercapacitor is followed by the research objectives and thesis organization.

Chapter 2 plays the role in providing the background of supercapacitor, carbon fiber cloth (CFC) as the electrode substrate together with conducting polymer and metal oxides as the electrode material used in this work.

Chapter 3 consists of the elaboration on the experimental process of the sample preparation. Besides that, the characterization processes were also highlighted and discussed.

Chapter 4 discussed the results and discussion of the research. This includes the optimization of the PANI electrode where optimum potential applied in the electrodeposition process of PANI onto the electro-etched CFC (EC) was studied. The work in this section has been published in *Fabrication of Polyaniline Nanorods on Electro-Etched Carbon Cloth and its Electrochemical Activities as Electrode Materials*

(Razali, et al., 2018). Finally, the next section presents the characterization results of the composition of NiO and PANI electrode (NiO-PANI electrode). The calcination temperatures of the NiO was analyzed and optimized prior to the preparation of NiO-PANI electrode. The composition was optimized and elaborated in this chapter. The work in this section has been published in *Electrochemical Performance of Binder-Free NiO-PANI on Etched Carbon Cloth as Active Electrode Material For Supercapacitor* (Razali & Majid, 2018).

Chapter 5 summarizes and concludes the thesis with some comparison and suggestions for future work.

CHAPTER 2: LITERATURE REVIEW

2.1 Introduction

This chapter discusses the definition of supercapacitor and how the electrode material affects the performance of the energy storage device.

2.2 Supercapacitor

Supercapacitor is a charge-storage device similar to a rechargeable battery. It consists of three major components which are two highly conductive electrodes, electrolyte and separator.

Supercapacitors are capable in managing device with high power rates. It can go up to hundreds or thousands times higher in the same volume compared to batteries (Miller & Simon, 2008). However, supercapacitors are not able to store the same amount of charge as batteries do (Miller & Simon, 2008). Therefore, this makes supercapacitors more suitable for application with power bursts required and moderate energy storage capacity.

The power output of supercapacitors normally can reach up to 10 kW kg^{-1} (Chung, 2018). On the other hand, their specific energy is several orders of magnitude higher than the capacitors (Pandolfo & Hollenkamp, 2006). Supercapacitors could fill the gap between aluminum electrolytic capacitors and batteries, which are capable of storing large amounts of energy with average power densities (< 1 kW kg^{-1}) due to their storage mechanism (González, et al., 2016). This has been explained in graphical form of Ragone plot with different storage technologies in. The energy and power densities are represented in horizontal and vertical axes together with the discharge time of the devices in diagonal lines ($E = P \times t$).

Besides having high power rate, supercapacitors are also able to discharge in a short time period. This is important in energy recovery systems. For example, transport system's dynamic braking (González, et al., 2016). Table 2.1 compares the energy storage performance of supercapacitor, capacitor and battery.

Table 2.1: Comparison table among selected electrochemical energy storage technologies, taken from Pandolfo and Hollenkamp (2006).

Characteristics	Capacitor	Supercapacitor	Battery
Energy density (Wh kg^{-1})	< 0.1	1 - 10	10 - 100
Power density (W kg^{-1})	> 10 000	500 - 10 000	< 1000
Discharge time	10^{-6} to 10^{-3}	S to min	0.3 – 3 h
Charge time (s)	10^{-6} to 10^{-3}	S to min	1 – 5 h
Coulombic efficiency (%)	~100	85 - 98	70 - 85
Cycle life	Almost infinite	> 500 000	~ 1000

Supercapacitors are also able to withstand millions of cycle. This is due to its charge storage mechanism that works in irreversible chemical reactions and physically store charges at the surface of electrodes in an electric double layer. Table 2.2 shows the comparison of main differences in the properties of batteries and supercapacitors.

Table 2.2: Comparison between batteries and supercapacitors, taken from Miller and Simon (2008).

Comparison parameter	Battery	Supercapacitor
Storage mechanism	Chemical	Physical
Power limitation	Reaction kinetics, mass transport	Electrolyte conductivity
Energy storage	High (bulk)	Limited (surface area)
Charge rate	Kinetically limited	High, same as discharge
Cycle life limitation	Mechanical stability, chemical reversibility	Side reactions

Supercapacitor has its disadvantage related to the charge storage mechanism. In order to avoid the chemical decomposition of electrolytes, the operating voltage of a supercapacitor cell should be kept low (González, et al., 2016). Supercapacitor can be classified into two categories, a) electric double layer capacitors (EDLCs) and b) pseudocapacitors (Minakshi, et al., 2016; Naoi, et al., 2016; Salanne, et al., 2016).

2.2.1 Electric double layer capacitor

In the past few years, electric double layer capacitor (EDLC) has seen a significant increase in publication in various articles (Sharma & Bhatti, 2010). This is due to the demand the electrodes with high surface area as it can store more energy (Cheng, et al., 2017). The charge storage of EDLC is an electrostatic mechanism with no redox reaction involved. It stores charge through adsorption of electrolyte ions onto the surface of wired materials. Carbon was found to be the ideal material in EDLC electrode preparation as it has high conductivity, low density and also huge surface area.

2.2.2 Pseudocapacitor

Pseudocapacitance was discovered in 1971 where the term was chosen due to its reaction that involves faradaic charge-transfer. Several faradaic mechanisms which would result in capacitive electrochemical features are (1) underpotential deposition, (2) redox pseudocapacitance and (3) intercalation pseudocapacitance (Augustyn, et al., 2014).

The process of underpotential arises when an adsorbed monolayer was formed by metal ions at a different surface of metal above its redox potential, for example, lead on the surface of a gold electrode. Contrary to the underpotential, the redox pseudocapacitance occurs when ions are electrochemically adsorbed onto or close to the surface of the material associated with faradaic charge-transfer. Lastly, the intercalation pseudocapacitance takes place when ions intercalate into the tunnels or layers of a redox-active material accompanied by faradaic charge-transfer without any crystollagraphic change of phase. The mechanisms mentioned are due to the difference in physical process of different types of materials.

The pseudocapacitance is described to provide specific electrochemical features. The energy storage is represented based on its response to (1) voltage window; in cyclic voltammetry, (2) constant current; in charge and discharge and (3) alternating current; in impedance spectroscopy.

2.2.3 Hybrid supercapacitor

Hybrid capacitor is a combination of both EDLC electrode and pseudocapacitive or battery type electrode systems, leading to an intermediate performance in some cases. Generally, hybrid supercapacitor is able to improve overall cell potential, energy and power densities compared to EDLC. A good example of such a system is the lithium-ion capacitors (LiCs) (Pandolfo & Hollenkamp, 2006).

2.2.4 Parameters of supercapacitor

The total capacitance, C_T of a supercapacitor is a reflection of the electrical charge, ΔQ stored under a given voltage change, ΔV, as shown in Equation 2.1;

$$C_T = \frac{\Delta Q}{\Delta V} \tag{2.1}$$

A more essential specific capacitance (F g^{-1}) is defined to measure the charge storage ability of supercapacitor materials, shown in Equation 2.2;

$$C_T = \frac{\Delta Q}{\Delta V m} \tag{2.2}$$

where m is the mass of electroactive material.

Power density and energy density are the most often used parameters for evaluating the performance of supercapacitors. These parameters are normally evaluated gravimetrically or volumetrically in W kg^{-1} for power density and W h kg^{-1} for energy density. It is to describe the efficiency in energy uptake/delivery and to demonstrate the amount of electrical energy stored or deliverable (Sanliang & Ning, 2015).

The generally used calculation for maximum energy density (E) and power density (P) can be expressed in Equation 2.3 and Equation 2.4, respectively (Sanliang & Ning, 2015):

$$E = \frac{1}{2} C V^2 \tag{2.3}$$

$$P = \frac{V^2}{4 m R_s} \tag{2.4}$$

where C, V, m and R_s are specific capacitance, range of operating potential, mass of electroactive materials and the equivalent resistance of supercapacitor, respectively.

The operating potential (V) is determined by electrolyte window stability. The operating potential can be increased by implementing suitable electrolyte for the system. For example, organic electrolytes have cell potential in the range of 3.0 to 3.5 V (Huang, et al., 2018). On the other hand, aqueous electrolyte can normally operate at about 1 V. Besides electrolyte, suitable electrode material and optimized electrode structure can also offer high operating potential.

2.3 Electrode substrate

As previously mentioned, are supercapacitors composed of electrodes, separator and electrolyte, Figure 2.1. Among the three components, electrodes are generally considered to have a critical impact on the electrochemical performance of supercapacitors, and thus are extensively studied.

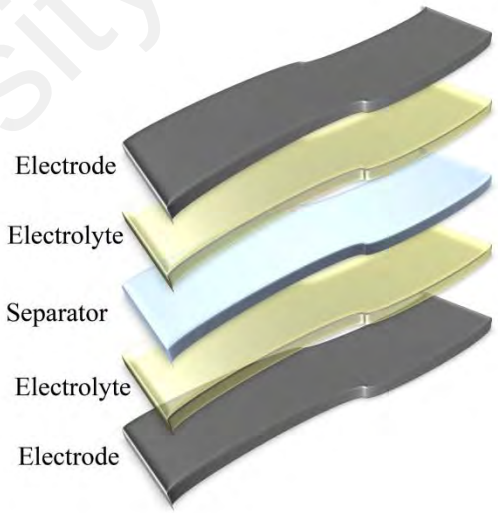

Figure 2.1: Supercapacitor's structure layers.

Typically, electrodes should have high surface area in addition to their requirement of being highly conductive. Currently, various strategies have been developed towards the flexible electrodes for supercapacitors, such as fabricating free-standing films of the active materials (Zheng, et al., 2009a). Therefore, novel support structures for the loading of pseudocapacitive materials are expected to produce high capacitance while being inexpensive and environmentally friendly (Zheng, et al., 2009a).

In recent times, porous materials such as conventional paper (Du, et al., 2018; Zhang, et al., 2018c), textiles (Xu, et al., 2019a), sponges (Liu, et al., 2017b) and cable type electrodes with thin conducting layers (Chen, et al., 2018; Vellacheri, et al., 2017) have been used as substrates to produce high performance supercapacitors. In addition, metal substrates are also common in the fabrication of electrodes for supercapacitors. Besides flexibility, various metal substrates such as stainless steel (SS), aluminum (Al), copper (Cu), nickel (Ni), and titanium (Ti) have many other advantages, such as high strength, high conductivity, and ease of preparation (Dong, et al., 2014; Dubal, et al., 2012; Dubal, et al., 2013; Jagadale, et al., 2012; Jingbin, et al., 2013).

One of the greatest electrode substrate is carbon fiber cloth (CFC). CFC consists of carbon microfibers manufactured into flat sheets. It is used as an electrode that facilitates the diffusion of reactants across the membrane electrode assembly (Afriyanti, et al., 2013; Park & Popov, 2011; Sawangphruk, et al., 2013). CFC has been widely used as electrode substrate for catalyst support, current collector, and gas transport layer. This is due to their porosity, mechanical integrity, large surface area, and good conductivity (Gongkai, et al., 2012; Meng, et al., 2010). Figure 2.2 shows the enlarged picture of the microfiber in CFC.

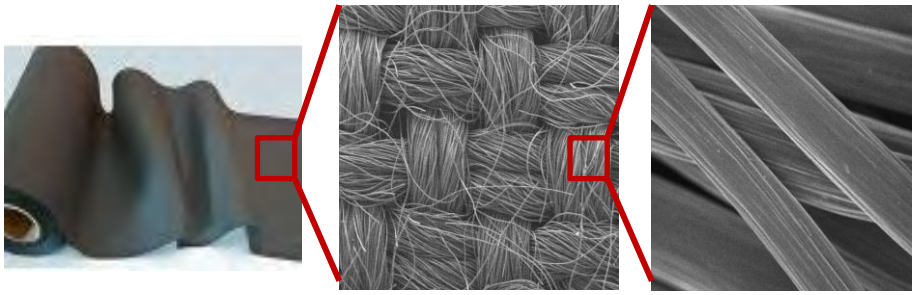

Figure 2.2: Structure of CFC in high magnification.

CFC can be a capable current collector and backbone for the coating of conducting polymers and transition metal oxides for supercapacitors. The single carbon fibers in CFC are well connected to form a conductive network with suitable pore channels. This is a huge advantage as it can offer efficient electron transportation path. Besides that, effective electrolyte access to the electrochemically active materials can be provided. Therefore, well-modified pore size distribution of CFC could enhance the specific capacitance of the electrode; hence generate a high power rate capability of the device (Dubal, et al., 2014).

2.4 Electrode material

The most important aspect in fabricating high power rate supercapacitor is the electrode material. There are three types of electrode materials that are widely used in producing supercapacitor; carbon, metal oxides and conducting polymer.

2.4.1 Carbon

Carbon based materials are broadly used in many applications and are employed for energy storage mostly in EDLC. They are relatively low in cost and high in availability. Examples of carbon materials are activated carbon (AC) (An, et al., 2018; Arnaiz, et al., 2018; Kiseleva, et al., 2018; Thaneswari, 2018; Yoo, et al., 2018; Zhang, et al., 2018b), carbon nanotubes (CNT) (Childress, et al., 2018; Kiseleva, et al., 2018; Thaneswari, 2018;

Yoo, et al., 2018; Zhang, et al., 2018a) and graphene (Moyseowicz & Gryglewicz, 2019; Ramesh & Jebasingh, 2019; Zou, et al., 2019). Although carbon-based electrode gives high cycle life, it possess at average a low specific capacitance value.

2.4.2 Metal oxide

Extensive research has been carried out on metal oxide based electrode material. Currently, energy storage device has been in a promising state due to the metal oxide electrode which has been a large part of the process. The ability of exhibiting reversible redox reaction enables the supercapacitor with metal oxide electrode to produce high capacitance value.

The earliest studied transition metal oxide for supercapacitor was RuO_2, and it is still recognized as one of the most promising electrode materials. RuO_2 has produced high theoretical specific capacitance (~2000 F g^{-1}) (Xu, et al., 2013), long cycle life, wide potential window, high electric conductivity, high rate capability and good electrochemical reversibility (Zhang, et al., 2011; Zhang, et al., 2009). The pseudocapacative behaviour of RuO_2 in an acidic electrolyte can be described as a fast and reversible faradaic reaction. In order to reduce the cost of supercapacitor electrode materials, a feasible scheme is developed to produce a cheap metal oxide/ hydroxide as an alternative candidate to replace RuO_2 (Kumar, et al., 2018; Li, et al., 2018; Prataap, et al., 2018).

NiO is another promising material for pseudocapacitor electrodes, due to its ultrahigh theoretical specific capacitance of 3750 F g^{-1}, low cost and environmental friendliness (Chang, et al., 2010; Wu, et al., 2008). The supercapacitive mechanism of NiO and the oxidation state changes in NiO occurs between NiO and nickel oxide hydroxide (NiOOH) (Equation 2.5);

$$NiO + OH^- \leftrightarrow NiOOH + e^- \quad (2.5)$$

Another theory indicates that at first NiO changes to nickel hydroxide ($Ni(OH)_2$) in alkaline electrolyte, then an electrochemical reaction occurs between $Ni(OH)_2$ and NiOOH, Equation 2.6 (Sahu, et al., 2017; Zhang, et al., 2012).

$$Ni(OH)_2 \leftrightarrow NiOOH + H^+ + e^- \quad (2.6)$$

The two theories reach an agreement that Ni^{2+} oxidizes to NiOOH through losing an electron, resulting in the supercapacitive reactions.

Nanostructured NiO materials can provide a large specific surface area, as well as short diffusion and transport pathways of ions and electrons, resulting in fast reaction kinetics (Ge, et al., 2013; Khairy & El-Safty, 2013; Xia, et al., 2011). Meanwhile, nanostructures can buffer the stress from swelling of the electrodes and inhibit pulverization, to enhance the cycling performance. Porous NiO with macropores have much larger specific capacitance.

In the work of Jahromi et al. (2015), nickel oxide nanoparticles with a uniform particle size were synthesized via a facile sol– gel method. Various crystal sizes of NiO nanoparticles (8, 12, and 22 nm) were achieved by calcination at various temperatures

Nanoflake structures of NiO were obtained by all samples. The highest specific capacitance achieved by sample calcined at 300 °C, was 379 F g^{-1} measured at 0.1 A g^{-1} in 1 M KOH electrolyte. This result is in agreement with the FESEM and HRTEM results, where the sample with the lowest crystal size exhibited highest specific capacitance due to its large surface area (Pilban Jahromi, et al., 2015).

Based on the literatures, calcination temperatures always play an important role in giving high specific capacitance in electrode materials. Therefore, it is important to obtain a small crystal size electrode material in order to achieve good electrochemical performance.

2.4.3 Conducting polymer

Other than carbon and transition metal oxide, conducting polymer is also labeled as promising electrode material for supercapacitor application. This is due to its unique properties such as flexibility, has good conductivity, ease of synthesis as well as high capacitance and rate capability which are strongly demanded in electrode fabrication.

There are several types of conducting polymer which are being widely used for electrode assembly such as stated in Table 2.3;

Table 2.3 Type of conducting polymers

Name	Abbreviation
Polypyrrole	PPy
Polyaniline	PANI
Poly(3,4-ethylenedioxythiophene)	PEDT, PEDOT
Polythiophene	PTh
Polythiophene-vinylene	PTh-V
Poly(2,5-thienylenevinylene)	PTV
Poly(3-alkylthiophene)	PAT
Poly(p-phenylene)	PPP
Poly-p-phenylyne-sulphide)	PPS
Poly(p-phenylenevinylene)	PPV
Poly(p-phenylene-terephthalamide)	PPTA
Polyacetylene	Pac

Conductive polymers can conduct charge thanks to the ease with which electrons jump within and between the chains of the polymer (Laleh, et al., 2011). The polymers possess a conjugated backbone (Balint, et al., 2014), meaning that it is formed by a series of alternating single and double bonds (Laleh, et al., 2011; Shirakawa, et al., 1977).

Single and double bonds both contain a chemically strong, localized r-bond, while double bonds also contain a less strongly localized p-bond (Ravichandran, et al., 2010). The p-orbitals in the series of p-bonds overlap each other, allowing the electrons to be more easily delocalized (i.e. they do not belong to a single atom, but to a group of atoms) and move freely between the atoms (Laleh, et al., 2011; Shirakawa, et al., 1977; Wong, et al., 1994). The final key to the conductivity of these polymers is the dopant (Kim, et al., 2007; Laleh, et al., 2011; Ravichandran, et al., 2010; Xiao, et al., 2009). The polymer is synthesized in its oxidized, conducting form, and only in the presence of the dopant molecule (a negative charge/anion in most cases) is the backbone stabilized and the charge neutralized (Wallace & Spinks, 2007). Parallel to this, the dopant introduces a charge carrier into this system by removing or adding electrons from/to the polymer chain and relocalizing them as polarons or bipolarons (a loosely held, but localized, electron surrounded by a crystal lattice distortion (Laleh, et al., 2011; Ravichandran, et al., 2010; Xiao, et al., 2009).

As an electrical potential is applied, the dopants start to move in or out of the polymer (depending on the polarity), disrupting the stable backbone and allowing charge to be passed through a polymer in the form of the above-mentioned polarons and bipolarons (Laleh, et al., 2011; Ravichandran, et al., 2010; Xiao, et al., 2009).

2.4.3.1 Polyaniline

Polyaniline (PANI), which is also known as aniline black, is one of the groundbreaking conducting polymers, which can be synthesized both chemically and electrochemically. In the early works followed by the first report in 1886, PANI were synthesised based on electropolymerization. In 1968, the high electrical conductivity of PANI and its potential electrochemical applications were discovered (De Surville, et al., 1968). The early works on electropolymerization of aniline during mid-20th century were carried out by standard sweep voltammetry (Gilchrist, 1903; Green & Woodhead, 1910), without observe the electrochemical reversibility behaviors due to the absence of modern cyclic voltammetry (CV).

An appropriate report on the electrochemical property of PANI was done by Diaz and his coworker (Diaz & Logan, 1980). PANI has then become one of the most famous conducting polymers in the dominion of electrochemistry (Ćirić-Marjanović, 2010), due to its facile electropolymerization and promising electrochemical properties.

PANI is a readily available p-type conducting polymer. It has gained considerable attention for application in electrodes of most energy storage devices, either as a sole electrode active material or supplement material acting as a performance enhancer. PANI can exist in three different oxidation states: (1) leucoemaraldine, (2) emaraldine and (3) pernigraniline which are the fully reduced, partially oxidized and fully oxidized states, respectively (MacDiarmid & Epstein, 1989).

PANI is commonly synthesized through chemical oxidative polymerization of aniline using a strong oxidant (García-Gallegos, et al., 2018; Song, et al., 2017). Electrochemical synthesis of polyaniline has also been widely studied (Jafari, et al., 2018; Li, et al., 2019; Shen & Huang, 2018; Shklovsky, et al., 2018).

PANI nanostructures are prepared either via a template-assisted method where an external soluble or insoluble substrate with pre-formed nanoscale features is employed such as a metal oxide (Su, et al., 2017). The synthesis can also be a template-free technique. It considers the material's ability to self-assemble into various morphologies depending on the synthesis conditions. For example, pH value, temperature and nature of dopants (Agilan & Rajendran, 2018; Mello & Mulato, 2018).

Synthesis of PANI is largely carried out in acidic conditions, which result in a protonated/doped emeraldine salt. External doping or de-doping of the emeraldine salt has also been achieved using an acid or base, respectively (Chiang & MacDiarmid, 1986). PANI has been extensively studied as a supercapacitor electrode due to its high capacitive characteristics and low cost (Kandasamy & Kandasamy, 2018; Miller, et al., 2018; Ouyang, 2018; Sayah, et al., 2018).

Conductivity of PANI is strongly dependent on the degree of oxidation and the doping. Doped emeraldine base is the most conducting one, with conductivity value ranging from 0.1 to 100 S cm^{-1} (Xia, et al., 1994). Un-doped emaraldine and the fully reduced/oxidized states show conductivity in the order of 10^{-10} S cm^{-1}.

In employing PANI in a supercapacitor as the electrode material, extensive research has been conducted. Classic supercapacitors feature the charge to be delivered in monotonic way over the discharging potential window. This is represented by the diagonal line in the charge/discharge profiles. Arbizzani et al. (1996) the initiators who unambiguously attributed the supercapacitor performance of conducting polymers to redox reactions by differentiating it from charge separation at double layer (Arbizzani, et al., 1996). In a comparative study of various conducting polymers, they showed that the charge/discharge profiles could be a line rather than flat plateau of battery-like performance (Arbizzani, et al., 1996).

One of the key factors controlling the electrochemical behavior of conducting polymer in general is morphology. Excellent supercapacitor performance can be achieved by altering the polymer morphology during the synthesis (Chellachamy Anbalagan & Sawant, 2016). It has been reported that by adding a small amount of additives such as para-phenylenediamine during the polymerization process can result in the formation of longer polymer chains which are less entangled. This significantly improves the specific capacitance and energy of the PANI supercapacitor (Desilvestro & Scheifele, 1993).

The role of PANI morphology is critically important even in all-solid-state cells in which the electroactive material is not soaked in the electrolyte to increase the electrode/electrolyte interface (Roy, et al., 2018). In the chemical polymerization of aniline, various controllable parameters can change the morphology of the resulting PANI. For example, it has been reported that by changing the polymerization temperature, a noticeable effect on the specific capacitance and cyclability of the supercapitors (Li, et al., 2019) was observed. Increasing the electrochemically accessible surface area by forming porous PANI can also significantly improve the supercapacitor performance (Liu, et al., 2018; Moyseowicz & Gryglewicz, 2019; Tabrizi, et al., 2018).

From the studies of Wang *et al*. (2014), PANI was self-assembled by chemical oxidative copolymerization of aniline. The electrode was able to reach 119 F g^{-1} specific capacitance measured at 1 A g^{-1} in 1 M H_2SO_4 electrolyte. This proved that a significant electrical double-layer capacitance and Faradic pseudocapacitance were achieved due to its regular nanorod morphology with large surface area and high electrical conductivity (Wang, et al., 2014).

Mu et al. (2013) reported another simple chemical template-free polymerization method in the presence of D-tartaric acid (D-TA) as the dopant. The PANI nanotube was obtained with specific capacitance of 625 F g^{-1} at current density of 1 A g^{-1} in 1 M H_2SO_4 electrolyte.

In this work, binder free PANI has been directly deposited onto EC to improve the electrical conductivity. In the following section, the literature of PANI composite with metal oxide or carbon electrodes which are related to this thesis is compared and studied.

2.4.3.2 PANI-based composite electrode

Damage to the morphology caused by swelling and shrinkage of electrode materials during charging and discharging processes leads to poor cycling stability (Shi, et al., 2014). As a potential pseudocapacitive material, PANI still suffer from limited cycling stability, high self-discharge rate and low attainable doping degree as well as mass transport limitation within thick polymer layers (Leif, et al., 2011). To resolve these issues, PANI has been crosslinked (Wang, et al., 2014), nano-structured (Li, et al., 2014) or supported on various inorganic nanomaterials as composites (He, et al., 2012). Table 2.4 shows the electroactivity of polyaniline-based supercapacitors from previous works with the cycle life.

Table 2.4: Polyaniline-based supercapacitors, electroactivity (per gram of total electrode mass) at different current densities, and cycle life.

PANI composite	PANI wt.%	Specific capacitance (Fg^{-1}), current density	% retention (cycles)
Graphene (Simotwo, et al., 2016)	40	448, 1.0 Ag^{-1}	81 (5000)
CNF (Tran, et al., 2015)	48	409, 0.1 Ag^{-1}	80 (1000)
MWCNT (Ansari, et al., 2016)	95	530, 1.0 Ag^{-1}	90 (1000)
MnO_2 (Ansari, et al., 2016)	90	525, 2.0 Ag^{-1}	77 (1000)

Ansari et al. (2016) reported a simple one-step and scalable in situ chemical oxidative polymerization process of PANI-MnO_2 nanocomposite. Fibrous Pani-MnO_2 nanocomposite achieved high capacitance (525 F g^{-1} at a current density of 2 A g^{-1}) and good cycling stability of 76.9% after 1000 cycles at 10 A g^{-1} which is more stable compared to PANI electrode (Ansari, et al., 2016).

2.5 Summary

In summary, supercapacitor is believed to be one of the best alternatives to overcome the energy demands issue due to their higher power density and longer cycle life compared to battery. Electrode of a supercapacitor plays an important role to achieve high energy and power density with a variety of electrode materials. One of the examples is PANI. However, PANI exhibited poor cycling stability. This problem can be overcomed by compositing PANI with transition metal oxide materials. Different composite materials would yield different electrochemical performance and morphology.

In this work, the electropolymerization parameter of PANI has been optimized in order to obtain a uniform coat of PANI on electro-etched carbon fiber cloth. To overcome the poor cycling stability issue, NiO has been introduced to PANI in order to form NiO-PANI composite.

CHAPTER 3: EXPERIMENTAL METHODS

3.1 Introduction

This chapter will elaborate the preparation and characterization process of the samples which involves several methods.

3.2 Electrode preparation

The electrode preparation process consists of a few different steps for each system. This covers the electro-etching process of carbon fiber cloth (CFC), NiO and Ni-Co growing process and lastly, PANI electrodeposition. The list of material used in this are as listed in Table 3.1.

Table 3.1: List of chemicals.

Chemical / material	Manufacturer	Details
Carbon cloth	ELAT	99.5% carbon
Aniline	Sigma Aldrich	≥ 99.5% 93.13 g mol^{-1}
Sulphuric acid	Sigma Aldrich	95.0%
Nickel nitrate hydroxide	Unilab	290.81 g mol^{-1}

3.2.1 Electro-etching process

The electro-etching process was conducted in three electrodes system electrolysis consisting of working electrode (WE), counter electrode (CE) and reference electrode (RE). The working electrode is stable where it does not support the completing reaction of hydrogen (H_2) evolution and oxygen (O_2) evolution/reduction during the electrolysis

process besides being durable against corrosion. The current is controlled by the working electrode as it provides current in opposite sign with equal magnitude to the working electrode while the reference electrode acts as the medium to maintain constant potential throughout the experimental process (Li, et al., 2009).

The working electrode used in this work was 2 cm^2 of CFC substrate with general specifications of 454 µm thickness, 170 g m^{-2} basic weight and 0.377 g cm^{-3} density. The binder was PTFE treated woven fiber with 99.5% carbon. The CFC was etched electrochemically by using potentiostat (Autolab, PGSTAT30) on chronoamperometry method fixed at 2 V potential for 10 minutes with the CFC act in as the working electrode (WE) in 0.5 M H_2SO_4 electrolyte. The substrate was later washed with distilled water and dried at 300 °C for 3 hours. The counter (CE) and reference electrode (RE) used is platinum wire and silver/silver chloride (Ag/AgCl) respectively, Figure 3.1.

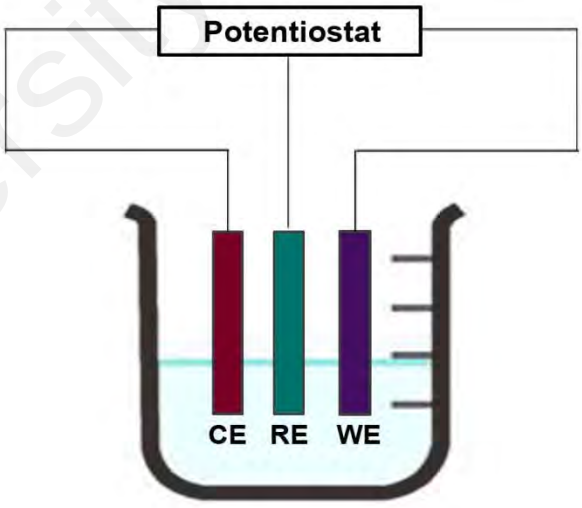

Figure 3.1: Electro-etching set up.

3.2.2 Polyaniline Embedded On Electro-Etched Carbon Fiber Cloth Electrode

The electrodeposition process was setup identically as the electro-etching process where three electrodes system was employed and electro-etched CFC (EC) acts as the working electrode in 0.5 M PANI in H_2SO_4 electrolyte. The time taken took place for the electrodeposition process was fixed at 60 seconds while the applied potential was varied for each sample as shown in Table 3.2.

Table 3.2: Sample designation for PANI on EC electrode.

Potential applied (V)	Sample designation
1.2	P1.2
1.4	P1.4
1.6	P1.6
1.8	P1.8

The samples were washed and dried at 60 °C for 10 hours prior to being used for characterization. Figure 3.2 shows the difference in physical observation of the electrodes before the electro-etching process (pristine CFC), EC and deposited samples.

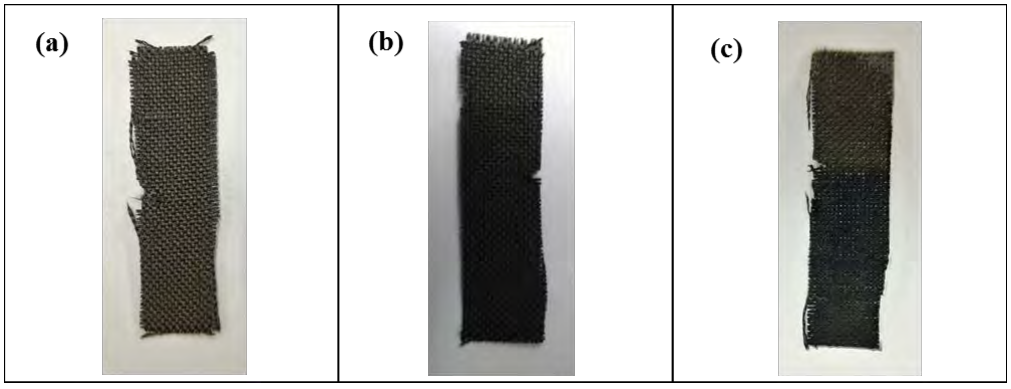

Figure 3.2: (a) pure CFC, (b) EC and (c) deposited electrode.

3.2.3 Nickel oxide-polyaniline composite embedded on carbon fiber cloth electrode

The nickel hydroxide ($Ni(OH)_2$) was prepared by using hydrothermal method. 4 mmol of nickel nitrate hydroxide ($Ni(NO_3)_2.6H_2O$) was dissolved together with 2 mmol of urea in 40 mL of distilled water for 10 minutes. The resultant mixture was transferred into a Teflon-lined autoclave with stainless-steel shell together with EC, and was maintained at 120 °C for 6 hours. The product grown on EC was washed with distilled water and heated at different temperatures i.e. 200, 300, 400 and 500 °C for 3 hours to grow NiO on EC (EC-NiO).

PANI nanowires were electrodeposited using the chronoamperometry method on the EC-NiO. The deposition electrolyte consists of 0.5 M purified aniline monomer in 0.5 M H_2SO_4 solution. The applied potential was fixed at 1.4 V for 60 seconds deposition time. The electrochemical cell consists of EC-NiO substrate as the WE, platinum wire as the CE, and Ag/AgCl as the RE. Prepared electrodes were heated in a furnace at 60 °C for 10 hours before being characterized. The samples' designated names are as stated in Table 3.3.

Table 3.3: Sample designation for EC-NiO electrode, with and without PANI.

Heating temperature	Designation	
	Without PANI	With PANI
200	Ni200	NiP200
300	Ni300	NiP300
400	Ni400	NiP400
500	Ni500	NiP500

3.3 Characterizations

This section elaborates on the characterization process involved in the research. The composition and morphology of the samples as well as their electrochemical properties were examined by using the following characterization techniques, as explained in the next subsections.

3.3.1 X-ray diffraction (XRD)

XRD is a non-destructive analytical method to observe material properties such as structure, phase composition, and texture. The XRD instrument used in this work was D8-advance X-ray diffraction XRD Bruker AXS with monochromatised radiation of CuKα. The operating voltage and current were 40 kV and 40 mA respectively. In this work, XRD is used to detect changes in properties of the composite electrode with various potential applied during electrodeposition process and different post heating temperature. Since different temperature is applied for each composite electrode, the impact of post–heating temperature on the structure of material can be identified. The XRD result was displayed in the plot of scattered intensity versus Bragg angle 2θ.

3.3.2 Fourier transform infrared spectroscopy (FTIR)

The fundamental vibration of the polymer electrolytes were studied using FTIR spectroscopy in the wavenumbers region between 4000 and 650 cm^{-1} at a resolution of 1 cm^{-1}. The basic principle behind the molecular spectroscopy is that specific molecules absorb light energy at specific wavenumber, known as their resonance frequencies.

In this work, the spectra was obtained using Thermo Scientific Nicolet iSIO Smart ITR machine. The deconvolution of FTIR spectra band was done by using Origin 8.5 software.

3.3.3 Raman spectroscopy

Raman spectroscopy is a spectroscopic technique used to examine molecular vibrational, rotational, and other low-frequency modes of the sample. When a monochromatic light source (i.e laser) illuminates the sample, the laser light interacts with molecular vibrations, phonons or other excitations in the system. Energy of laser photons will be shifted up or down. This shifted energy gives information on molecular vibration of the system. In this work, the Raman spectra were obtained using Renishaw in Via Raman microscope with a green laser beam. The deconvolution of Raman spectra band was done by using Origin 8.5 software.

3.3.4 Field-emission scanning electron microscopy (FESEM) and

Field-emission scanning electron microscopy (FESEM) is used to envisage the topography of a sample. This enables us to get a better view of the structure of the material up to nano-scale resolution. In this thesis, FESEM was employed to examine the morphology of the electrode prepared.

The FESEM instrument used was Jeol JSM-7600F field scanning electron microscopy. The electrode was cut into an appropriate size to fit in the specimen stub. FESEM consists of a field emission gun and a series of electromagnetic lenses and apertures. FESEM works by striking a specimen with high energy electrons which will produce elastic and inelastic scattering. Elastic scattering takes place when the incident electrons is ejected from the atoms in the specimen. During inelastic scattering process, kinetic energy is transferred by the incident electrons to the atoms of the specimen. The detected signal electrons from the specimen are collected by a detector and used for image reconstruction (Leng, 2008). Different magnifications were used in the observation such as 30 K, 100 K and 200 K to get better information of the sample morphology.

3.3.5 Energy dispersive X-ray spectroscopy (EDX)

EDX is used to investigate the elemental compositions of the specimen. A high energy electrons beam is focused into the interested sample. The incident beam may excite an electron in an inner shell of sample and ejecting it from the shell while creating an electron-hole. An electron from its outer shells fills the hole and results in the difference in energy between higher energy shell and lower energy shell which may be released in the form of X-rays. The energy of X-rays emitted from the specimen is then measured by energy dispersive spectrometer. In this thesis, the FESEM equipped with EDX was used to examine our sample morphologies and elemental compositions.

3.3.6 Transmission electron microscopy (TEM)

Transmission electron microscopy (TEM) is a microscopic technique which enables the display of fine detailed microstructure due to having smaller wavelength of electron in comparison with light in high resolution. TEM has a similar working principal as microscope, but instead of light, it employs electron during the analysis of a material's microstructure. The basic working principle of TEM is a beam of electrons is transmitted through an ultra-thin specimen. The image resulted from the electrons' interaction transmitted through the specimen (Leng, 2008).

The TEM instrument used was Jeol-2100F transmission electron microscopy to investigate the electrode's composite structure. Prior to the TEM characterization, the scrapped off electrode material embedded on EC was dispersed in and sonicated in ethanol for 5 minutes. The solution then was dropped on copper grid and dried at room temperature for 72 hours.

3.3.7 Thermogravimetric analysis (TGA)

Thermogravimetric analysis (TGA) is a technique for measuring mass change of a sample with temperature. A sample to be measured is placed in a furnace and its mass change is monitored by a thermobalance. The main application of TGA is to analyze material decomposition and thermal stability through mass change as a function of temperature. The measurement is done in scanning mode or as a function of time in the isothermal mode. TGA curves are plotted as mass change expressed in percent versus temperature or time.

Decomposition of a sample is represented by two characteristic temperatures: T_i and T_f. T_i is the lowest temperature when the onset of mass change is detected and T_f is the lowest temperature when the mass change is completed. In Chapter 4, the TGA curve was obtained by using Mettler Toledo analyzer, which consists of a TGA/SDTA851e main unit. The temperature range used is from 30 to 900 °C with heating rate of 10 °C min^{-1} in nitrogen atmosphere.

3.3.8 Cyclic voltammetry (CV)

CV is a potential sweep technique to study the reaction of working electrode and determine the energy storage capacitance of supercapacitor. The working electrode is swept between two selected potential limits (E_i and E_f) at a particular rate in which current is monitored. The potential will be scanned initially in a positive direction to study the oxidation and negative direction to investigate the reductions. The presence of oxidation and reduction peaks indicate a redox reaction has occurred in the cell. The peak weight and height of the CV profile may depend on the applied sweep rate. The specific capacitance can be calculated using CV curve by Equation 3.1 (Zhang & Zhao, 2009)

$$C = \frac{\int I\, dt}{\Delta V \times m} \tag{3.1}$$

Where I is the oxidation/reduction current, dt is time differential, m is the mass of active material and ΔV is the operating potential.

In this thesis, most of the CV studies were conducted in three electrode system. The prepared electrode was used as working electrode. Ag/AgCl and platinum wire were used as reference and counter electrode respectively. The CV profile was examined in 0.5 M H_2SO_4 electrolyte.

3.3.9 Charge and discharge (CDC)

CDC characterization is based on the voltage-composition relationship of an electrochemical cell. In CDC study, the cell is charged-discharged at a constant current between maximum potential until cut-off discharge potential is applied. The CDC measurement of potential against time is obtained and the specific capacitance can be calculated from CDC discharge curve by using the following Equation 3.3 (Li, et al., 2009).

$$C = \frac{I}{\frac{dV}{dt} \times m} \tag{3.3}$$

Where I is the discharge current, dV/dt is the change of discharge potential with respect to discharge time and m is mass of the active materials.

The CDC studies were conducted in three electrodes system and symmetrical two electrodes system. In three electrodes system, the prepared electrode was used as working electrode. Ag/AgCl and platinum wire were used as reference and counter electrode respectively and was measured in 0.5 M H_2SO_4 electrolyte. In symmetrical two electrodes system assembly, The CDC profile was studied in 0.5 M H_2SO_4 + PVA electrolyte.

3.3.10 Electrochemical impedance spectroscopy (EIS)

EIS is used to study the impedance resistance or conductivity of the electrode materials. The analysis of impedance study for various electrode structure and electrolyte are very important to design and optimize the device performance. In this work, all of the EIS tests were performed within the frequency from 0.01 Hz to 100 KHz in 0.5 M H_2SO_4 electrolyte.

3.4 Summary

In summary, two different methods of electrode preparation have been applied to the electro-etched carbon fiber cloth, i.e. electrodeposition and hydrothermal method. Besides that, sample characterizations were carried out by referring to the structure, morphology and electrochemical properties.

CHAPTER 4: RESULTS AND DISCUSSION

4.1 Introduction

This chapter includes the findings obtained from every system studied in the research. The results are tabulated and discussed in the following sections.

4.2 Polyaniline Embedded on Electro-Etched Carbon Fiber Cloth Electrode

This section discusses the structure and morphology of PANI-based electrode embedded on etched carbon cloth, EC followed by the electrochemical analysis.

4.2.1 Introduction

Over the past decade, conductive polymer has been widely used in various applications such as transistor (Aleshin, 2006), electromagnetic shielding (Kamchi, et al., 2013), batteries (Dziewoński & Grzeszczuk, 2010), sensors (Peng, et al., 2009) and supercapacitors (Indrajit, et al., 2015). For supercapacitor application, conductive polymer is a very good choice to be used as the electrode material. This is due to its ability to improve the charge storage by having high doping/de-doping rates during the charge-discharge process (Indrajit, et al., 2015).

In this work, simple direct potentiostatic electrodeposition method is applied for the electro-polymerization of PANI onto EC. The process took place without having any surfactant or plasticizer addition. Electrodeposition is a simple method and easy to use with accurate control of deposited material by having the deposition parameter monitored and adjusted according to the requirement needed.

4.2.2 Electrodeposition mechanism

The electrodeposition process involves potential that is applied which comprised of a redox transition of leucomeraldine and polaronic emeraldine of PANI (Ebrahim, et al., 2016; Zhang, et al., 2013b). Figure 4.1 displays the schematic diagram of electrodeposition process, and the chronoamperometry (CA) curve obtained from the electrodeposition process. Symbol '¤' represents the change of phase from leucomeraldine to polaronic emaraldine (Zhang, et al., 2013b).

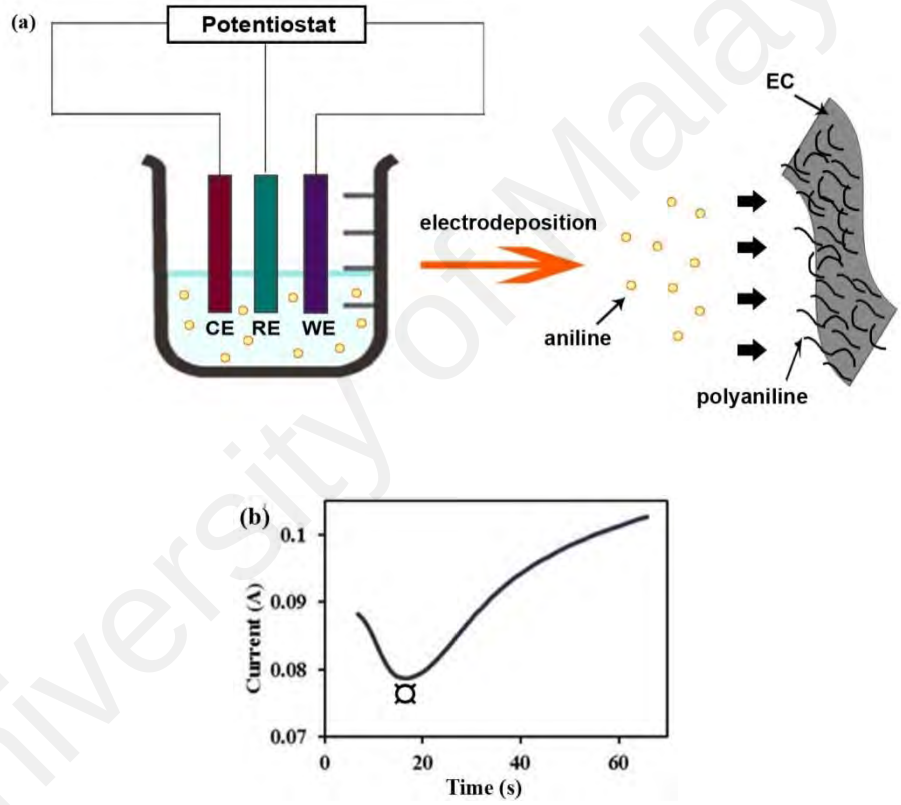

Figure 4.1: (a) Schematic diagram of electrodeposition process of PANI and (b) the CA curve of the process.

In this work, PANI was electrodeposited onto EC instead of CFC substrate in order to achieve better access for the electrolyte cation (Cheng, et al., 2011). EC is able to provide more channels for ion movement due to the enhanced porosity compared to CFC as

reported by Cheng and coworkers. This advantage is necessary for supercapacitor applications as it can prevent agglomeration of electrode material (Cheng, et al., 2011; Horng, et al., 2010).

4.2.3 X-ray diffraction

In order to confirm the formation of PANI on EC, composition and elemental studies of the electrodes were performed. The XRD patterns of all electrodes are displayed in Figure 4.2. The XRD spectra of all deposited PANI samples has similar pattern with the EC substrate. This indicates that the deposited films were too thin or amorphous in nature (Rusi & Majid, 2013).

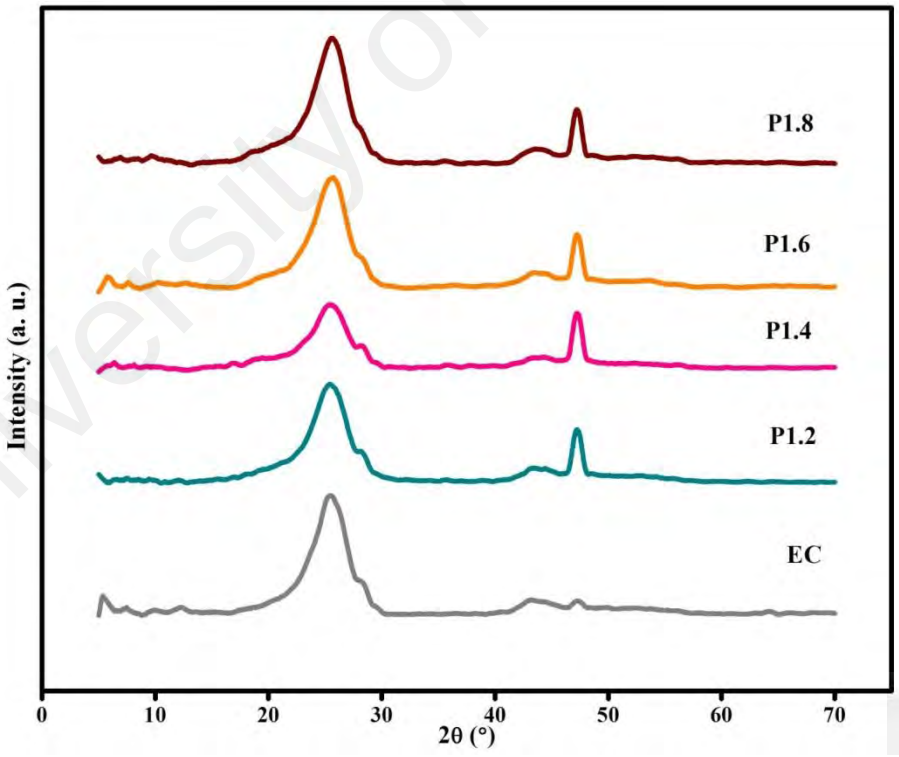

Figure 4.2: XRD diffractogram of all electrodes.

The XRD patterns were deconvoluted at the range of 2θ = 10° to 30° to confirm the obscured PANI peak. Figure 4.3 reveals the two prominent peaks resolved from this region for all deposited samples. One peak appeared approximately at 2θ = 23.7°, 22.5°, 21.7° and 22.1° for sample P1.2, P1.4, P1.6 and P1.8, respectively, which represents the carbon from EC with a corresponding plane of (200). The other peak centred at 2ϑ = ~25.5° which appeared in all samples is contributed by PANI (Guo, et al., 2015; Xu, et al., 2014; Zhou, et al., 2014b).

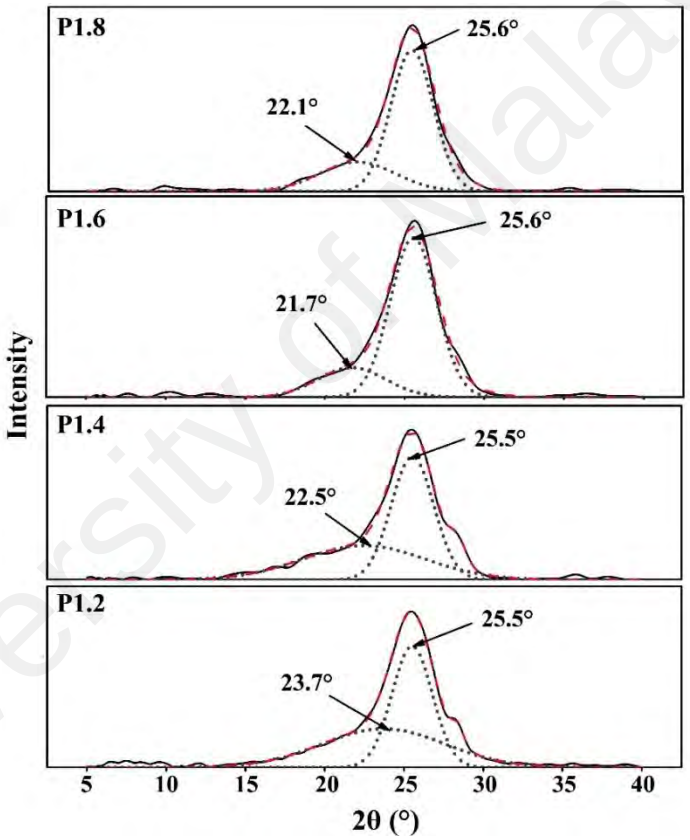

Figure 4.3: Deconvoluted XRD diffractogram of all deposited PANI electrodes.

4.2.4 Energy dispersive X-ray spectroscopy (EDX)

The elemental composition of the deposited layer obtained from EDX is shown in Figure 4.4. The element of carbon and nitrogen are found which belong to EC-PANI. The presence of sulphur element can be due to H_2SO_4 used during the electrodeposition

(Bláha, et al., 2017). Oxygen which is also found in the spectra is probably from the H_2SO_4. FTIR has been investigated in order to see clearly the evidence of deposited PANI.

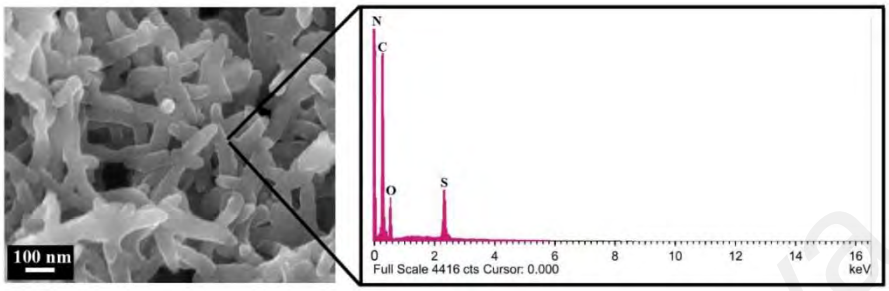

Figure 4.4: EDX spectrum of P1.4 obtained from selected region.

4.2.5 Fourier transform infrared spectroscopy

FTIR study was conducted for all electrodes in order to further confirm the PANI formation on EC. Figure 4.5 displays the FTIR spectra of PANI vibrations on EC.

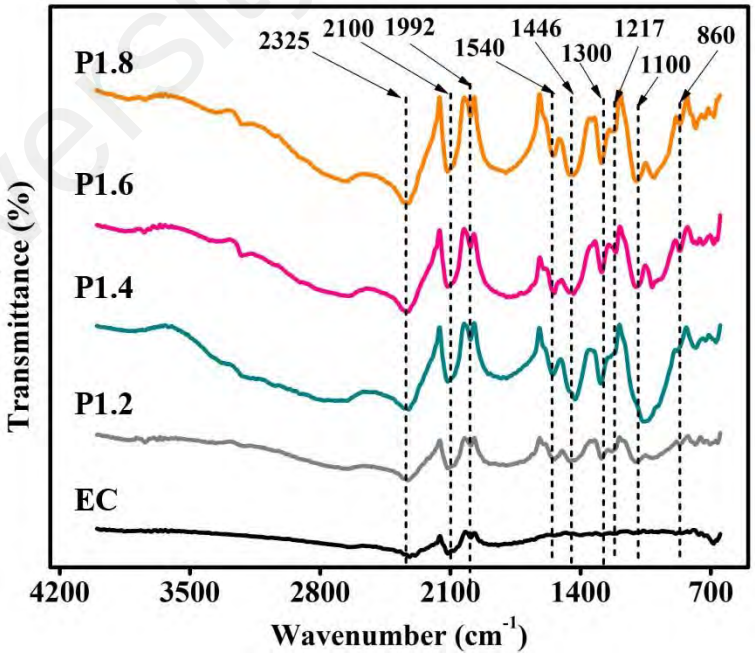

Figure 4.5: FTIR spectra of EC and all deposited PANI electrodes.

The peaks at ~2100 cm^{-1} and ~1992 cm^{-1} correspond to the EC. These two peaks verified that PANI has been successfully deposited on the EC substrate. Peaks at ~1540 and ~1446 cm^{-1} are assigned to the C=C stretching vibrations of the quinoid (N=Q=N) and benzenoid (N-B-N) rings, respectively. Peaks representing aromatic C−N stretching vibrations of the quinoid rings and the C–N stretching vibration of the benzenoid rings can be observed at ~1300 and ~1217 cm^{-1}, respectively (Tao, et al., 2007). The presence of peaks at ~1100 cm^{-1} and ~860 cm^{-1} are related to the symmetric O=S=O stretching vibrations and the 1,4-substituted phenyl ring stretching of the emeraldine salt form of PANI (Trchová, et al., 2006; Venancio, et al., 2006).

4.2.6 Field-emission scanning electron microscopy

The morphology of prepared electrodes was investigated through FESEM characterization (Figure 4.6).

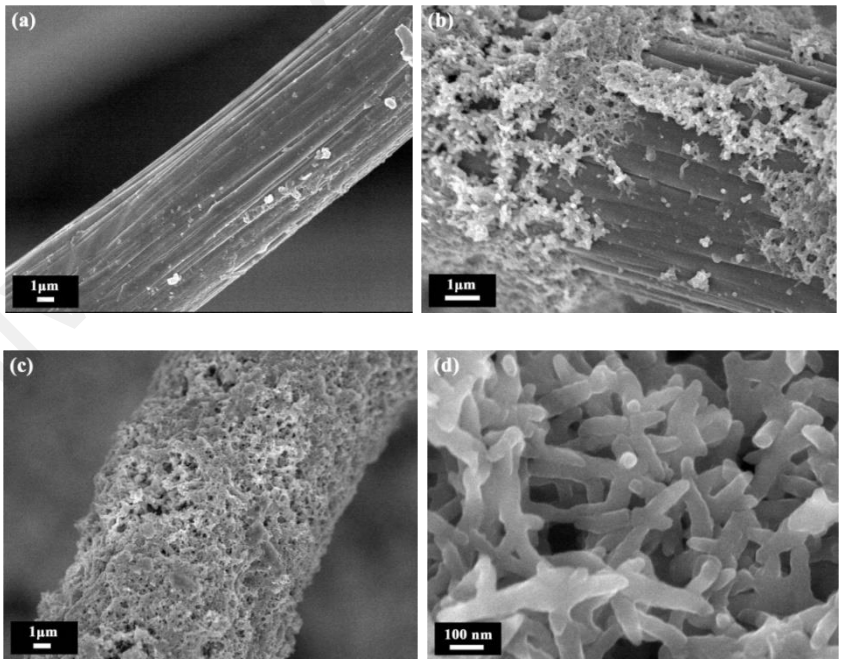

Figure 4.6: FESEM images (a) EC, (b) P1.2, (c) P1.4 at X 5000 magnification and (d) P1.4, (e) P1.6 and (f) P1.8 at X 100 000 magnification.

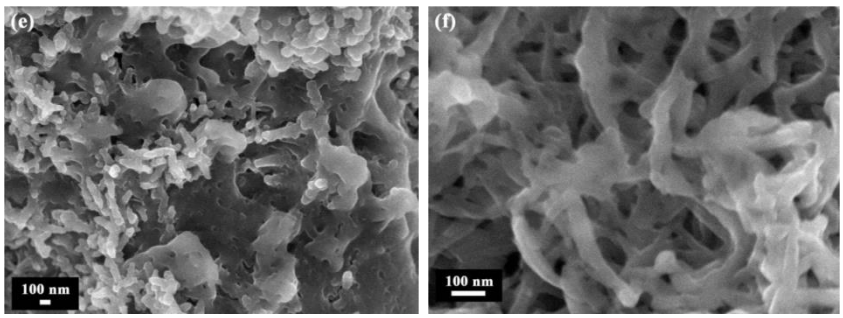

Figure 4.6, continueued

Figure 4.6 (a) shows a bare fibre of EC that act as the base for growing PANI. In Figure 4.6 (b), it can be clearly seen that PANI nuclei grown unevenly on EC. This is probably due to the slow deposition rate of monomers when the potential was applied at 1.2 V. This situation eventually resulted in insufficient time for PANI nucleation to cover the entire substrate within the 60 seconds of the deposition time.

On the other hand, PANI nuclei grew uniformly when the applied potential was increased to 1.4 V, Figure 4.6 (c). In a high FESEM magnification of P1.4 (Figure 4.6 (d)), a clear nanorods with an average diameter of 57.7 nm was observed. This structure is conceivably an ideal structure for ion absorptions (Saranya, et al., 2015). Further increase in applied potential value to 1.6 V and 1.8 V, led to thick deposition with agglomerated nanorods (Figure 4.6 (e, f)), as well as increment in the mass of electrode material (from ~0.045 g to ~0.086 g).

4.2.7 Transmission electron microscopy

A representative TEM image of the selected electrode is shown in Figure 4.7. This figure reconfirmed that deposited PANI had built up from small PANI nanorods, which is in agreement with FESEM results. From these structural studies, applied potential was shown to strongly influence the morphology and thickness of the deposits. It is believed that the morphology and thickness will affect the electrochemical performance.

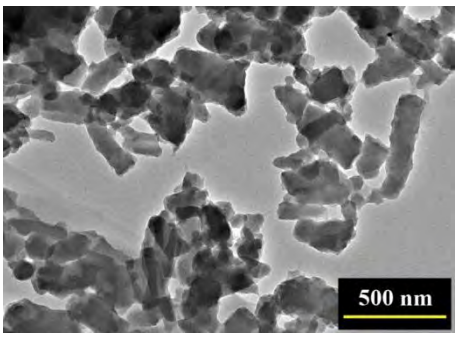

Figure 4.7: TEM image of sample P1.4.

4.2.8 Cyclic voltammetry

In order to evaluate the electrochemical behavior of EC-PANI electrode, CV, GCD, EIS, and cycle stability test were conducted.

CV of PANI is generally composed of three redox couples reactions over a wide range of potential (Eftekhari, et al., 2017). In this work, two sets of redox reactions can be clearly seen, Figure 4.8. The redox transition occurred between the insulating phase of PANI, leucoemeraldine and protonated emeraldine which is the conducting phase of PANI. The reaction is shown at peak A/A' pair. Another set involves the phase transition between the emeraldine and the pernigraniline, peak B/B' (Eftekhari, et al., 2017), Figure 4.8.

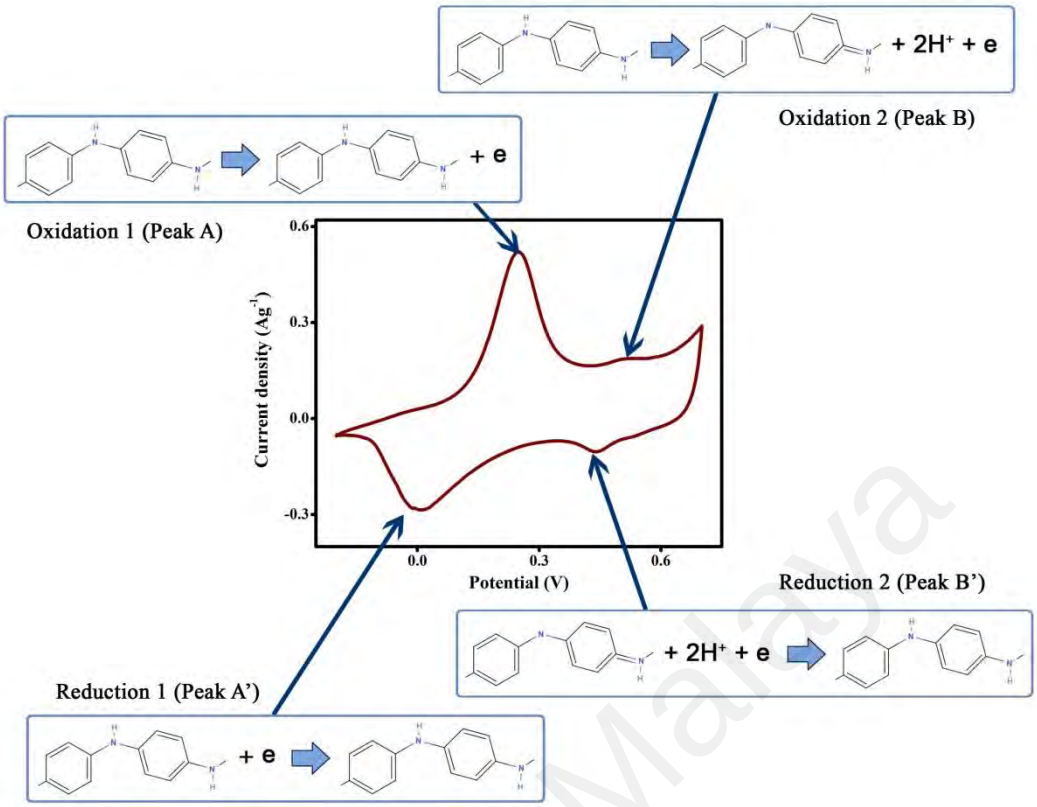

Figure 4.8: Cyclic voltammetry curves of polyaniline in 0.5 M H_2SO_4 showing two redox couples.

Figure 4.9 shows the CV curves of all samples at 1 mV s^{-1}. The tests were conducted at potential range of -0.2 to 0.7 V in 0.5 M H_2SO_4 electrolyte.

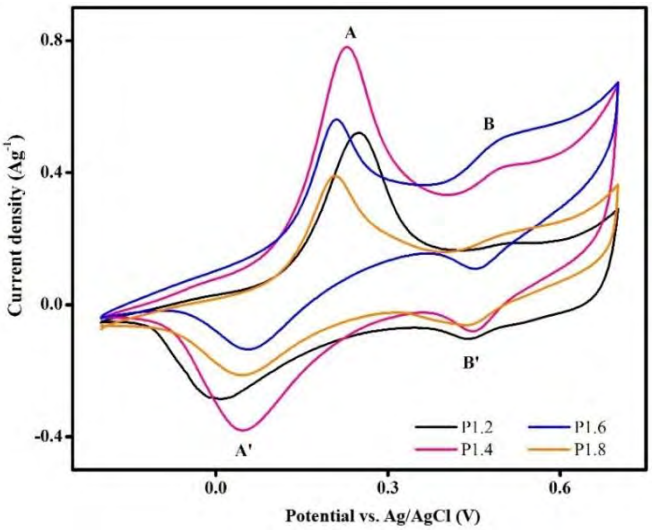

Figure 4.9: CV profiles of P1.2, P1.4, P1.6, and P1.8 at 1 mV s^{-1} scan rate.

From the figure, two sets of redox peaks are observed. Those peaks are attributed to the pseudocapacitance behavior of the samples. These redox activities imply the capacity for ideal supercapacitor-like behavior (Miao, et al., 2013).

The specific capacitance is calculated using Equation 4.1.

$$C_s = \frac{\int ivdv}{2\mu m \Delta V} \tag{4.1}$$

Where *Cs* represents the specific capacitance (F g^{-1}), *i* is the response current (A), *v* is the potential (V), μ is the scan rate (mV s^{-1}) and *m* is the mass of active material of the electrode (g). The calculated specific capacitances from the CV curves were 114 F g^{-1}, 136 F g^{-1}, 134 Fg^{-1} and 87 F g^{-1} at the scan rate of 1 mV s^{-1} for P1.2, P1.4, P1.6, and P1.8 electrodes in 0.5 M H_2SO_4 electrolyte, respectively.

The evenly distributed PANI structure on the P1.4 electrode is believed to result in the high accessibility of electrolyte cations into the electrode and result in an increased in the rate of ion exchange. Meanwhile, lower specific capacitances were found for the P1.6 and P1.8 electrodes which may be due to a PANI structure of agglomerated nanorods and high electrode resistance.

The CV profiles of P1.4 and its corresponding specific capacitance at various applied scan rates are displayed in Figure 4.10. As the scan rate increased, the specific capacitance decreased, which is due to the fast ion sweep, therefore less active materials are being assessed at higher scan rate (Umeshbabu, et al., 2015b).

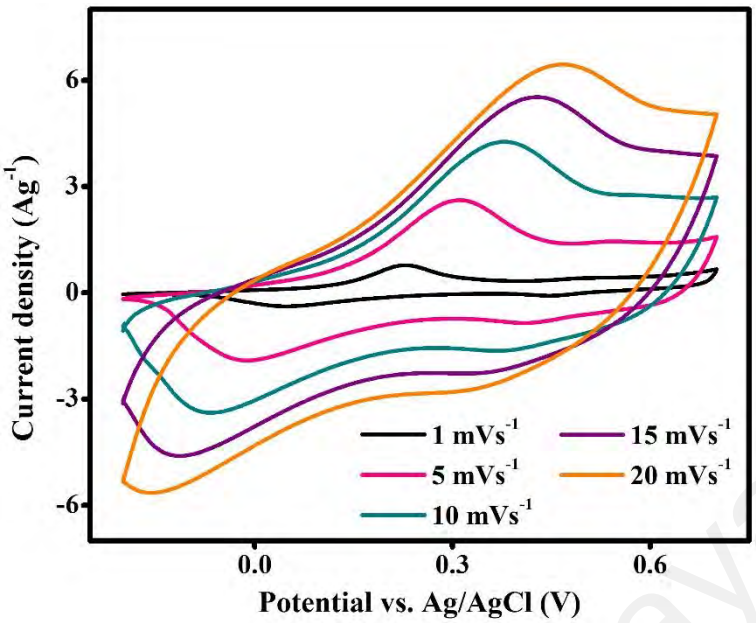

Figure 4.10: CV profiles of P1.4 at different scan rates.

From the CV curves at various scan rates, it is observed that the peak current increases with increment of the scan rate. There are also gradual expansion of the cathodic peak potential. This indicates diffusion controlled reaction kinetics (Adhikari, et al., 2017) process took place.

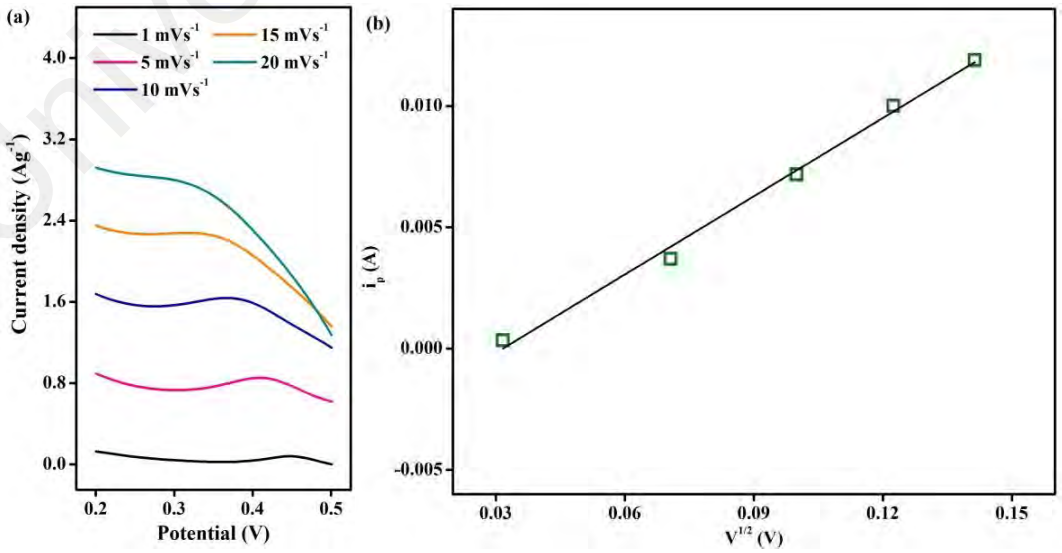

Figure 4.11: (a) Cathodic peak (B') of CV curve for P1.4 at different scan rates and (b) current peak vs square root of scan rate.

The diffusion control process relates the peak current to the square root of the scan rate, $v^{1/2}$ (Figure 4.11 (a)), via the Randles-Sevcik (Adhikari, et al., 2017; Randles, 1948) as shown in Equation 4.2.

$$i_p = 0.4463nFAC\left(\frac{nFvD}{RT}\right)^{\frac{1}{2}} \quad (4.2)$$

where *n* is the number of electrons appearing in half-reaction for the redox couple, *F* and *R* is the Faraday's and gas constants, *v* is the sweep rate, *C*, *D* is the concentration and the diffusion coefficient of the diffusing species. *A* is the surface area of electrode. The slope and hence the diffusion coefficient *D* for P1.4 was (~D = 0.00063 cm^2 s^{-1}). As evident from Figure 4.11 (b), the linear behavior of the curve shows presence of diffusion controlled process in PANI structures.

4.2.9 Galvanostatic charge-discharge

Galvanostatic charge discharge (GCD) characterizations were performed to study the storage capacity of the prepared electrode. Figure 4.12 displays the GCD curves of all samples in 0.5 M H_2SO_4 at 0.5 A g^{-1} current density in potential window of -0.2 V to 0.7 V. The GCD curve possessed a non-linear charge that is in consistence with the CV profile and can be validated as pseudocapacitance contributed from the electrode.

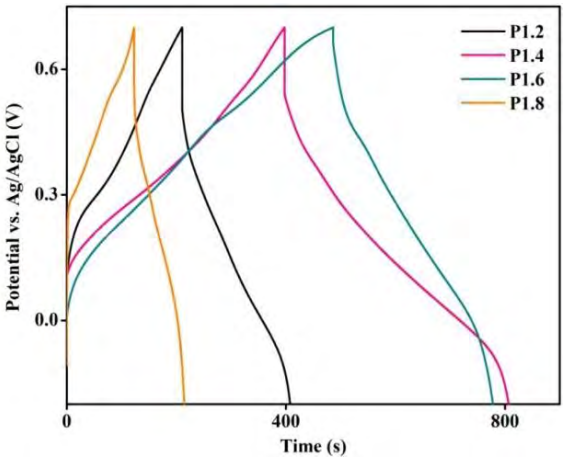

Figure 4.12: GCD curves of P1.2, P1.4, P1.6 and P1.8 at 0.5 A g^{-1}.

The specific capacitance is calculated using Equation 4.3 and shown in Figure 4.13.

$$C_s = \frac{I \times t}{m \times \Delta V} \tag{4.3}$$

Where C (F g^{-1}) is the specific capacitance, I is the current applied (A), Δt is the time taken during discharge process (s), m stands for the mass of active material (g) and Δv is the potential difference (V).

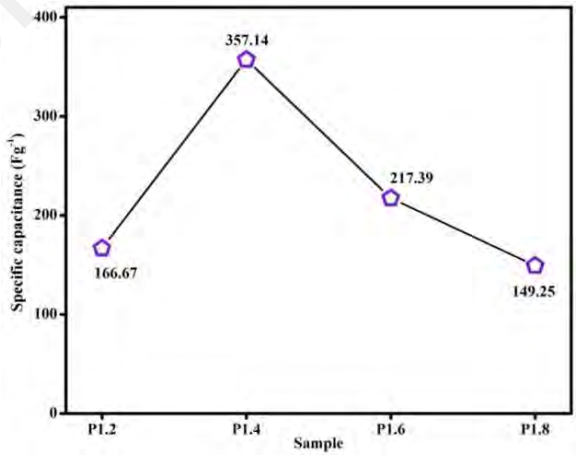

Figure 4.13: Specific capacitance of P1.2, P1.4, P1.6 and P1.8 at 0.5 A g^{-1}.

Specific capacitances (F g^{-1}) of the electrode with respect to the current densities (A g^{-1}) at which they were measured are as displayed in the Table 4.1.

Table 4.1: Specific capacitance calculated at 0.5 A g^{-1} and 1.0 A g^{-1} current density**.**

Sample	Specific capacitance (F g^{-1})	
	0.5 A g^{-1}	**1.0 A g^{-1}**
P1.2	166.67	153.85
P1.4	357.14	322.58
P1.6	217.39	204.08
P1.8	149.25	149.25

The calculated specific capacitances from the CD curves are concurring with the CV results. The calculated values focusses on the effect of the potential applied during the sample preparation. The specific capacitance increased when the potential applied is at 1.4 V. This might be implying to the uniformity of grown PANI in which provides adequate active site for H^+ ion absorption. However, the specific capacitance decreased as the deposition potential applied increased. This is probably due to the agglomeration of PANI deposited which restricted the ion absorption as evidenced in FESEM images.

GCD curves measured at different current densities for sample P1.4 showed almost similar trend in the charging and discharging profiles, Figure 4.14.

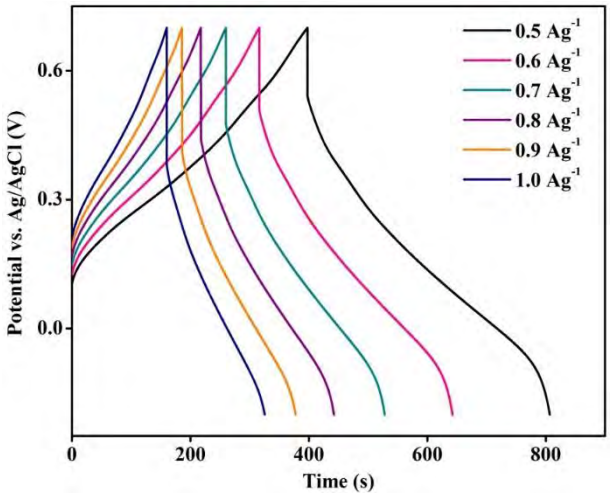

Figure 4.14: GCD curves of P1.4 at different current densities.

The specific capacitance of sample P1.4 at the current density of 0.5 A g^{-1} are 357.14 F g^{-1} and 322.58 F g^{-1} for 1.0 A g^{-1}, Figure 4.15. With the interval of current density from 0.5 to 1.0 A g^{-1}, the C_s retention is 90%. High capacitance retention of 90% indicates good charge storage capacity which might due to fast charge transfer related to the increment in current densities (Ma, et al., 2016; Wang, et al., 2017).

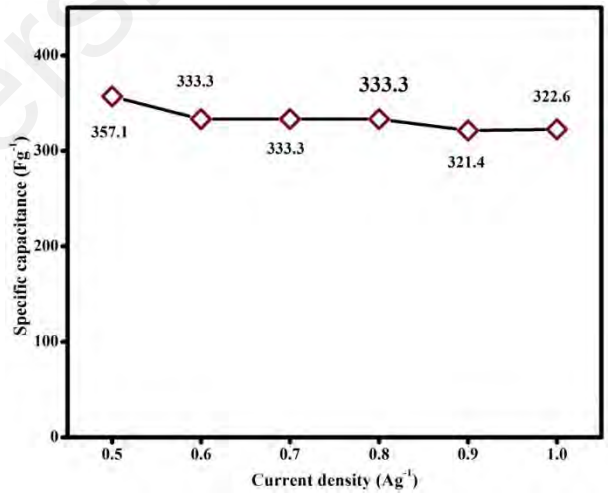

Figure 4.15: Calculated specific capacitance of P1.4 at different current densities.

The energy and power density of P1.4 at the current density of 0.5 A g^{-1} are 40.18 mW h kg^{-1} and 1.28 W kg^{-1}. At the current density of 1.0 A g^{-1}, the calculated energy density and power density are 36.29 mW h kg^{-1} and 0.64 W kg^{-1}.

4.2.10 Electrochemical impedance spectroscopy

Figure 4.16 (a) presents the Nyquist plots of the samples which can reveal the electron transmission in the bulk of the electrode and the ion diffusion at the interface of electrode and electrolyte. Generally, the Nyquist plot consists of an incomplete semicircle at high-frequency region and a sloped line over the low frequency region (Chen, et al., 2008; Liu, et al., 2014; Lv, et al., 2015).

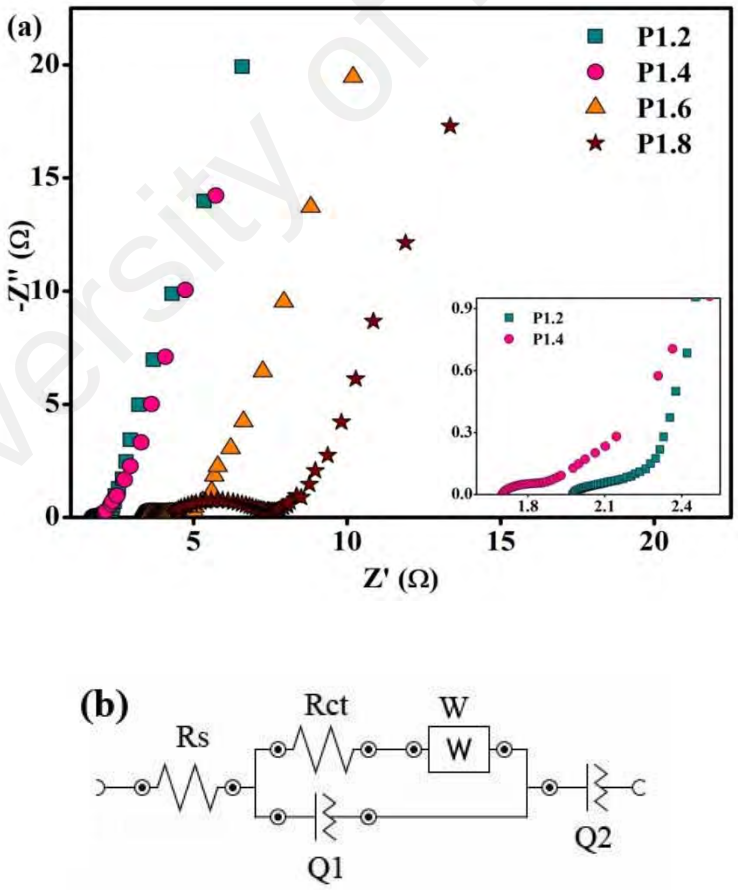

Figure 4.16: (a) Nyquist plot of all deposited samples and (b) circuit model of fitted Nyquist plot.

The Nyquist plots obtained is shown in figure have been fitted with the circuit model, Figure 4.16 (b). The data generated is displayed in Table 4.2. As shown in the figure, the semicircle of sample P1.4 is smaller compared to other samples. This implies that sample P1.4 has the lowest value of charge-transfer resistance of 0.20 Ω thus has the best kinetic properties. The good electrochemical performance might be due to the uniform nanowire morphology of P1.4 sample which is conducive to diffusion of electrolyte ion which is in agreement with the FESEM results.

Table 4.2: List of R_{ct} and R_s values of all deposited samples.

Sample	R_{ct} (Ω)	R_s (Ω)
P1.2	0.24	1.80
P1.4	0.20	1.58
P1.6	3.20	5.07
P1.8	3.50	4.17

4.2.11 Cycle studies

Cycle studies are important in investigation of supercapacitor life time. A symmetrical cell of P1.4//PVA+0.5 M H_2SO_4//P1.4 was fabricated and continuously cycled for 2000 times of charging and discharging process. The cell displays a good retention stability under continuous cycling at different current densities. Figure 4.17 shows the retention plot of the cell at all current densities.

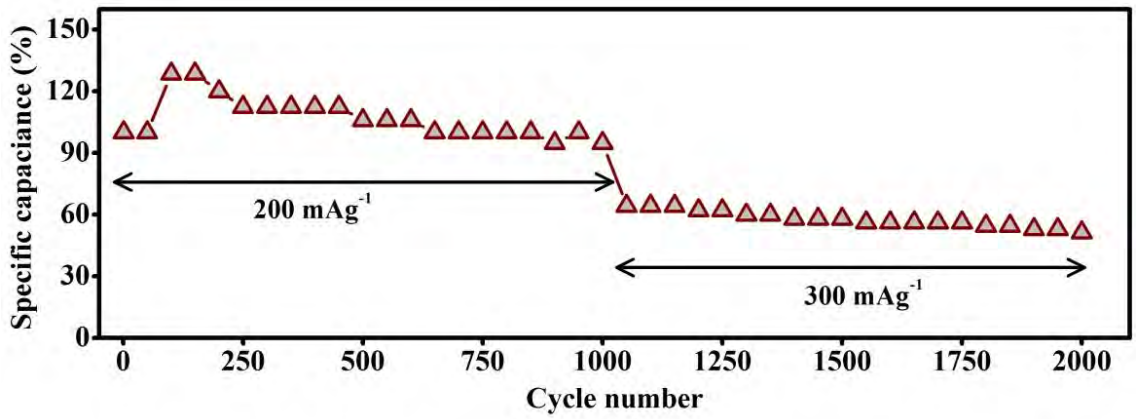

Figure 4.17: Retention plot for symmetric cell P1.4//PVA+0.5 M H_2SO_4//P1.4 at different current densities.

The cell was firstly cycled at 200 mA g^{-1} and then continued at 300 mA g^{-1}. The specific capacitance undergoes slight increment at 100^{th} and 150^{th} cycle, 129% of the initial value. This might be due to the occurrence of activation process in the cell (Zheng, et al., 2009b). The specific capacitance value was gradually dropped by the cycle and retained 95% specific capacitance of the initial cycle after 1000 continuous cycles at current density of 200 mA g^{-1}. A slight attenuation in specific capacitance of the initial cycle is observed when the cell was cycled at 300 mA g^{-1}. The value maintained throughout the following 1000 cycles with 88% implying good electrochemical performance of P1.4 electrode.

4.3 Nickel oxide-polyaniline composite embedded on carbon fiber cloth electrode

4.3.1 Introduction

PANI electrodes have been attracting the attention of researchers due to their unique doping/dedoping behavior, environmental stability, high conductivity and ease of synthesis. Having PANI being deposited straight onto a conductive substrate clearly exhibit a good specific capacitance value. However, directly deposited PANI has its own flaw as PANI will undergo rapid dissolution that contributes to low cycle rate of electrode. To overcome the situation, PANI can be coupled with another material to form a hybrid. Metal oxide is one of the best choices to act as a holder for PANI in order to prevent the dissolution effect and also able to contribute in the conductivity of the electrode (Ansari, et al., 2016; Wang, et al., 2016).

In this work, we grow nickel oxide on EC through hydrothermal method followed by electrodeposition of PANI via chronoamperometry mode. The influence of heat treatment on the morphology of the grown metal oxide has been systematically studied at different heating temperatures to obtain NiO-EC samples.

4.3.2 Nickel oxide growing and PANI electrodeposition mechanism

This section explains the steps involved in the fabrication of the electrode. Based on the observation, it is interesting to highlight the interaction between urea and Ni^{2+} ions which involve in the growing mechanism of the precursor $Ni(OH)_2$ synthesis. By acting as a precipitation agent, urea plays an important role in the process. $Ni(NO_3)_2 \cdot 6H_2O$ used in this work act as the source of Ni^{2+} ions besides having free water molecules being existed in the composite. Figure 4.18 shows the schematic diagram of the $Ni(OH)_2$ precursor and NiO growth mechanism.

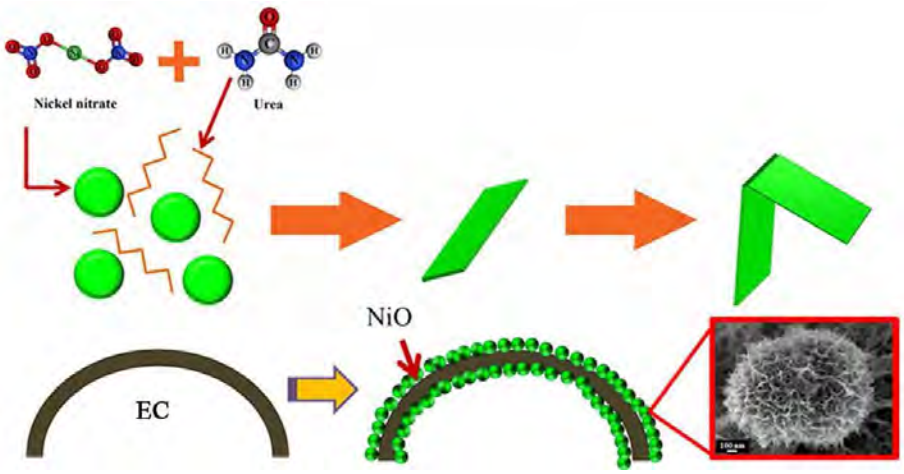

Figure 4.18: Schematic diagram of the NiO growth mechanism.

The reactions between nitrogen and oxygen atom in the polar groups of one urea unit occupy the empty orbitals of the metal ion in the solution which eventually forming coordinate bonds between urea and Ni^{2+} ions. On parallel occasion, the Ni^{2+} ions also unite with OH^- from the self-ionization of water simultaneously (Carotenuto, et al., 2000; Chandiramouli & Jeyaprakash, 2015; Latorre-Sanchez & Pomposo, 2015; Nwanya, et al. (2015)).

Afterwards, the nuclei grew larger, resulting the interactions to form networks under the heat application. This process leads to the formation of nanosheets product which followed by having self-oriented and assembled by degrees towards ordered flower-like structure to reduce the surface energy (Miao & Zeng, 2016). These processes occurred at the surface of the EC fiber resulting the flower-like structure of $Ni(OH)_2$ precursor to automatically grow on the EC without binder.

The mechanism of PANI electrodeposition started during the redox transition of leucoemeraldine and the polaronic emeraldine of PANI when potential is applied in the electrodeposition at specific time using electrolyte solution containing 0.5 M of aniline in H_2SO_4 with EC-NiO as the WE (Zhang, et al., 2013a; Zhao & Li, 2008).

Figure 4.19 displays the schematic diagram of the electrodeposition process of PANI on EC-NiO as the substrate together with the CA curve obtained from the electrodeposition process where the '*' indicates the point of the phase transitions from leucomeraldine to polaronic emaraldine (Zhang, et al., 2013a).

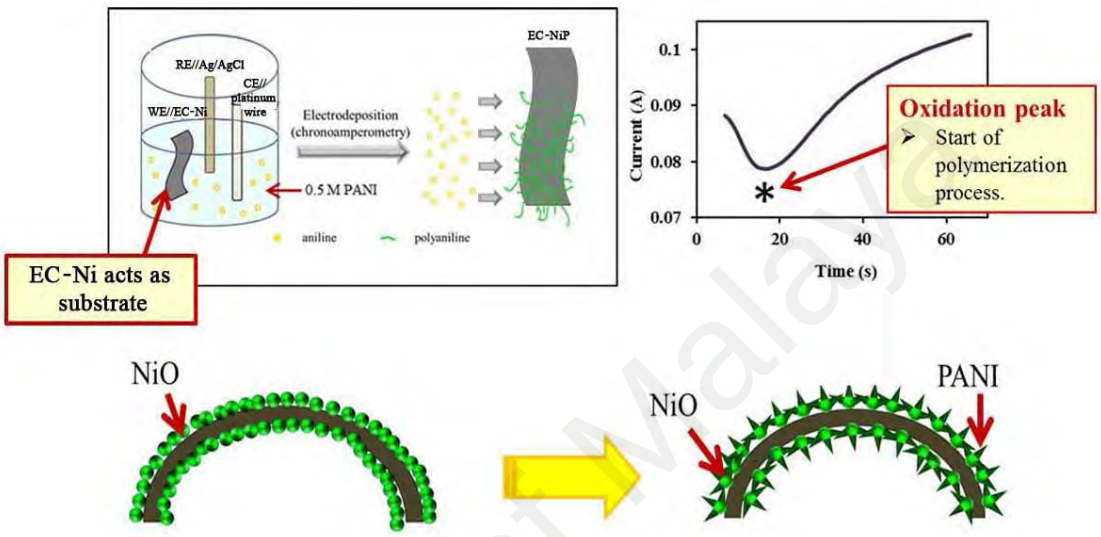

Figure 4.19: Schematic diagram for deposition mechanism of PANI onto EC-NiO, and (inset) CA curve of PANI electrodeposition process.

4.3.3 Thermogravimetric analysis

Thermal analyses of the prepared samples were conducted from room temperature to 800 °C. Figure 4.20 displays the TGA analysis conducted on $Ni(OH)_2$, EC, EC-NiO, and sample NiP300.

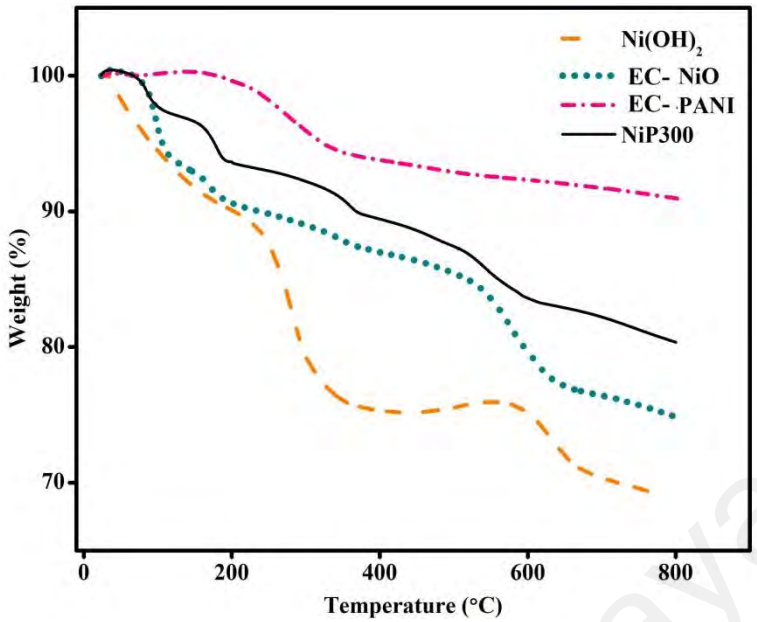

Figure 4.20: TGA spectra of $Ni(OH)_2$, EC-NiO, EC-PANI and sample NiP300.

The weight loss of 9 wt.% before 240 °C can be due to the dehydration of absorbed water on $Ni(OH)_2$ sample. The phase transformation of nickel hydroxide to nickel oxide can be inferred from major weight loss of 23 wt.% observed at 240 °C until 343 °C (Zhao, et al., 2011) according to Equation 4.4:

$$Ni(OH)_2 \rightarrow NiO + H_2O \qquad (4.4)$$

The same trend was observed in EC-NiO sample with the weight loss of 12 wt.% at 343 °C. This shows that this sample is more stable compared to $Ni(OH)_2$. 6 wt.% of weight loss observed on sample EC-PANI between 150 °C and 341 °C of is due to the deprotonation of the PANI losing dopant H_2SO_4. PANI then undergoes degradation after 341 °C which lead to loss of 10 wt.% that can be seen at the temperature from 341 °C to 800 °C. This is related to the PANI decomposition and degradation with different polymerization degree (Pandey, et al., 2005). In sample, NiP300, the initial weight loss from 77 °C to 191 °C is due to the evaporation surface-absorbed moisture molecule. Whereas, the weight loss of 11 wt.% from 191 °C to 368 °C is due to the loss of H_2SO_4

dopant and phase transformation of hydroxide to oxide from PANI and nickel, respectively, which occurred simultaneously.

4.3.4 X-ray diffraction

The chemical compositions of all samples were studied by X-ray diffraction (XRD) spectra. Figure 4.21 displays the XRD spectra of EC, NiO, EC-PANI and deposited PANI after heat treatment at 200, 300, 400 and 500 °C. Peaks observed at 2θ=37.3°, 43.4° and 62.9° in all deposited samples can be assigned to the NiO plane of (111), (200) and (220) respectively (Hu, et al., 2016; Liu, et al., 2017a; Miao & Zeng, 2016).

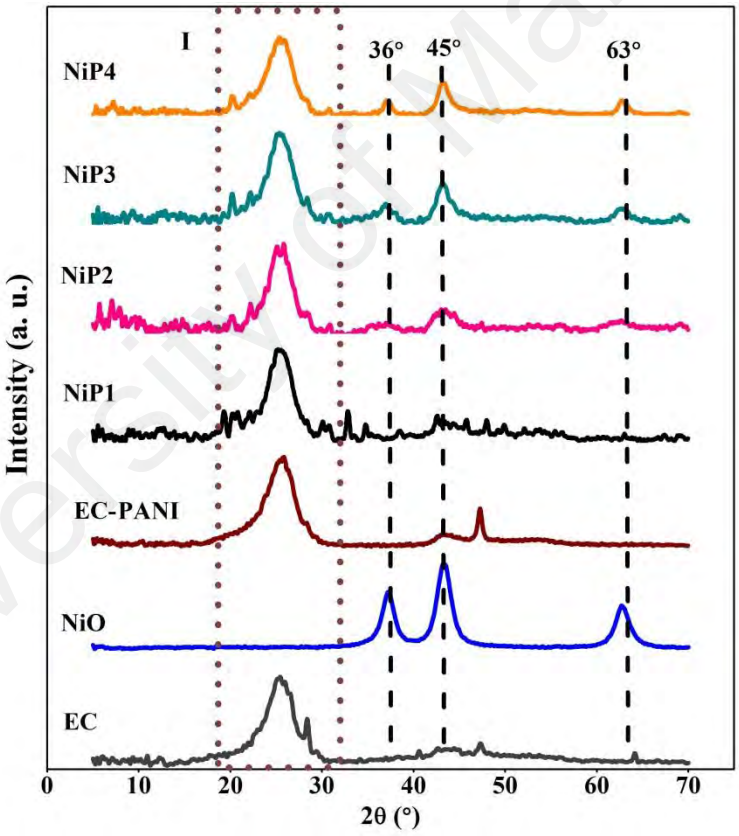

Figure 4.21: XRD diffractogram of EC, NiO, EC-PANI, NiP200, NiP300, NiP400 and NiP500.

As shown in the figure, the peaks became sharper as the temperature increased; implying a more ordered structure was formed (Xiao, et al., 2016). The characteristic peak of PANI and EC are present at 2θ= 25°.

Figure 4.22 shows the deconvoluted diffractogram at region X. Peak of PANI can be noticed at 2θ= 25.5° in which, the broad peak with low intensity indicating the formation of amorphous of PANI (Rusi & Majid, 2013; Zhang, et al., 2013a). The resolved peak observed at 2θ= 25° is corresponding to the (002) plane of carbon in EC which related to amorphous carbon materials with low degree of graphitization (Ding, et al., 2012; Gan, et al., 2015; Guo, et al., 2015; Jiang, et al., 2016; Lai & Lo, 2015; Zhou, et al., 2014b). Changes in intensity and shape of these peaks have proven the formation of NiO_PANI on EC substrate.

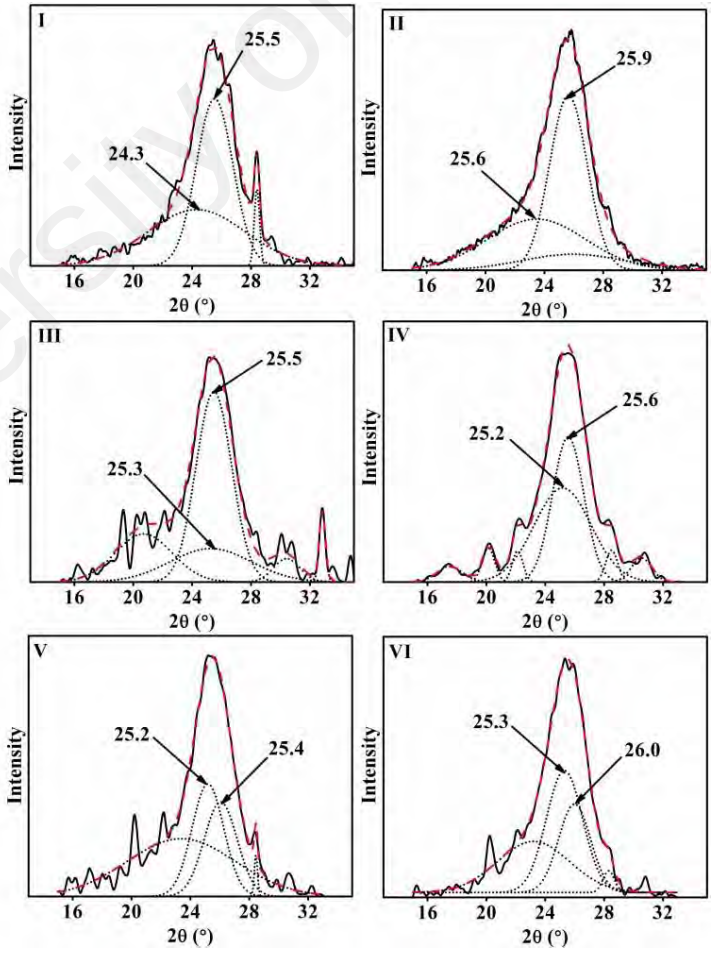

Figure 4.22: Deconvoluted diffractogram on region X of (I) EC, (II) EC-PANI, (III) NIP200, (IV) NIP300, (V) NIP400 and (VI) NIP500.

To further investigate the structural changes of sample during heating process, evolution of the crystal size (B) at different heating temperatures was calculated using Scherrer Equation 4.5 and shown in Table 4.3.

$$B(2\theta) = \frac{K\lambda}{L\cos\theta} \tag{4.5}$$

The calculation is based on the peak of $2\theta = 43.4°$. In general, the crystallite size will increase with the increasing of heating temperature (Marotti, et al., 2006). The table shows that the calculated crystallite size of each sample has a strong relationship with the heating temperature. The variation in size for NiO is between 2.18 and 17.50 nm over the temperature range of 200 to 500 °C. The crystallite size of NiO increases linearly from 300 °C until the heating temperature reaches 500 °C. The smaller crystallite size provides higher surface area for ion penetration leads to higher specific capacitance which is in a good agreement with other reports (Meher, et al., 2011; Pan, et al., 2010).

Table 4.3: Crystal size with respect to the heating temperature of electrodes NiP200, NiP300, NiP400 and NiP500.

Sample	Crystal size (nm)
NiP200	17.50
NiP300	2.18
NiP400	5.29
NiP500	6.10

4.3.5 Energy dispersive X-ray spectroscopy

The elemental composition of the deposit obtained from EDX is shown in Figure 4.23 (a and b). The element of carbon, sulphur, nickel, and oxygen are found which belongs to EC-Ni, Figure 4.23 (a). There are additional nitrogen and oxygen elements in NiP300 electrode, where the nitrogen observed is originated from PANI and oxygen might be from the adsorption of moisture by PANI, Figure 4.23 (b). In order to see clearly the evidence of deposited PANI, FTIR has been investigated.

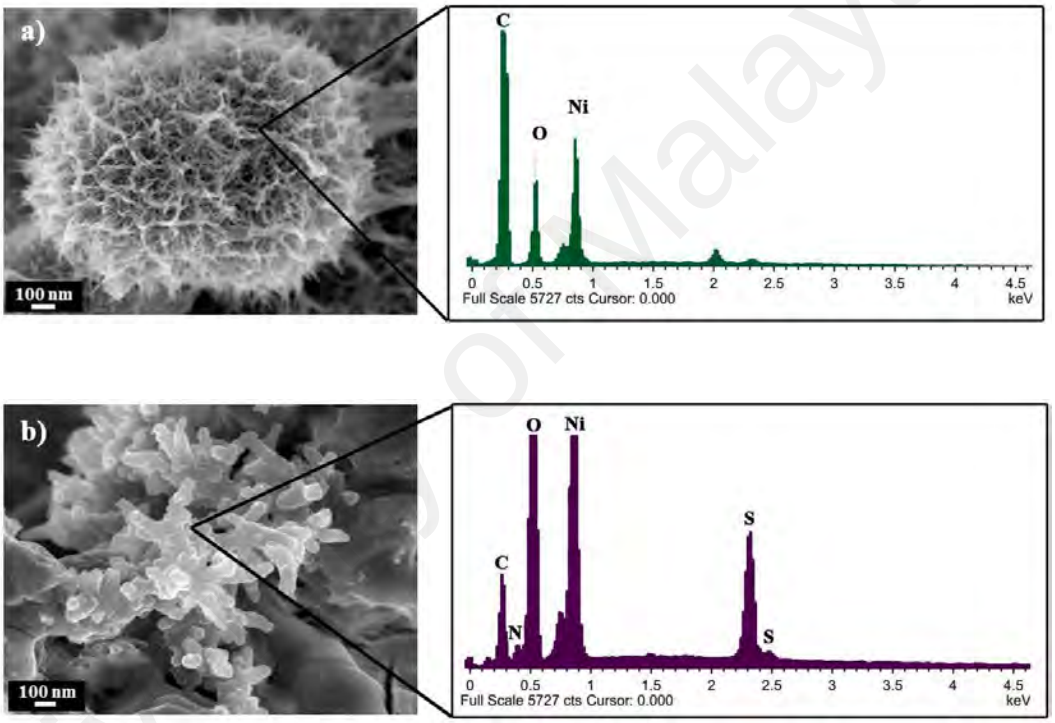

Figure 4.23: EDX spectrum of (a) NI300 and (b) NIP300.

4.3.6 Fourier transform infrared spectroscopy

FTIR analyses of the electrodes were conducted to verify the formation of NiO and PANI on EC. The spectra are shown in Figure 4.24 (a). In the spectrum of EC, the prominent band at 2325, 2088 and 1992 cm^{-1} are due to the typical C=C group which can be associated with carbon material. In the spectrum of EC-NiO, the intensity of these three peaks is decreasing and remains at its position in all studied samples.

For most of the oxide's characteristic, the transmittance bands are positioned at the lower wavenumber (Basharat, et al., 2015). Hence, the bands that occurred at 656 and 717 cm^{-1} are assigned to the bonding between Ni and O (Basharat, et al., 2015).

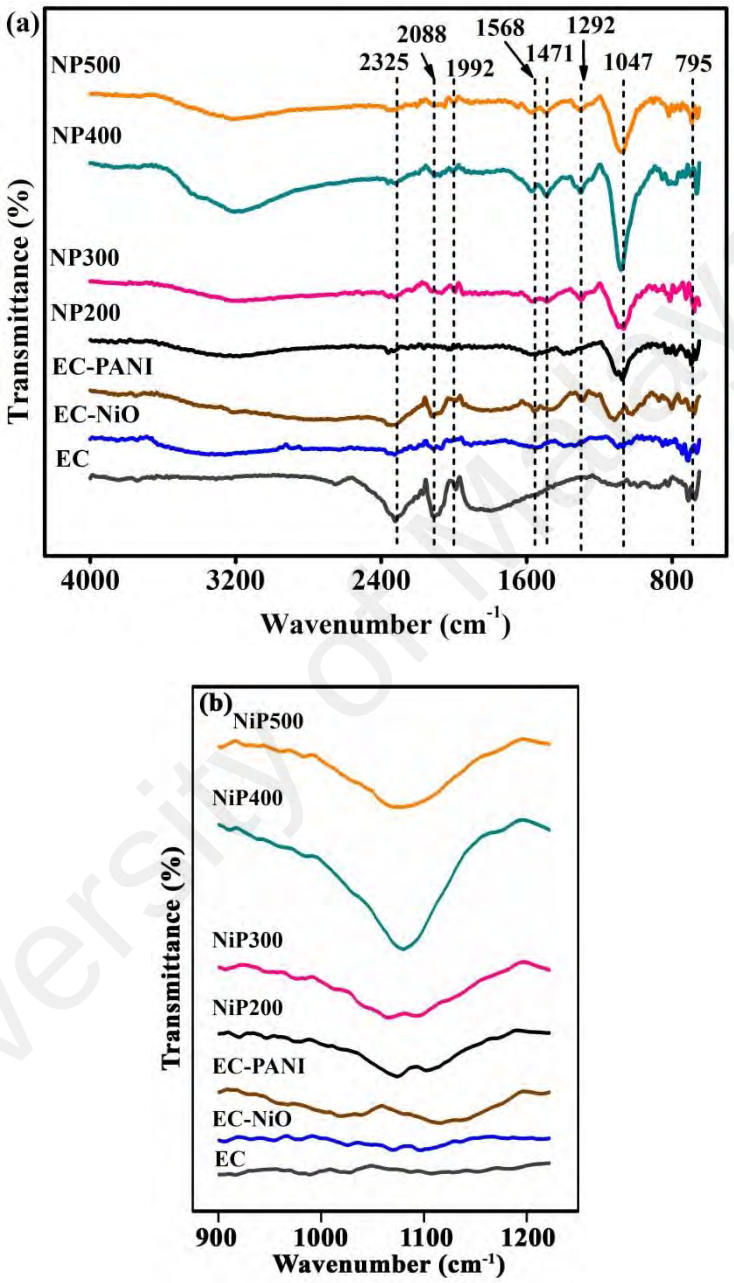

Figure 4.24: (a) FTIR spectra of NiO, EC, EC-NiO, EC-PANI and all prepared samples at wavenumber of 650-3200 cm^{-1} and (b) at 900-1220 cm^{-1}.

The FTIR spectrum of EC-PANI shows characteristic bands located at 1568, 1471 and 795 cm^{-1} are assigned to the C=C stretching vibration of quinoid rings, C=C stretching of benzoid rings and *p*-substituted ring of PANI respectively (Xing, et al., 2004). FTIR spectra of the samples in the region between 900 to 1220 cm^{-1} is shown in Figure 4.24 (b).

The deconvoluted spectrum of NiO powder is shown in Figure 4.25 (I). Four bands located at 1033, 1046, 1068 and 1103 cm^{-1} are seen. To further confirm the bands, the spectrum of NiO on EC substrate is deconvoluted, Figure 4.25 (II). Bands at 1049 and 1069 cm^{-1} remain at the same position, however,the intensity become lower for 1049 cm^{-1} and higher for 1069 cm^{-1}. Meanwhile, four intensive bands at 962, 1023, 1113 and 1155 cm^{-1} were resolved from this region for sample EC-PANI as shown in Figure 4.25(III). Bands at 962 and 1155 cm^{-1} are attributed to C-H out of plane and C-N stretching of second aromatic amine of PANI (Neelgund & Oki, 2011).

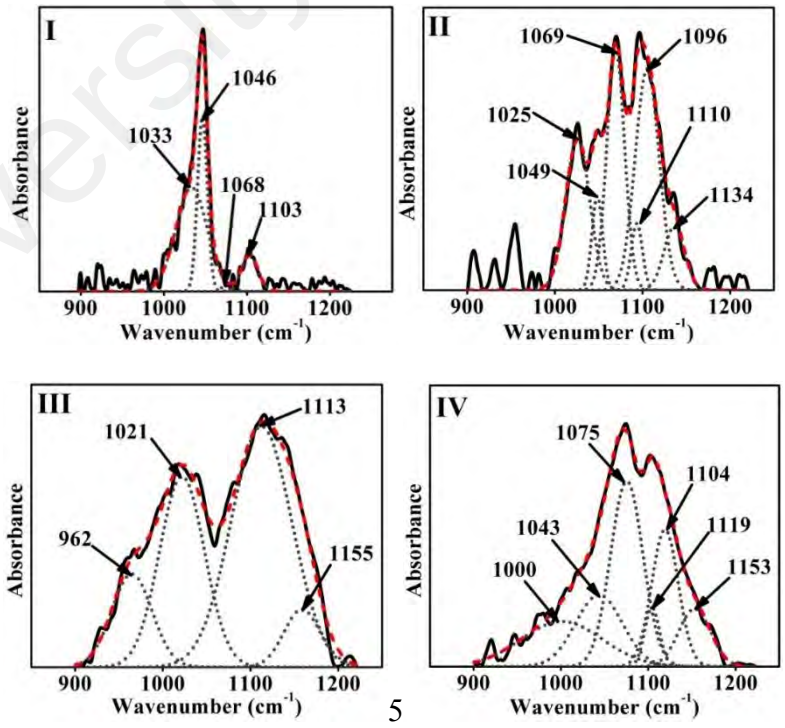

5

Figure 4.25: Deconvoluted FTIR spectra of (I) pure NiO, (II) EC-NiO, (III) EC-PANI, (IV) NiP200, (V) NiP300, (VI) NiP400 and (VII) NiP500.

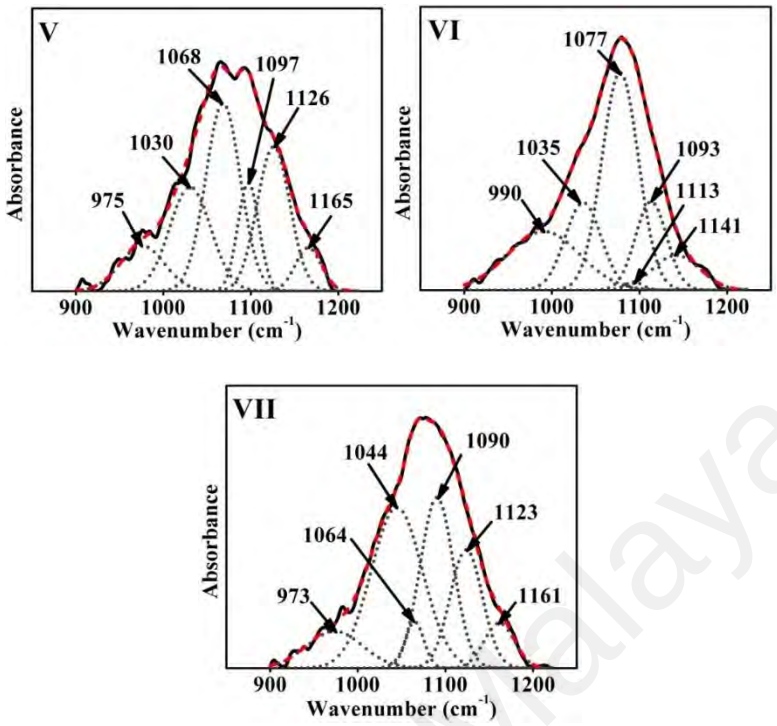

Figure 4.25, continued.

The spectrum of samples consist of EC, NiO and PANI heated at 200 °C (NiP200), Figure 4.25 (IV) reveals absorption band at 1037 cm^{-1} which can be attributed to the C-O stretching bond of NiO and PANI . This band appeared at the same wavenumbers in all prepared samples. Similar observation also occurred for band at 1068 cm^{-1} where no significant changes can be detected in terms of position and intensity. . Intensity of the band at 1110 cm^{-1} of EC-NiO for sample NiP200 is observed to increase. The two bands at 1134 and 1113 cm^{-1} belong to EC-NiO and PANI, respectively, have merged and centered at 1126 cm^{-1}. Band at 1110 cm^{-1} from EC-NiO and NiP200 spectra later combined together with the band at 1126 cm^{-1} in samples heated at higher temperature. While in sample NiP300, peak at 1155 cm^{-1} get shifted to higher wavenumber, 1165 cm^{-1} without any changes in the remaining two samples (NiP400 and NiP500).

4.3.7 Raman spectroscopy

The chemical structure of the NiCC_PANI is further explored by using Raman spectra as shown in Figure 4.26.

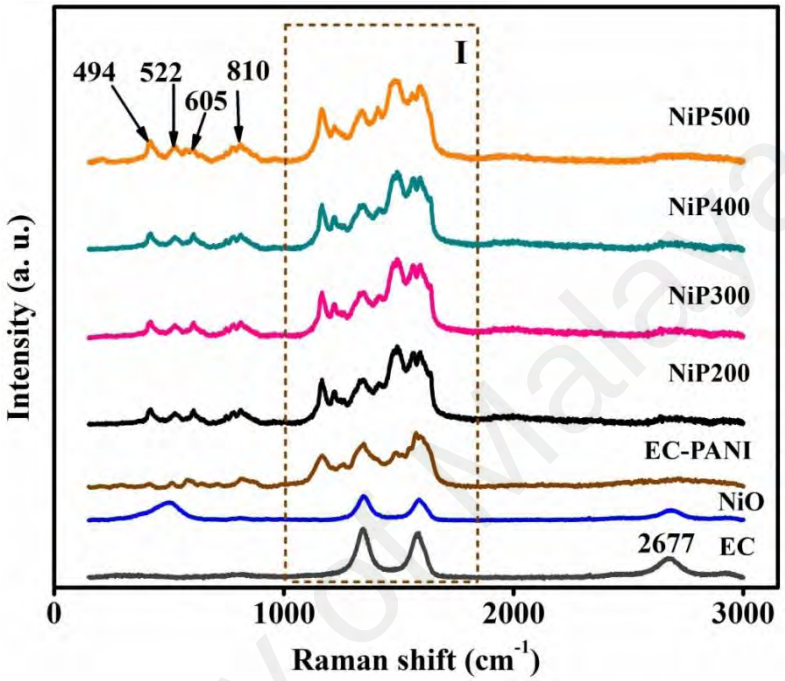

Figure 4.26: Raman spectra of EC and all deposited PANI electrodes.

From the figure, three peaks were observed in all spectra located at ~1345 cm^{-1}, ~1579 cm^{-1} and ~2673 cm^{-1} which correspond to EC. This is due to the formation of semiquinone radical cations, that is, the p-disubstituted benzene rings. Five small peaks located at ~494 cm^{-1}, ~522 cm^{-1}, ~605 cm^{-1} and ~810 cm^{-1} are observed in G band, D band and 2D band, which corresponding to the peaks of NiO. Peaks 490 cm^{-1} and 520 cm^{-1} are assigned to the first-order transverse optical (1TO) and longitudinal optical (1LO) phonon modes of NiO, respectively while peak 600 cm^{-1} and 810 cm^{-1} are attributed to the second order transverse optical (2TO) longitudinal optical (2LO) phonon modes of NiO (Burmistrov, et al., 2015; Cazzanelli, et al., 2003; Dietz, et al., 1971; Mironova-Ulmane, et al., 2011).

One broad pocket of peaks in region I (900-2100 cm^{-1}) is deconvoluted and displayed in Figure 4.27 to distinguish the overlapped peaks between NiO and PANI.

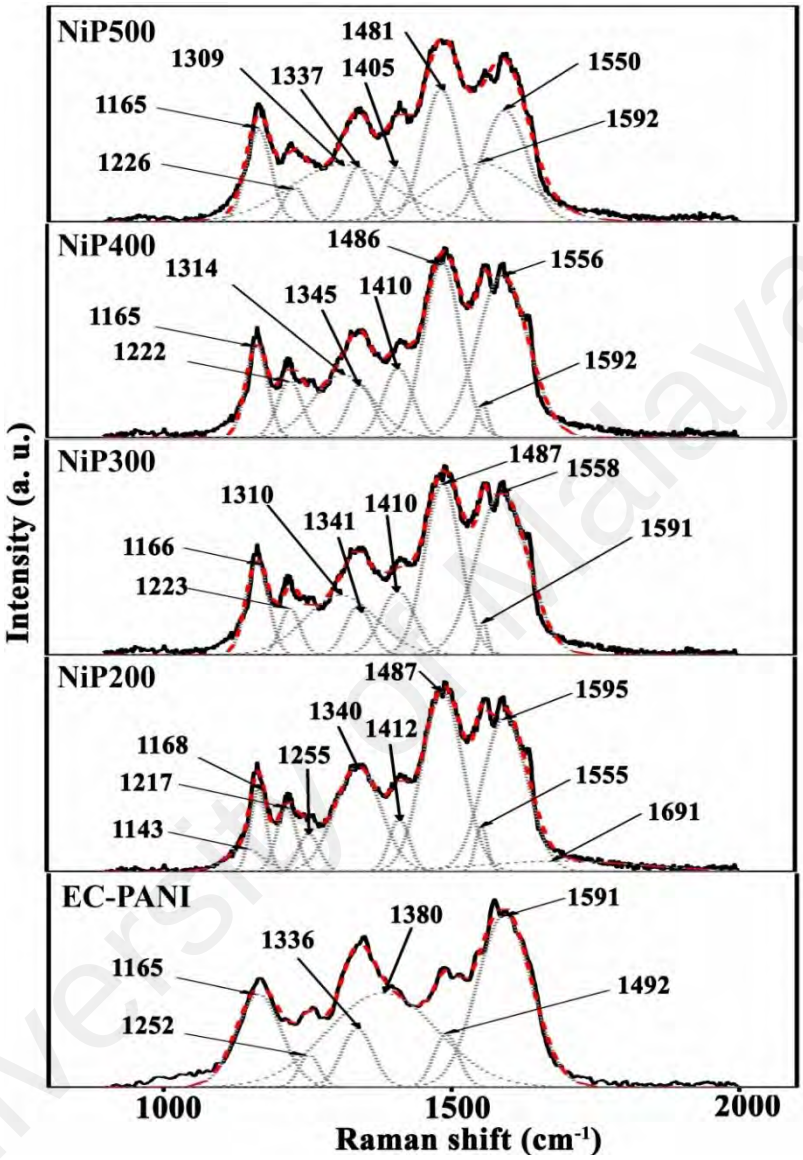

Figure 4.27: Deconvoluted spectra at region I of CCE-PANI and all prepared samples.

Peaks located at ~1165 cm^{-1}, ~1314 cm^{-1}, 1492 cm^{-1} and ~1555 cm^{-1} are believed to be originated from NiO. Peaks at 1165 cm^{-1} and 1492 cm^{-1} are associated with two-phonon scattering and the excitation of two magnons respectively while 1314 cm^{-1} and

1492 cm^{-1} are observed in D band and G band respectively (Burmistrov, et al., 2015; Kudin, et al., 2008; Zhou, et al., 2014a).

The characteristic bands of PANI can be seen at 1143 and 1217 cm^{-1} which can be referred to C-H bending modes. Rings of C-C stretching mode can be captured at 1591 cm^{-1} while for C-N stretching mode is observed at 1380 cm^{-1}. The conductive property of PANI can be detected in the region from 1100 to 1150 cm^{-1} which can be indicated as the delocalization of charge on the polymer backbone (Kar & Choudhury, 2013).

4.3.8 Field-emission scanning electron microscopy

The morphology of our electrode was investigated through FESEM study (Figure 4.28 and Figure 4.29). Figure 4.28 (a1) reveals the nanoflower-like shaped NiO formed on sample Ni300 by growing it directly on the EC. Same shape also can be seen from sample Ni400 (Figure 4.28 (b1)) but in a more densely packed order as shown in Figure 4.28 (b2) compared to Ni300 (Figure 4.28 (a2)) where the plates are more loosely arranged hence providing more spaces for PANI deposition.

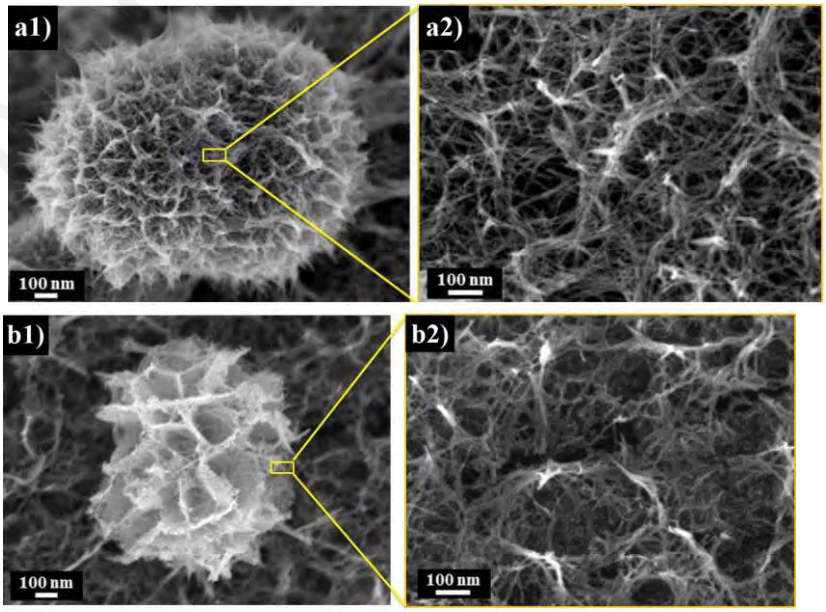

Figure 4.28: FESEM images of (a1) Ni300 with (a2) inset and (b1) Ni400 with (b2) inset at X 50 000 and X 200 000 magnification.

This situation is proven in Figure 4.29 (b1) where sample NiP300 has uniform pattern of PANI deposition. The deposited PANI is able to fill up the gap between the plates provided by the NiO that has grown beforehand. In due course, more uniform shape and well-developed nanowire of PANI inevitably gives more area for electrolyte contact when electrochemical analysis took place.

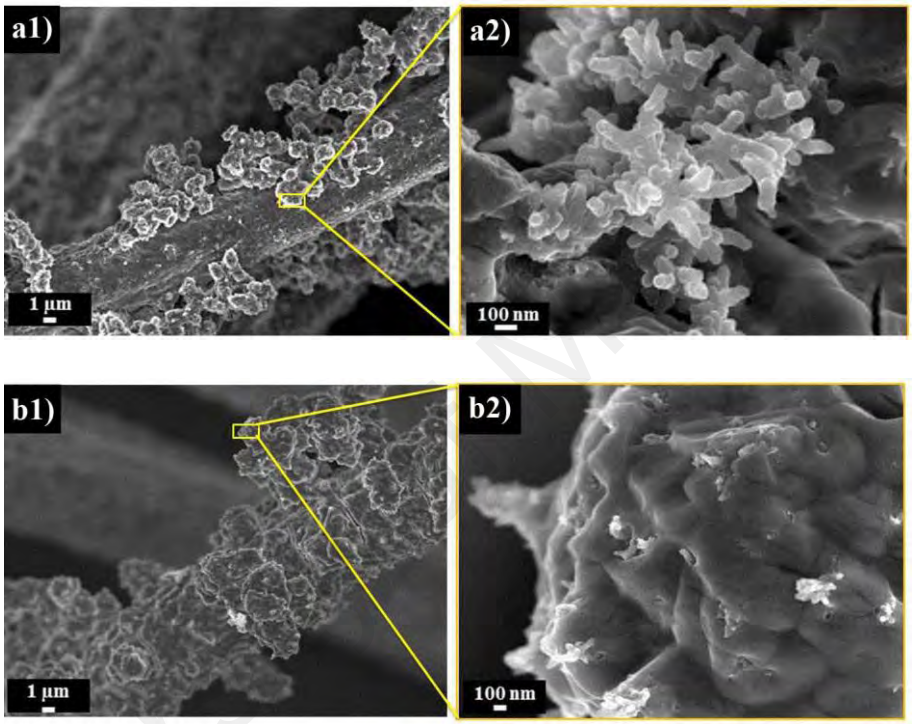

Figure 4.29: FESEM images of (a1) NiP300 with (a2) inset and (b1) NiP400 with (b2) inset at X 3000 and X 30 000 magnification.

Unlike in the case of sample NIP400 (Figure 4.29 (b1)), the PANI deposited is not in uniform condition. Agglomeration occurred on the surface of the electrode which might be due to the limitation of spaces provided by the NiO for PANI to attach. This leads to PANI being unable to grow well on its substrate, hence decreases the area for electrolyte contact among the active electrode material which automatically gives low specific capacitance value.

4.3.9 Transmission electron microscopy

A representative TEM image of the selected electrode is shown in Figure 4.30. This figure verified that deposited PANI had built up from small PANI nanowire, which is in agreement with FESEM results.

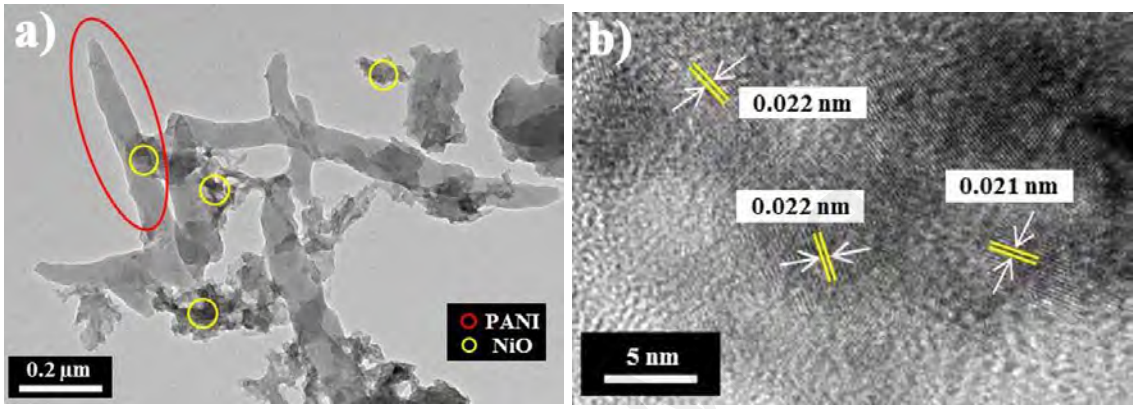

Figure 4.30: TEM images of NIP300 at (a) low and (b) high magnification.

This figure verified that deposited PANI had built up from small PANI nanowire, which is in agreement with FESEM results. From these structural studies, heating temperature was shown to strongly influence the morphology and porosity of the deposits. It is believed that these factors will affect the PANI electrodeposition process which influences the electrochemical performance.

4.3.10 Cyclic voltammetry

CV, GCD, EIS and cycle stability tests have been carried out to evaluate the electrochemical behavior of the samples.

The CV was measured at the period potential from -0.2 to 0.7 V in 0.5 M H_2SO_4 electrolyte at scan rates of 1 to 20 mV s^{-1}. Figure 4.31 (a) shows CV profile of all samples at scan rate of 1 mV s^{-1}. From the figure, two pairs of redox peaks marked as A/A' and

B/B' were observed showing pseudocapacitance property. Peak A/A' can be attributed to the conversion of leucomeraldine to emaraldine of the PANI chain, while the B/B' peak is due to the emaraldine-pernigraniline transformation (Yu, et al., 2016).

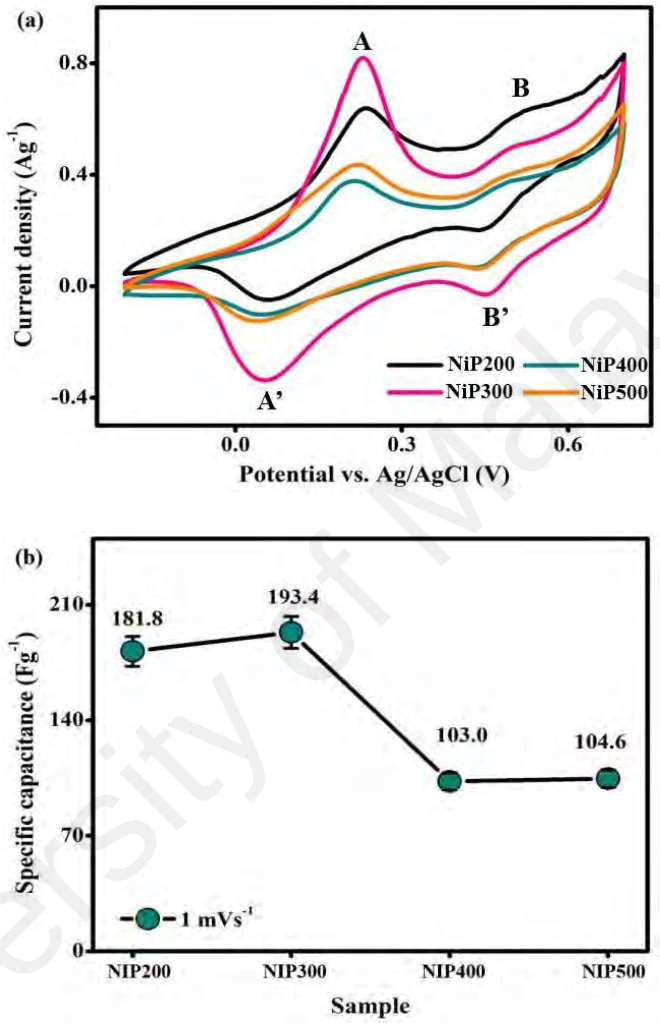

Figure 4.31: (a) CV profiles of NIP200, NIP 300, NIP400 and NIP500 and (b) calculated specific capacitance at scan rate of 1 mv s^{-1}.

The electrochemical performance of the electrodes were measured in terms of specific capacitance (C_s). The C_s based on CV curves were calculated using equation (4.1). The mass of active materials is in between 0.00645 g to 0.00800 g. The calculated C_s at a scan rate of 1 mV s^{-1} is presented in Figure 4.31 (b). As can be seen, the highest C_s value of 193.38 F g^{-1} was obtained by the NiP300 sample, at a scan rate of 1 mV s^{-1}. Figure

4.32 shows the CV profile of NiO-PANI electrode system at higher scan rate, 10 mV s^{-1} in which slight changes can be observed.

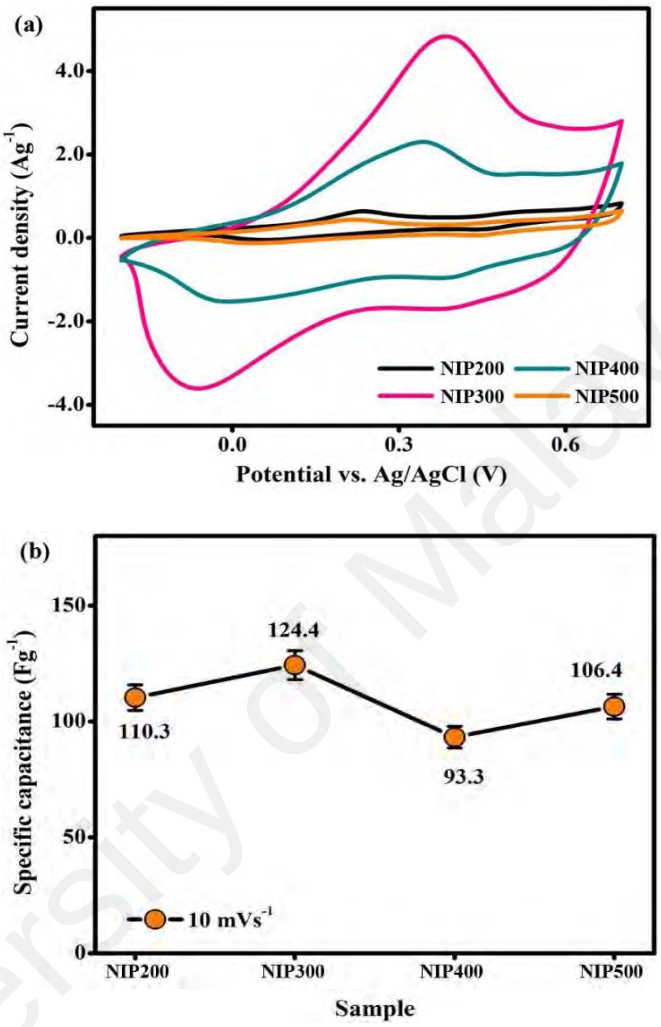

Figure 4.32: (a) CV profiles of NiP200, NiP300, NiP400 and NiP500 and (b) calculated specific capacitance at scan rate of 10 mv s^{-1}.

Figure 4.32 (a) shows that the anodic and cathodic peaks shifted to higher and lower potential respectively. Despite the deviations, same trend of C_s is observed in all samples measured at 10 mV s^{-1}, Figure 4.32 (b). Sample NiP300 still possess highest specific capacitance of 124.36 F g^{-1}. In order to get more information on the electrochemical behavior of the electrodes, a series of CV with different scan rates from 1 to 20 mV s^{-1} were also conducted on sample NiP300 and is displayed in Figure 4.33.

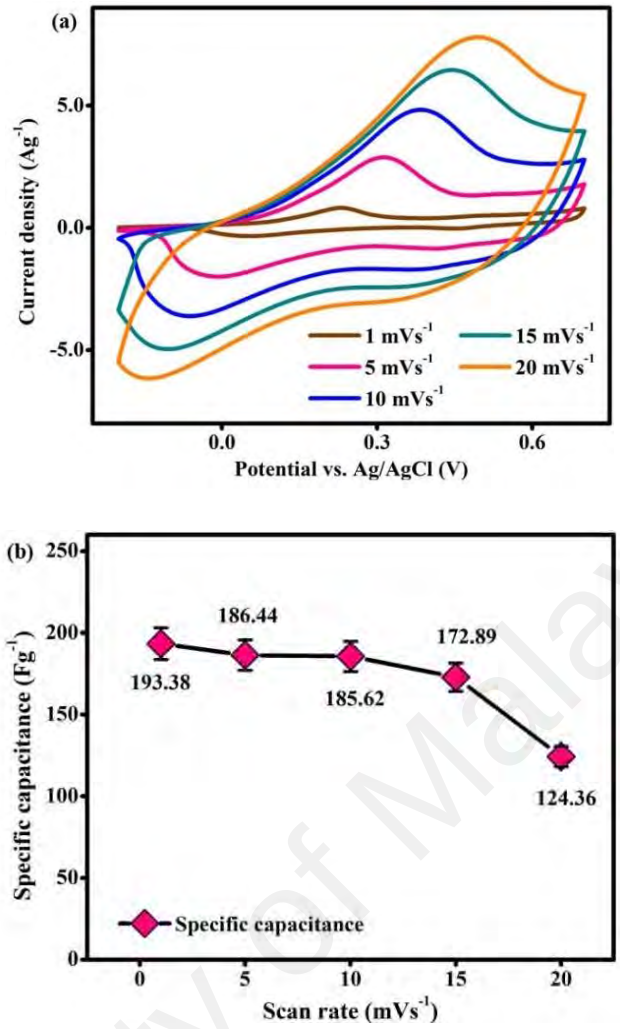

Figure 4.33: (a) CV curves of NiP300 at various scan rates and (b) plot of its specific capacitance versus different scan rate applied in 0.5 M H_2SO_4 electrolyte.

The CV profile in Figure 4.33 (a) shows unambiguous anodic and cathodic peaks which can be inferred to the redox activity contributed from faradaic reaction of the sample (Zhou, et al., 2004). As the scan rate increased from 1 to 20 mV s^{-1}, the anodic and cathodic peak experienced some changes in their intensity and positions.

The anodic peak shows increment in its current peak value and shifted to higher potential. On the other hand, the current value of cathodic peak experienced decrement and also shifted to the lower potential region. This observation might be due to the strengthened electric polarization and kinetic irreversibility of ions originating from the electrolyte at the electrode's surface while undergoing redox reaction at higher scan rates

(Umeshbabu, et al., 2015a). The shape of the CV curves progressively transformed into a rectangle at higher scan rate. The C_s values of electrode NiP300 measured at different scan rates are displayed in Figure 4.33 (b). Lower scan rate exhibited higher specific capacitance.

4.3.11 Galvanostatic charge-discharge

Galvanostatic charge/discharge (GCD) measurements were conducted in order to investigate the charge storage capacity of the electrodes. Figure 4.34 (a) presents the GCD curves at current density of 0.5 A g^{-1} in the potential windows ranging from -0.2 to 0.7 V.

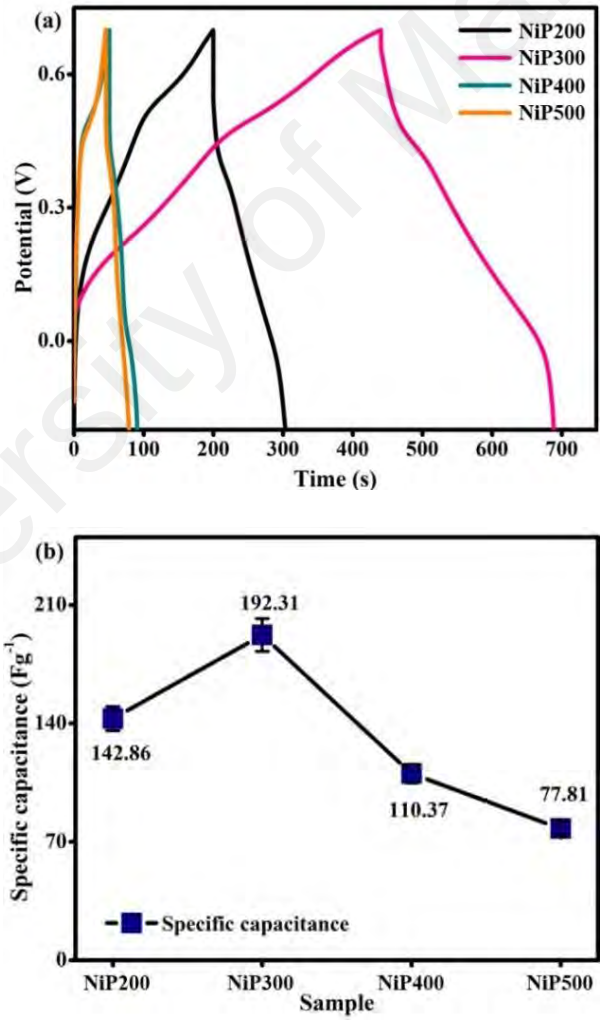

Figure 4.34: GCD profiles of NiP200, NiP300, NiP400 and NiP500 at current density of 0.5 A g^{-1} and (b) calculated specific capacitance.

The non-linear charge and discharge curve is consistent with the peaks marked at the CV profile which can be corroborated to pseudocapacitance behavior which was contributed by the electrode. The specific capacitance obtained for samples NiP200, NiP300, NiP400 and NiP500 are calculated using Equation 4.3. The values were plotted in Figure 4.34 (b). The specific capacitance highlight the effects of heating temperature during electrode preparation since C_s increased as heating temperature increased to 300 °C. This might be associated to the uniformity of grown PANI that provides sufficient active site for a better absorption of H^+ ion. The increment of specific capacitance can also be inferred to the small crystal size.

At higher heating temperatures of 400 and 500 °C, the specific capacitance value are observed to drop due to the enlargement of crystal size as previously mentioned in XRD results. This situation will lead to PANI agglomeration due to the ineffective PANI deposition onto the NiO surfaces. Hence, the utilization of active sites for electrolyte ion absorption/desorption will be reduced (He, et al., 2012). Therefore, the calculated specific capacitance of sample NiP400 and NiP500 (110.37 F g^{-1} and 77.81 F g^{-1}) are found to be lower than sample NiP300 (192.31 F g^{-1}) measured at 0.5 A g^{-1} in 0.5 M H_2SO_4. High specific capacitance achieved by sample NiP300 is due to the efficient ion charge transfer provided by the ordered PANI nanorods on NiO (Ma, et al., 2016).

Comparison of GCD curves at different current densities for sample NiP300 show almost similar trend in the charging and discharging profiles, Figure 4.35. The specific capacitance of sample NiP300 at current density of 0.5 and 1.0 Ag^{-1} are 192.3, and 185.2 F g^{-1} respectively. With the interval of current density from 0.5 to 1.0 Ag^{-1}, the specific capacitance retention is 96%. High capacitance retention indicates good charge storage capacity which might be due to fast charge transmission related to the increment in current densities (Ma, et al., 2016). The same observation has been reported in other

works such as Xue and coworkers (Xue, et al., 2012), Han and coworkers (Han, et al., 2014), as well as Ma and coworkers (Ma, et al., 2016) for PANI based composite electrodes. The energy and power density of NiP300 at current density 0.5 Ag^{-1} are 21.7 mW h kg^{-1} and 4.8 W kg^{-1} respectively. While for current density 1.0 A g^{-1}, the energy density calculated was 20.8 mW h kg^{-1} with 2.4 W kg^{-1} of power density.

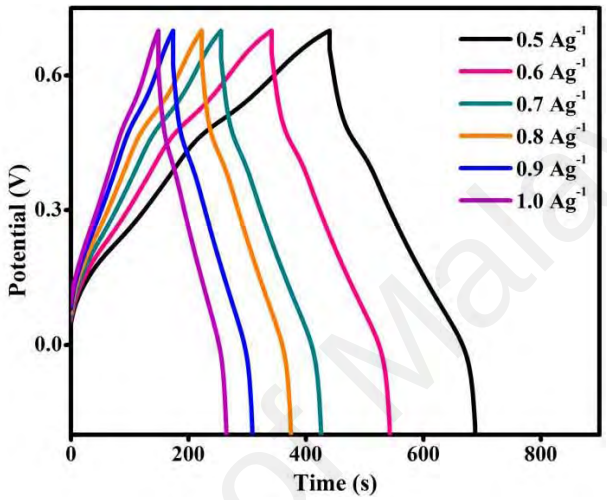

Figure 4.35: CD curves of NiP300 at various current densities.

4.3.12 Electrochemical Impedance Spectroscopy (EIS)

The EIS study of the electrodes in 0.5 M H_2SO_4 electrolyte is shown in Figure 4.36. All plots exhibited similar electrochemical impedance characteristics where ordinary semicircle and oblique line are presented at the high and low frequency, respectively. In high frequency region, there is an intercept of the arc on the x-axis called the equivalent series resistance (R_s), which represents a combination of ionic resistance of electrolyte, contact resistance, and internal resistance of the material (Pandit, et al., 2017). However, transfer resistance (R_{ct}) is obtained from the electrochemical reaction resistance that can be inferred from the high frequency semicircle (Pandit, et al., 2017). Lines with slopes greater than 45° observed at low frequency can be ascribed to the diffusion and kinetics process called the Warburg impedance (W) (Girija & Sangaranarayanan, 2006).

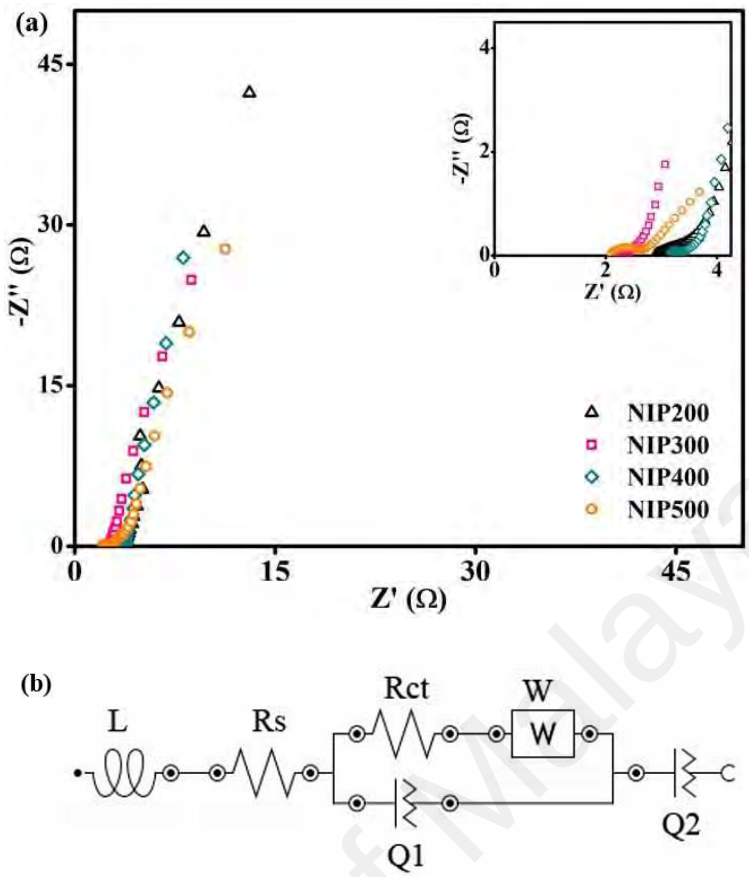

Figure 4.36: (a) Nyquist plot of all samples and (b) its equivalent circuit.

The equivalent circuit of the fitted curve is displayed in Figure 4.36 (b). The R_{ct} values of sample NiP200, NiP300, NiP400 and NiP500 are 3.00 Ω, 2.07 Ω, 2.79 Ω and 2.22 Ω, respectively. NiP300 electrode with the lowest R_{ct} value is the most convenient sample for diffusion and migration of electrons. Thus, these characteristics contribute to the best electrochemical performance, corresponding to the CV and charge-discharge results as mentioned in the previous section. The uniform deposition of PANI on the electrode also plays an important role in better accessibility of cations to the electrode matrix (Zhou, et al., 2004), which also parallels with the FESEM result.

4.3.13 Cycle studies

A symmetrical NiP300//PVA+0.5 M H_2SO_4//NiP300 cell was fabricated and tested for 4500 cycles continuously under different current densities of charging and discharging process. This cycling stability test was carried out using NiP300 electrode with total mass load of 0.0114 g. The cell shows good retention stability after continuous cycling at various current densities as can be observed from Figure 4.37.

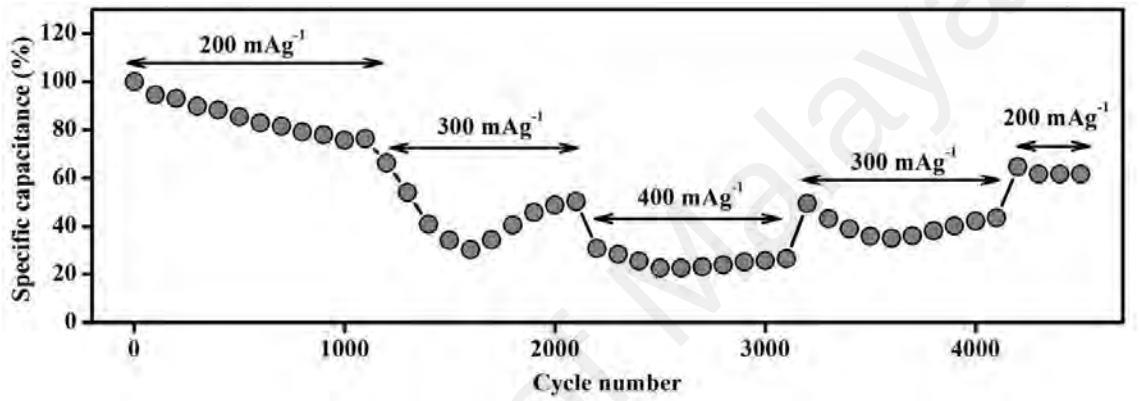

Figure 4.37: Retention graph of 4500 cycles of symmetric cell of EC-NiP at different current density in PVA+0.5 M H_2SO_4 gel electrolyte.

The sequence of the charge and discharge cycles begins at 200 mA g^{-1} followed by 300 and 400 mA g^{-1}. The current densities were reversed to 300 and 200 mA g^{-1} within 1000 cycles continuously. The specific capacitance for the first 1000 cycles at 200 mA g^{-1} decreased by 27% of the initial cycle. During the next 1000 cycles at 300 mA g^{-1}, the specific capacitance experienced a decrement of 46%, especially from 1000^{th} to 1500^{th} cycle. In the next 500 cycles, the value gradually increased to 66% of the initial capacitance. This is possibly due to the activation process that happened during the cycling process. This situation occurred as a result of insufficient utilization of NiO during the early cycles (Zheng, et al., 2009b). The values of specific capacitance for the subsequent current densities are calculated to be 76% and 82% of initial capacitance,

respectively. When the current density is switched back to 200 mA g^{-1}, the cell is able to store the charge and retained approximately 72% of the initial capacitance. This indicates that the specific capacitance only experienced a slight attenuation hence implying good electrochemical performance of NiP300 electrode even after being tested at high current densities.

The EIS measurements of fabricated cell were carried out before and after 4500 cycles in the frequency range from 0.01 Hz to 10 kHz. Figure 4.38 (a) and (b) shows the Nyquist curve of NiP300//PVA+0.5 M H_2SO_4//NiP300 cell before and after the cycle process. The specific capacitances at various frequencies were calculated and presented in Figure 4.38 (c).

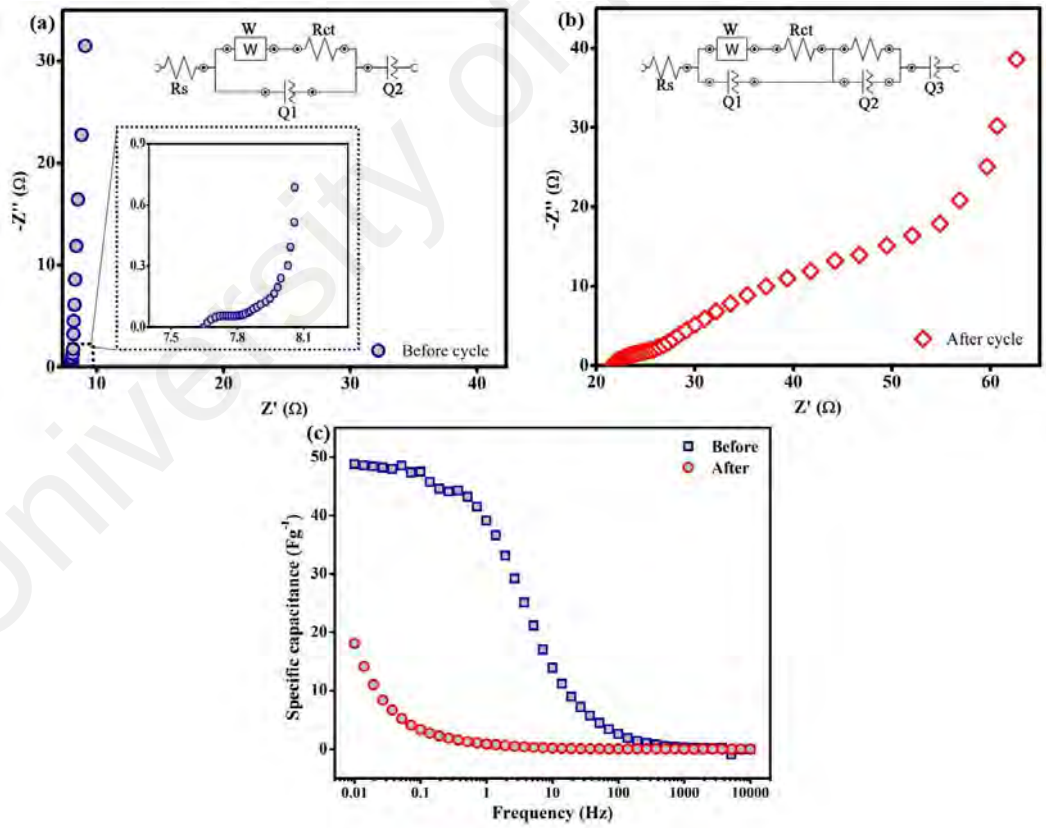

Figure 4.38: Nyquist plot of EC-NiP symmetric cell (a) before, (b) after cycling process and (c) plot of specific capacitance vs. frequency.

After 4500 continuous cycle of the symmetrical cell, the Nyquist curve has shifted towards higher resistance values. The broadening of the high-frequency semicircle was also observed as R_{ct} value increased from 0.3 to 4.0 Ω after the cycle. This can be ascribed to the larger resistance resulted from the repeated charge-discharge processes. As can be seen from Figure 4.38 (b), the second semicircle with resistance value of 31.0 Ω appeared in the Nyquist plot after 4500 cycles. This semicircle indicates that interface layer was formed which affected the charge-discharge process. Hence, the specific capacitance retention value was decreased (Li, et al., 2015).

Figure 4.38 (c) shows the specific capacitance as a function of frequency (0.01 Hz–10 kHz) of NiP300//PVA+0.5 M H_2SO_4//NiP300 cell before and after 4500 cycles. Before cycle, the specific capacitance value was gradually decreased with frequency until 100 Hz and remained constant towards the end. This is due to the inability of ions from electrolyte to follow the electric field oscillations at higher frequencies (100 Hz – 10 kHz). A different trend was observed after 4500 cycles where the plateau region begins to appear at lower frequency number (0.1 Hz - 10 kHz). This is probably due to the increment of resistance which is in agreement with Figure 4.38 (a) and Figure 4.38 (b) as the R_{ct} value was found to be larger after the cycling stability process (Vello, et al., 2017).

Figure 4.39 shows the plot of energy and power density versus cycle number of NiP300//PVA+0.5 M H_2SO_4//NiP300 cell.

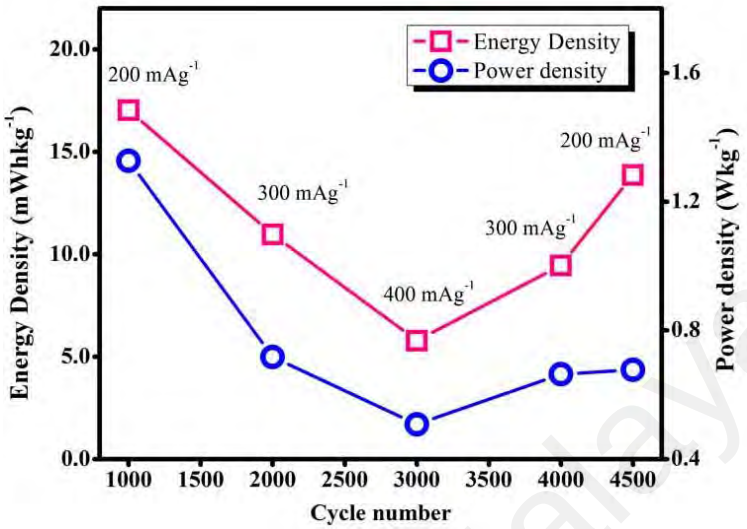

Figure 4.39: Energy and power density calculated for each 1000 cycles and 4500th cycle

From figure, it can be seen that both energy and power density of the cell decreased with respect to the increment of current density applied for each 1000 cycles. After the cell underwent 1000 cycles at current density of 200 mA g^{-1}, it delivers energy density of 17.04 mW h kg^{-1} with power density of 1.33 W kg^{-1}. As the current density increased to 300 mA g^{-1}, the energy density decreased to 10.97 mW h kg^{-1} with power density of 0.72 W kg^{-1}. The energy density was then decreased to 5.79 mW h kg^{-1} at 400 mA g^{-1} after 3000 cycles. When the current density returned to 200 mA g^{-1}, the cell successfully restored 13.87 mW h kg^{-1} energy density compared to the value of the first 1000 cycles.

It can be seen that the NiP300//PVA+0.5 M H_2SO_4//NiP300 cell has achieved an electrochemical reversibility with low resistance value. This might be due to the good synergistic effect between the NiO and PANI (Ma, et al., 2016). Besides that, the porous structure of carbon fiber cloth is expected to give a better diffusion of electrolyte into the

electrode material thus providing more channels for rapid ion transport (Cheng, et al., 2011).

4.4 Summary

The EC-PANI electrode was successfully deposited on EC using chronoamperometry mode. The P1.4 electrode deposited for deposition potential of 1.4 V was found to have uniform interconnected nanofiber structure. The electrochemical performance of P1.4 confirmed that it has better performance in ion diffusion with specific capacitance of 357.14 F g^{-1} at current density of 200 mA g^{-1} in 0.5 M H_2SO_4 electrolyte. Finally, symmetrical P1.4 cell was assembled and exhibited 95% of specific capacitance retention after 1000 cycles in PVA+0.5 M H_2SO_4 electrolyte at current density of 200 mA g^{-1}. The specific capacitance also retains 88% at current density of 300 mA g^{-1} for the next 1000 cycles.

The EC-NiO-PANI electrode was successfully grown on EC using hydrothermal method and chronoamperometry method. The EC-NiO electrode heated at 300 °C was found to have uniform nanoflower-like structure of NiO. The electrochemical performance of NiP300 confirmed that it has better performance in facilitating PANI deposition with specific capacitance of 192.39 F g^{-1} at current density of 200 mA g^{-1} in 0.5 M H_2SO_4 electrolyte. Symmetrical NiP300 cell exhibited good electrochemical reversibility when discharged at different current densities over 4500 cycles. The cell is also able to retain 72% of its initial capacitance after discharge current density is switched back to the initial value.

CHAPTER 5: CONCLUSION AND SUGGESTIONS FOR FUTURE WORK

5.1 Conclusions

In summary, all the objectives of the present study were achieved. This thesis focuses on the electrochemical performance of polyaniline based electrode materials for supercapacitor application. There are two electrode systems that have been fabricated and studied which are (1) EC-PANI electrode system and (2) EC-NiO-PANI electrode system.

The first objective was achieved from the electrode system (1). Different PANI structures have been obtained by varying the deposition potential of 0.5 M aniline on etched carbon cloth. The potential applied during the electrodeposition process is one of the important parameters that influence the electrodeposition rate and nucleation process, thus resulted in various morphologies. At low potential energy, low density of deposited PANI nanofiber was observed due to slow electrodeposition rate. The potential energy of 1.4 V was identified as a suitable potential value to produce uniform PANI nanofiber through chronoamperometry mode.

Two FTIR peaks at ~1540 and ~1446 cm^{-1} verified that PANI has been successfully deposited on the EC substrate. The formation of PANI is also supported by the XRD results in which peak centred at 2θ = ~25.5° has appeared in all samples to indicate the presence of PANI. Sample P1.4 exhibited the highest specific capacitance from the first electrode system with the value of 357.14 F g^{-1} at current density of 500 mA g^{-1}. The symmetric cell P1.4//PVA+0.5 M H_2SO_4//P1.4 showed good capacity retention of 88% after 2000 cycles.

In the next part of this work, a systematic study has been conducted in order to achieve the second objective. The effect of metal oxide deposition on the electrochemical behavior of PANI electrode was investigated on the composite electrode, EC-NiO-PANI (NiP) consists of grown NiO on EC (EC-NiO) which act as a supporting layer for PANI deposition. The optimization of heating temperature for NiO formation is achieved at 300 °C. At this temperature, the smallest crystal size was obtained from XRD peak calculation.

The specific capacitance of NiP300 electrode was 192.31 F g^{-1} at current density of 500 mA g^{-1} in 0.5 M H_2SO_4 electrolyte. Stability test of NiP300 was conducted symmetrically with PVA + 0.5 M H_2SO_4 as the electrolyte. The cell was tested for 4500 cycles continuously under different current densities. The cell was able to store the charge and retained 72% of the initial specific capacitance. After the cell underwent 1000 cycles at current density of 200 mAg^{-1}, it delivered energy density of 17.04 mW h kg^{-1} with power density of 1.33 W kg^{-1}. The cell successfully restored 13.87 mW h kg^{-1} of energy density compared to the value of the first 1000 cycles after 4500 cycles. This good stability and reversibility behavior is due to the uniform arrangement of nanofiber PANI on thin flakes of nanoflower-like NiO particles. The structure generated more porous network structure. The uniform nano-sized porous structure led to easy access of electrolyte cation transport to electrode matrices; hence a better ion diffusion performance was obtained.

5.2 Suggestions for future work

In this work, the deposition parameter and the heating temperature have been optimized for PANI based electrode systems. Overall, the good specific capacitance and energy density obtained in our research is suitable for supercapacitor application. However, there are many ways to improve the cycling performance of the electrode such

as compositing the PANI based electrode with carbonaceous material like graphene, CNT and MWCNT.

In other approach, the adhesion between the electrode surface and active material can be improved by adding sodium dodecyl sulfate (SDS) into deposition solution. Besides that, the optimized electrode from our studies can be used as electrode material for hybrid supercapacitor fabrication.

REFERENCES

Adhikari, H., Ghimire, M., Ranaweera, C. K., Bhoyate, S., Gupta, R. K., Alam, J., & Mishra, S. R. (2017). Synthesis and electrochemical performance of hydrothermally synthesized Co_3O_4 nanostructured particles in presence of urea. *Journal of Alloys and Compounds, 708*, 628-638.

Afriyanti, S., Yao, F. C., Xu, W., & See, L. P. (2013). Large areal mass, flexible and free‐standing reduced graphene oxide/manganese dioxide paper for asymmetric supercapacitor device. *Advanced Materials, 25*(20), 2809-2815.

Agilan, P., & Rajendran, N. (2018). In-vitro bioactivity and electrochemical behavior of polyaniline encapsulated titania nanotube arrays for biomedical applications. *Applied Surface Science, 439*, 66-74.

Aleshin, A. N. (2006). Polymer nanofibers and nanotubes: Charge transport and device applications. *Advanced Materials, 18*(1), 17-27.

Alqahtani, D. M., Zequine, C., Ranaweera, C. K., Siam, K., Kahol, P. K., Poudel, T. P., . . . Gupta, R. K. (2019). Effect of metal ion substitution on electrochemical properties of cobalt oxide. *Journal of Alloys and Compounds, 771*, 951-959.

An, G. H., Lee, D. Y., & Ahn, H. J. (2018). Hierarchically mesoporous activated carbon prepared from the dissolution of zinc oxide for high-rate electrical double layer capacitors. *Journal of Industrial and Engineering Chemistry, 65*, 423-428.

Ansari, S. A., Parveen, N., Han, T. H., Ansari, M. O., & Cho, M. H. (2016). Fibrous polyaniline@manganese oxide nanocomposites as supercapacitor electrode materials and cathode catalysts for improved power production in microbial fuel cells. *Physical Chemistry Chemical Physics, 18*(13), 9053-9060.

Arbizzani, C., Mastragostino, M., & Meneghello, L. (1996). Polymer-based redox supercapacitors: A comparative study. *Electrochimica Acta, 41*(1), 21-26.

Arnaiz, M., Botas, C., Carriazo, D., Mysyk, R., Mijangos, F., Rojo, T., . . . Goikolea, E. (2018). Reduced graphene oxide decorated with SnO_2 nanoparticles as negative electrode for lithium ion capacitors. *Electrochimica Acta, 284*, 542-550.

Augustyn, V., Simon, P., & Dunn, B. (2014). Pseudocapacitive oxide materials for high-rate electrochemical energy storage. *Energy & Environmental Science, 7*(5), 1597-1614.

Balint, R., Cassidy, N. J., & Cartmell, S. H. (2014). Conductive polymers: Towards a smart biomaterial for tissue engineering. *Acta Biomaterialia, 10*(6), 2341-2353.

Basharat, F., Rana, U. A., Shahid, M., & Serwar, M. (2015). Heat treatment of electrodeposited NiO films for improved catalytic water oxidation. *RSC Advances, 5*(105), 86713-86722.

Bláha, M., Trchová, M., Bober, P., Morávková, Z., Zujovic, Z. D., Filippov, S. K., . . . Stejskal, J. (2017). Structure and properties of polyaniline interacting with H-phosphonates. *Synthetic Metals, 232*, 79-86.

Burmistrov, I., Agarkov, D., Tartakovskii, I., Kharton, V., & Bredikhin, S. (2015). Performance optimization of cermet SOFC anodes: An evaluation of nanostructured NiO. *ECS Transactions, 68*(1), 1265-1274.

Capasso, C., Lauria, D., & Veneri, O. (2018). Experimental evaluation of model-based control strategies of sodium-nickel chloride battery plus supercapacitor hybrid storage systems for urban electric vehicles. *Applied Energy, 228*, 2478-2489.

Carotenuto, G., Pepe, G. P., & Nicolais, L. (2000). Preparation and characterization of nano-sized Ag/PVP composites for optical applications. *The European Physical Journal B - Condensed Matter and Complex Systems, 16*(1), 11-17.

Cazzanelli, E., Kuzmin, A., Mariotto, G., & Mironova-Ulmane, N. (2003). Study of vibrational and magnetic excitations in Ni c Mg 1− c O solid solutions by Raman spectroscopy. *Journal of Physics: Condensed Matter, 15*(12), C2045.

Chandiramouli, R., & Jeyaprakash, B. G. (2015). Operating temperature dependent ethanol and formaldehyde detection of spray deposited mixed CdO and MnO_2 thin films. *RSC Advances, 5*(55), 43930-43940.

Chang, L., Feng, L., Lai‐Peng, M., & Hui‐Ming, C. (2010). Advanced materials for energy storage. *Advanced Materials, 22*(8), E28-E62.

Chellachamy Anbalagan, A., & Sawant, S. N. (2016). Brine solution-driven synthesis of porous polyaniline for supercapacitor electrode application. *Polymer, 87*, 129-137.

Chen, X. L., Li, W. S., Tan, C. L., Li, W., & Wu, Y. Z. (2008). Improvement in electrochemical capacitance of carbon materials by nitric acid treatment. *Journal of Power Sources, 184*(2), 668-674.

Chen, Y., Xu, B., Wen, J., Gong, J., Hua, T., Kan, C.-W., & Deng, J. (2018). Design of novel wearable, stretchable, and waterproof cable-type supercapacitors based on high-performance nickel cobalt sulfide-coated etching-annealed yarn electrodes. *Small, 14*(21), Article#1704373.

Cheng, B.-H., Zeng, R. J., & Jiang, H. (2017). Recent developments of post-modification of biochar for electrochemical energy storage. *Bioresource Technology, 246*, 224-233.

Cheng, Q., Tang, J., Ma, J., Zhang, H., Shinya, N., & Qin, L.-C. (2011). Polyaniline-coated electro-etched carbon fiber cloth electrodes for supercapacitors. *The Journal of Physical Chemistry C, 115*(47), 23584-23590.

Chiang, J.-C., & MacDiarmid, A. G. (1986). 'Polyaniline': Protonic acid doping of the emeraldine form to the metallic regime. *Synthetic Metals, 13*(1), 193-205.

Childress, A., Ferri, K., & Rao, A. M. (2018). Helically coiled carbon nanotubes as supercapacitor electrodes. *Carbon, 140*, 377-384.

Chung, D. D. L. (2018). Development, design and applications of structural capacitors. *Applied Energy, 231*, 89-101.

Ćirić-Marjanović, G. (2010). Polyaniline Nanostructures *Nanostructured Conductive Polymers* (pp. 19-98): John Wiley & Sons, Ltd.

De Surville, R., Jozefowicz, M., Yu, L. T., Pepichon, J., & Buvet, R. (1968). Electrochemical chains using protolytic organic semiconductors. *Electrochimica Acta, 13*(6), 1451-1458.

Desilvestro, J., & Scheifele, W. (1993). Morphology of electrochemically prepared polyaniline. Influence of polymerization parameters. *Journal of Materials Chemistry, 3*(3), 263-272.

Diaz, A. F., & Logan, J. A. (1980). Electroactive polyaniline films. *Journal of Electroanalytical Chemistry and Interfacial Electrochemistry, 111*(1), 111-114.

Dietz, R. E., Parisot, G. I., & Meixner, A. E. (1971). Infrared absorption and raman scattering by two-magnon processes in NiO. *Physical Review B, 4*(7), 2302-2310.

Ding, L., Li, Q., Zhou, D., Cui, H., An, H., & Zhai, J. (2012). Modification of glassy carbon electrode with polyaniline/multi-walled carbon nanotubes composite: Application to electro-reduction of bromate. *Journal of Electroanalytical Chemistry, 668*, 44-50.

Dong, X., Wang, K., Zhao, C., Qian, X., Chen, S., Li, Z., . . . Dou, S. (2014). Direct synthesis of RGO/Cu_2O composite films on Cu foil for supercapacitors. *Journal of Alloys and Compounds, 586*, 745-753.

Du, H., Liu, X., Ren, Z., Yang, H., & Yu, Y. (2018). Capacitance properties of unipolar pulsed electro-polymerized PEDOT films. *Journal of Applied Polymer Science, 135*(40), Article#46729.

Duan, Y., Hu, T., Yang, L., Gao, J., Guo, S., Hou, M., & Ye, X. (2019). Facile fabrication of electroactive microporous Co_3O_4 through microwave plasma etching for supercapacitors. *Journal of Alloys and Compounds, 771*, 156-161.

Dubal, D. P., Chodankar, N. R., Gund, G. S., Holze, R., Lokhande, C. D., & Gomez-Romero, P. (2015). Asymmetric supercapacitors based on hybrid CuO@reduced graphene oxide@sponge versus reduced graphene oxide@sponge electrodes. *Energy Technology, 3*(2), 168-176.

Dubal, D. P., Fulari, V. J., & Lokhande, C. D. (2012). Effect of morphology on supercapacitive properties of chemically grown β-$Ni(OH)_2$ thin films. *Microporous and Mesoporous Materials, 151*, 511-516.

Dubal, D. P., Gund, G. S., Lokhande, C. D., & Holze, R. (2013). Decoration of spongelike $Ni(OH)_2$ nanoparticles onto mwcnts using an easily manipulated chemical protocol for supercapacitors. *ACS Applied Materials & Interfaces, 5*(7), 2446-2454.

Dubal, D. P., Kim, J. G., Kim, Y., Holze, R., Lokhande, C. D., & Kim, W. B. (2014). Supercapacitors based on flexible substrates: An overview. *Energy Technology, 2*(4), 325-341.

Dziewoński, P. M., & Grzeszczuk, M. (2010). Towards TiO_2-conducting polymer hybrid materials for lithium ion batteries. *Electrochimica Acta, 55*(9), 3336-3347.

Ebrahim, S. A., Harb, M. E., Soliman, M. M., & Tayel, M. B. (2016). Preparation and characterization of a pseudocapacitor electrode by spraying a conducting polymer onto a flexible substrate. *Journal of Taibah University for Science, 10*(2), 281-285.

Eftekhari, A., Li, L., & Yang, Y. (2017). Polyaniline supercapacitors. *Journal of Power Sources, 347*, 86-107.

Gan, X., Zhao, H., Chen, S., Yu, H., & Quan, X. (2015). Three-Dimensional Porous H_xTiS_2 nanosheet–polyaniline nanocomposite electrodes for directly detecting trace Cu(II) ions. *Analytical Chemistry, 87*(11), 5605-5613.

García-Gallegos, J. C., Vega-Cantú, Y. I., & Rodríguez-Macías, F. J. (2018). Fast mechanochemical synthesis of carbon nanotube-polyaniline hybrid materials. *Journal of Materials Research, 33*(10), 1486-1495.

Ge, X., Gu, C. D., Lu, Y., Wang, X. L., & Tu, J. P. (2013). A versatile protocol for the ionothermal synthesis of nanostructured nickel compounds as energy storage materials from a choline chloride-based ionic liquid. *Journal of Materials Chemistry A, 1*(43), 13454-13461.

Gilchrist, L. (1903). The electrolysis of acid solutions of aniline. *The Journal of Physical Chemistry, 8*(8), 539-547.

Girija, T. C., & Sangaranarayanan, M. V. (2006). Analysis of polyaniline-based nickel electrodes for electrochemical supercapacitors. *Journal of Power Sources, 156*(2), 705-711.

Gongkai, W., Xiang, S., Fengyuan, L., Hongtao, S., Mingpeng, Y., Weilin, J., . . . Jie, L. (2012). Flexible pillared graphene‐paper electrodes for high‐performance electrochemical supercapacitors. *Small, 8*(3), 452-459.

González, A., Goikolea, E., Barrena, J. A., & Mysyk, R. (2016). Review on supercapacitors: Technologies and materials. *Renewable and Sustainable Energy Reviews, 58*, 1189-1206.

Green, A. G., & Woodhead, A. E. (1910). CCXLIII.-Aniline-black and allied compounds. Part I. *Journal of the Chemical Society, Transactions, 97*(0), 2388-2403.

Guo, F., Ye, K., Huang, X., Gao, Y., Cheng, K., Wang, G., & Cao, D. (2015). Palladium dispersed in three-dimensional polyaniline networks as the catalyst for hydrogen peroxide electro-reduction in an acidic medium. *RSC Advances, 5*(114), 94008-94015.

Han, G., Liu, Y., Zhang, L., Kan, E., Zhang, S., Tang, J., & Tang, W. (2014). MnO_2 nanorods intercalating graphene oxide/polyaniline ternary composites for robust high-performance supercapacitors. *Scientific Reports, 4*, Article#4824.

He, S., Hu, X., Chen, S., Hu, H., Hanif, M., & Hou, H. (2012). Needle-like polyaniline nanowires on graphite nanofibers: hierarchical micro/nano-architecture for high performance supercapacitors. *Journal of Materials Chemistry, 22*(11), 5114-5120.

Hong, X., Li, S., Wang, R., & Fu, J. (2019). Hierarchical SnO_2 nanoclusters wrapped functionalized carbonized cotton cloth for symmetrical supercapacitor. *Journal of Alloys and Compounds, 775*, 15-21.

Horng, Y.-Y., Lu, Y.-C., Hsu, Y.-K., Chen, C.-C., Chen, L.-C., & Chen, K.-H. (2010). Flexible supercapacitor based on polyaniline nanowires/carbon cloth with both high gravimetric and area-normalized capacitance. *Journal of Power Sources, 195*(13), 4418-4422.

Hu, Z., Tong, G., Lin, D., Nian, Q., Shao, J., Hu, Y., . . . Cheng, G. J. (2016). Laser sintered graphene nickel nanocomposites. *Journal of Materials Processing Technology, 231*, 143-150.

Huang, B., Wang, W., Pu, T., Li, J., Zhu, J., Zhao, C., . . . Chen, L. (2018). Two-dimensional porous (Co, Ni)-based monometallic hydroxides and bimetallic layered double hydroxides thin sheets with honeycomb-like nanostructure as positive electrode for high-performance hybrid supercapacitors. *Journal of Colloid and Interface Science, 532*, 630-640.

Indrajit, S., Abhijit, G., Li‐Chyong, C., & Kuei‐Hsien, C. (2015). Conducting polymer‐based flexible supercapacitor. *Energy Science & Engineering, 3*(1), 2-Article#26.

Islam, N., Wang, S., Warzywoda, J., & Fan, Z. (2018). Fast supercapacitors based on vertically oriented MoS_2 nanosheets on plasma pyrolyzed cellulose filter paper. *Journal of Power Sources, 400*, 277-283.

Jafari, S., Dehghani, M., Nasirizadeh, N., & Azimzadeh, M. (2018). An azithromycin electrochemical sensor based on an aniline MIP film electropolymerized on a gold nano urchins/graphene oxide modified glassy carbon electrode. *Journal of Electroanalytical Chemistry, 829*, 27-34.

Jagadale, A. D., Jamadade, V. S., Pusawale, S. N., & Lokhande, C. D. (2012). Effect of scan rate on the morphology of potentiodynamically deposited β-$Co(OH)_2$ and corresponding supercapacitive performance. *Electrochimica Acta, 78*, 92-97.

Jeong, H. T., Du, J. F., Kim, Y. R., Raj, C. J., & Kim, B. C. (2019). Electrochemical performances of highly stretchable polyurethane (PU) supercapacitors based on nanocarbon materials composites. *Journal of Alloys and Compounds, 777*, 67-72.

Jiang, Y., Yan, J., Wu, X., Shan, D., Zhou, Q., Jiang, L., . . . Fan, Z. (2016). Facile synthesis of carbon nanofibers-bridged porous carbon nanosheets for high-performance supercapacitors. *Journal of Power Sources, 307*, 190-198.

Jingbin, H., Yibo, D., Jingwen, Z., Min, W., G., E. D., & Xue, D. (2013). Flexible CoAl LDH@PEDOT core/shell nanoplatelet array for high‐performance energy storage. *Small, 9*(1), 98-106.

Kai, W., Haiping, W., Yuena, M., & Zhixiang, W. (2014). Conducting polymer nanowire arrays for high performance supercapacitors. *Small, 10*(1), 14-31.

Kamchi, N. E., Belaabed, B., Wojkiewicz, J. L., Lamouri, S., & Lasri, T. (2013). Hybrid polyaniline/nanomagnetic particles composites: High performance materials for EMI shielding. *Journal of Applied Polymer Science, 127*(6), 4426-4432.

Kandasamy, S. K., & Kandasamy, K. (2018). Recent advances in electrochemical performances of graphene composite (graphene-polyaniline/polypyrrole/activated carbon/carbon nanotube) electrode materials for supercapacitor: A Review. *Journal of Inorganic and Organometallic Polymers and Materials, 28*(3), 559-584.

Kannan, V., Choi, J. H., Park, H. C., & Kim, H. S. (2018). Ultrahigh supercapacitance in cobalt oxide nanorod film grown by oblique angle deposition technique. *Current Applied Physics, 18*(11), 1399-1402.

Kar, P., & Choudhury, A. (2013). Carboxylic acid functionalized multi-walled carbon nanotube doped polyaniline for chloroform sensors. *Sensors and Actuators B: Chemical, 183*, 25-33.

Khairy, M., & El-Safty, S. A. (2013). Mesoporous NiO nanoarchitectures for electrochemical energy storage: influence of size, porosity, and morphology. *RSC Advances, 3*(45), 23801-23809.

Kim, D. H., Richardson‐Burns, S. M., Hendricks, J. L., Sequera, C., & Martin, D. C. (2007). Effect of immobilized nerve growth factor on conductive polymers: Electrical properties and cellular response. *Advanced Functional Materials, 17*(1), 79-86.

Kiseleva, E. A., Kochanova, S. A., Uryupina, O. V., Puntusova, L., & Tarasenko, A. B. (2018). *Carbon additive structure influence on electrochemical double-layer capacitor electrode behavior.* Paper presented at the IOP Conference Series: Earth and Environmental Science.

Kudin, K. N., Ozbas, B., Schniepp, H. C., Prud'homme, R. K., Aksay, I. A., & Car, R. (2008). Raman spectra of graphite oxide and functionalized graphene sheets. *Nano Letters, 8*(1), 36-41.

Kumar, K. Y., Archana, S., Namitha, R., Prasanna, B. P., Sharma, S. C., & Raghu, M. S. (2018). Ruthenium oxide nanostring clusters anchored graphene oxide nanocomposites for high-performance supercapacitors application. *Materials Research Bulletin, 107*, 347-354.

Lai, C.-C., & Lo, C.-T. (2015). Preparation of nanostructural carbon nanofibers and their electrochemical performance for supercapacitors. *Electrochimica Acta, 183*, 85-93.

Laleh, G. M., P, P. M., Mohammad, M., Hossein, N. E. M., Hossein, B., Sahar, K., . . . Seeram, R. (2011). Application of conductive polymers, scaffolds and electrical stimulation for nerve tissue engineering. *Journal of Tissue Engineering and Regenerative Medicine, 5*(4), e17-e35.

Latorre-Sanchez, A., & Pomposo, J. A. (2015). A simple, fast and highly sensitive colorimetric detection of zein in aqueous ethanol via zein-pyridine-gold interactions. *Chemical Communications, 51*(86), 15736-15738.

Leif, N., Gustav, N., Albert, M., & Maria, S. (2011). Toward flexible polymer and paper‐based energy storage devices. *Advanced Materials, 23*(33), 3751-3769.

Leng, Y. (2008). Scanning Electron Microscopy *Materials Characterization* (pp. 121-144), John Wiley & Sons (Asia) Pte Ltd.

Li, B., Yao, F., Bae, J. J., Chang, J., Zamfir, M. R., Le, D. T., . . . Lee, Y. H. (2015). Hollow carbon nanospheres/silicon/alumina core-shell film as an anode for lithium-ion batteries. *Scientific Reports, 5*, Article#7659.

Li, J., Luan, C., Cui, Y., Zhang, H., Wang, L., Wang, H., . . . Cheng, X. (2019). Preparation and characterization of palladium/polyaniline/foamed nickel composite electrode for electrocatalytic dechlorination. *Separation and Purification Technology, 211*, 198-206.

Li, J., Zhu, M., An, Z., Wang, Z., Toda, M., & Ono, T. (2018). Constructing in-chip micro-supercapacitors of 3D graphene nanowall/ruthenium oxides electrode through silicon-based microfabrication technique. *Journal of Power Sources, 401*, 204-212.

Li, X., Liu, Y., Guo, W., Chen, J., He, W., & Peng, F. (2014). Synthesis of spherical PANI particles via chemical polymerization in ionic liquid for high-performance supercapacitors. *Electrochimica Acta, 135*, 550-557.

Li, X., Pletcher, D., & Walsh, F. C. (2009). A novel flow battery: A lead acid battery based on an electrolyte with soluble lead(II): Part VII. Further studies of the lead dioxide positive electrode. *Electrochimica Acta, 54*(20), 4688-4695.

Liu, J., Rehman, S. U., Wang, J., Fang, Z., Zhang, X., & Bi, H. (2018). Magnetic-field assisted synthesis of carbon dots-doped polyaniline nanotubes with a high-performance supercapacitance. *Synthetic Metals, 246*, 23-30.

Liu, S., Zeng, W., & Chen, T. (2017a). Synthesis of hierarchical flower-like NiO and the influence of surfactant. *Physica E: Low-dimensional Systems and Nanostructures, 85*, 13-18.

Liu, Y., Ma, Y., Guang, S., Xu, H., & Su, X. (2014). Facile fabrication of three-dimensional highly ordered structural polyaniline-graphene bulk hybrid materials for high performance supercapacitor electrodes. *Journal of Materials Chemistry A, 2*(3), 813-823.

Liu, Y., Zhou, X., Liu, R., Li, X., Bai, Y., & Yuan, G. (2017b). Preparation of three-dimensional compressible MnO2@carbon nanotube sponges with enhanced supercapacitor performance. *New Journal of Chemistry, 41*(24), 14906-14913.

Lv, D., Shen, J., & Wang, G. (2015). A post-oxidation strategy for the synthesis of graphene/carbon nanotube-supported polyaniline nanocomposites as advanced supercapacitor electrodes. *RSC Advances, 5*(31), 24599-24606.

Ma, J., Tang, S., Syed, J. A., & Meng, X. (2016). Asymmetric hybrid capacitors based on novel bearded carbon fiber cloth-pinhole polyaniline electrodes with excellent energy density. *RSC Advances, 6*(86), 82995-83002.

Ma, X., & Kang, Z. (2019). A facile electrodeposition technique for synthesis of nickel sulfides/carbon nanotubes nanocomposites as high performance electrodes for supercapacitor. *Materials Letters, 236*, 468-471.

MacDiarmid, A. G., & Epstein, A. J. (1989). Polyanilines: a novel class of conducting polymers. *Faraday Discussions of the Chemical Society, 88*(0), 317-332.

Manoj, M., Muhamed Ashraf, C., Jasna, M., Anilkumar, K. M., Jinisha, B., Pradeep, V. S., & Jayalekshmi, S. (2019). Biomass-derived, activated carbon-sulfur composite cathode with a bifunctional interlayer of functionalized carbon nanotubes for lithium-sulfur cells. *Journal of Colloid and Interface Science, 535*, 287-299.

Marotti, R. E., Giorgi, P., Machado, G., & Dalchiele, E. A. (2006). Crystallite size dependence of band gap energy for electrodeposited ZnO grown at different temperatures. *Solar Energy Materials and Solar Cells, 90*(15), 2356-2361.

Meher, S. K., Justin, P., & Ranga Rao, G. (2011). Nanoscale morphology dependent pseudocapacitance of NiO: Influence of intercalating anions during synthesis. *Nanoscale, 3*(2), 683-692.

Mello, H. J. N. P. D., & Mulato, M. (2018). Effect of aniline monomer concentration on PANI electropolymerization process and its influence for applications in chemical sensors. *Synthetic Metals, 239*, 66-70.

Meng, C., Liu, C., Chen, L., Hu, C., & Fan, S. (2010). Highly flexible and all-solid-state paperlike polymer supercapacitors. *Nano Letters, 10*(10), 4025-4031.

Miao, R., & Zeng, W. (2016). Hydrothermal synthesis of flake-flower NiO architectures: Structure, growth and gas-sensing properties. *Materials Letters, 171*, 200-203.

Miao, Y.-E., Fan, W., Chen, D., & Liu, T. (2013). High-performance supercapacitors based on hollow polyaniline nanofibers by electrospinning. *ACS Applied Materials & Interfaces, 5*(10), 4423-4428.

Miller, E. E., Hua, Y., & Tezel, F. H. (2018). Materials for energy storage: Review of electrode materials and methods of increasing capacitance for supercapacitors. *Journal of Energy Storage, 20*, 30-40.

Miller, J. R., & Simon, P. (2008). Electrochemical capacitors for energy management. *Science, 321*(5889), 651-652.

Minakshi, M., Mitchell, D., Jones, R., Alenazey, F., Watcharatharapong, T., Chakraborty, S., & Ahuja, R. (2016). Synthesis, structural and electrochemical properties of sodium nickel phosphate for energy storage devices. *Nanoscale, 8*(21), 11291-11305.

Mironova-Ulmane, N., Kuzmin, A., Sildos, I., & Pärs, M. (2011). Polarisation dependent Raman study of single-crystal nickel oxide *Open Physics* 9(4), 1096-1099.

Moyseowicz, A., & Gryglewicz, G. (2019). Hydrothermal-assisted synthesis of a porous polyaniline/reduced graphene oxide composite as a high-performance electrode material for supercapacitors. *Composites Part B: Engineering, 159*, 4-12.

Mu, H., Bai, J., Li, C., & Sun, W. (2019). Strong physisorption and superb thermal stability of carbon nanofibers carried Cu_xO-V_2O_5 enabling the flexible and long-cycling supercapacitor. *Journal of Alloys and Compounds, 775*, 872-882.

Mu, J., Ma, G., Peng, H., Li, J., Sun, K., & Lei, Z. (2013). Facile fabrication of self-assembled polyaniline nanotubes doped with d-tartaric acid for high-performance supercapacitors. *Journal of Power Sources, 242*, 797-802.

Naoi, K., Kisu, K., Iwama, E., Nakashima, S., Sakai, Y., Orikasa, Y., . . . Simon, P. (2016). Ultrafast charge-discharge characteristics of a nanosized core-shell structured $LiFePO_4$ material for hybrid supercapacitor applications. *Energy & Environmental Science, 9*(6), 2143-2151.

Neelgund, G. M., & Oki, A. (2011). A facile method for synthesis of polyaniline nanospheres and effect of doping on their electrical conductivity. *Polymer international, 60*(9), 1291-1295.

Nie, S., Liu, L., Liu, J., Xia, J., Zhang, Y., Xie, J., . . . Wang, X. (2019). TiO_2-Sn/C composite nanofibers with high-capacity and long-cycle life as anode materials for sodium ion batteries. *Journal of Alloys and Compounds, 772*, 314-323.

Nwanya, A. C., Offiah, S. U., Amaechi, I. C., Agbo, S., Ezugwu, S. C., Sone, B. T., . . . Ezema, F. I. (2015). Electrochromic and electrochemical supercapacitive properties of Room Temperature PVP capped $Ni(OH)_2$/NiO Thin Films. *Electrochimica Acta, 171*, 128-141.

Ouyang, J. (2018). Recent advances of intrinsically conductive polymers. *Wuli Huaxue Xuebao/ Acta Physico - Chimica Sinica, 34*(11), 1211-1220.

Pan, A., Zhang, J.-G., Nie, Z., Cao, G., Arey, B. W., Li, G., . . . Liu, J. (2010). Facile synthesized nanorod structured vanadium pentoxide for high-rate lithium batteries. *Journal of Materials Chemistry, 20*(41), 9193-9199.

Pandey, J. K., Raghunatha Reddy, K., Pratheep Kumar, A., & Singh, R. P. (2005). An overview on the degradability of polymer nanocomposites. *Polymer Degradation and Stability, 88*(2), 234-250.

Pandit, B., Dubal, D. P., & Sankapal, B. R. (2017). Large scale flexible solid state symmetric supercapacitor through inexpensive solution processed V_2O_5 complex surface architecture. *Electrochimica Acta, 242*, 382-389.

Pandolfo, A. G., & Hollenkamp, A. F. (2006). Carbon properties and their role in supercapacitors. *Journal of Power Sources, 157*(1), 11-27.

Park, S., & Popov, B. N. (2011). Effect of a GDL based on carbon paper or carbon cloth on PEM fuel cell performance. *Fuel, 90*(1), 436-440.

Peng, H., Zhang, L., Soeller, C., & Travas-Sejdic, J. (2009). Conducting polymers for electrochemical DNA sensing. *Biomaterials, 30*(11), 2132-2148.

Pilban Jahromi, S., Pandikumar, A., Goh, B. T., Lim, Y. S., Basirun, W. J., Lim, H. N., & Huang, N. M. (2015). Influence of particle size on performance of a nickel oxide nanoparticle-based supercapacitor. *RSC Advances, 5*(18), 14010-14019.

Prataap, R. K. V., Arunachalam, R., Pavul Raj, R., Mohan, S., & Peter, L. (2018). Effect of electrodeposition modes on ruthenium oxide electrodes for supercapacitors. *Current Applied Physics, 18*(10), 1143-1148.

Qu, X., Huang, G., Xing, B., Si, D., Xu, B., Chen, Z., . . . Cao, Y. (2019). Core-shell carbon composite material as anode materials for lithium-ion batteries. *Journal of Alloys and Compounds, 772*, 814-822.

Ramesh, P., & Jebasingh, B. (2019). A facile synthesis of bis-(ptththalimidoethyl)-amine functionalized graphene oxide and its dual performance as a supercapacitor electrode and fluorescence sensor. *Materials Chemistry and Physics, 222*, 45-54.

Ramya, R., Sivasubramanian, R., & Sangaranarayanan, M. V. (2013). Conducting polymers-based electrochemical supercapacitors—Progress and prospects. *Electrochimica Acta, 101*, 109-129.

Randles, J. E. B. (1948). A cathode ray polarograph. Part II.—The current-voltage curves. *Transactions of the Faraday Society, 44*(0), 327-338.

Ravichandran, R., Sundarrajan, S., Venugopal, J. R., Mukherjee, S., & Ramakrishna, S. (2010). Applications of conducting polymers and their issues in biomedical engineering. *Journal of The Royal Society Interface, 7*(Suppl 5), Article#S559.

Razali, S. A., & Majid, S. R. (2018). Electrochemical performance of binder-free NiO-PANI on etched carbon cloth as active electrode material for supercapacitor. *Materials & Design, 153*, 24-35.

Razali, S. A., Rusi, & Majid, S. R. (2018). Fabrication of polyaniline nanorods on electro-etched carbon cloth and its electrochemical activities as electrode materials. *Ionics, 25*(6), 2575-2584.

Roy, A., Ray, A., Sadhukhan, P., Saha, S., & Das, S. (2018). Morphological behaviour, electronic bond formation and electrochemical performance study of V_2O_5-polyaniline composite and its application in asymmetric supercapacitor. *Materials Research Bulletin, 107*, 379-390.

Rusi, & Majid, S. R. (2013). Synthesis of MnO_2 particles under slow cooling process and their capacitive performances. *Materials Letters, 108*, 69-71.

Ryu, K. S., Kim, K. M., Park, N.-G., Park, Y. J., & Chang, S. H. (2002). Symmetric redox supercapacitor with conducting polyaniline electrodes. *Journal of Power Sources, 103*(2), 305-309.

Sahu, D. R., Wu, T.-J., Wang, S.-C., & Huang, J.-L. (2017). Electrochromic behavior of NiO film prepared by e-beam evaporation. *Journal of Science: Advanced Materials and Devices, 2*(2), 225-232.

Salanne, M., Rotenberg, B., Naoi, K., Kaneko, K., Taberna, P. L., Grey, C. P., . . . Simon, P. (2016). Efficient storage mechanisms for building better supercapacitors. *Nature Energy, 1*, Article#16070.

Sanliang, Z., & Ning, P. (2015). Supercapacitors Performance Evaluation. *Advanced Energy Materials, 5*(6), Article#1401401.

Saranya, K., Rameez, M., & Subramania, A. (2015). Developments in conducting polymer based counter electrodes for dye-sensitized solar cells – An overview. *European Polymer Journal, 66*, 207-227.

Sawangphruk, M., Srimuk, P., Chiochan, P., Krittayavathananon, A., Luanwuthi, S., & Limtrakul, J. (2013). High-performance supercapacitor of manganese oxide/reduced graphene oxide nanocomposite coated on flexible carbon fiber paper. *Carbon, 60*, 109-116.

Sayah, A., Habelhames, F., Bahloul, A., Nessark, B., Bonnassieux, Y., Tendelier, D., & El Jouad, M. (2018). Electrochemical synthesis of polyaniline-exfoliated graphene composite films and their capacitance properties. *Journal of Electroanalytical Chemistry, 818*, 26-34.

Sharma, P., & Bhatti, T. S. (2010). A review on electrochemical double-layer capacitors. *Energy Conversion and Management, 51*(12), 2901-2912.

Shen, L., & Huang, X. (2018). Electrochemical polymerization of aniline in a protic ionic liquid with high proton activity. *Synthetic Metals, 245*, 18-23.

Shi, F., Li, L., Wang, X.-l., Gu, C.-d., & Tu, J.-p. (2014). Metal oxide/hydroxide-based materials for supercapacitors. *RSC Advances, 4*(79), 41910-41921.

Shirakawa, H., Louis, E. J., MacDiarmid, A. G., Chiang, C. K., & Heeger, A. J. (1977). Synthesis of electrically conducting organic polymers: halogen derivatives of polyacetylene, (CH). *Journal of the Chemical Society, Chemical Communications*, *16*, 578-580.

Shklovsky, J., Reuveny, A., Sverdlov, Y., Krylov, S., & Shacham-Diamand, Y. (2018). Towards fully polymeric electroactive micro actuators with conductive polymer electrodes. *Microelectronic Engineering, 199*, 58-62.

Simotwo, S. K., Delre, C., & Kalra, V. (2016). Supercapacitor electrodes based on high-purity electrospun polyaniline and polyaniline-carbon nanotube nanofibers. *ACS Applied Materials and Interfaces, 8*(33), 21261-21269.

Simotwo, S. K., & Kalra, V. (2016). Polyaniline-based electrodes: recent application in supercapacitors and next generation rechargeable batteries. *Current Opinion in Chemical Engineering, 13*, 150-160.

Snook, G. A., Kao, P., & Best, A. S. (2011). Conducting-polymer-based supercapacitor devices and electrodes. *Journal of Power Sources, 196*(1), 1-12.

Song, H., Zhang, C., Li, T., He, X., Han, Y., Wang, Y., & Wang, Q. (2017). Synthesis and characterization of conductive polyaniline nanocomposite containing fluorene. *High Performance Polymers, 29*(10), 1192-1198.

Su, X., Gao, L., Zhou, F., & Duan, G. (2017). A substrate-independent fabrication of hollow sphere arrays via template-assisted hydrothermal approach and their application in gas sensing. *Sensors and Actuators, B: Chemical, 251*, 74-85.

Sun, W., Xiao, L., & Wu, X. (2019). Facile synthesis of NiO nanocubes for photocatalysts and supercapacitor electrodes. *Journal of Alloys and Compounds, 772*, 465-471.

Tabrizi, A. G., Arsalani, N., Mohammadi, A., Ghadimi, L. S., & Ahadzadeh, I. (2018). High-performance asymmetric supercapacitor based on hierarchical nanocomposites of polyaniline nanoarrays on graphene oxide and its derived N-doped carbon nanoarrays grown on graphene sheets. *Journal of Colloid and Interface Science, 531*, 369-381.

Tao, S., Hong, B., & Kerong, Z. (2007). An infrared and Raman spectroscopic study of polyanilines co-doped with metal ions and H+. *Spectrochimica acta. Part A, Molecular and biomolecular spectroscopy, 66*(4-5), 1364-1368.

Thaneswari, S. A. (2018). Direct growth of multi-walled carbon nanotubes on ni foil by chemical vapor deposition method for supercapacitor applications. *Journal of Advanced Microscopy Research, 13*(2), 223-229.

Tran, C., Singhal, R., Lawrence, D., & Kalra, V. (2015). Polyaniline-coated freestanding porous carbon nanofibers as efficient hybrid electrodes for supercapacitors. *Journal of Power Sources, 293*, 373-379.

Trchová, M., Šeděnková, I., Konyushenko, E. N., Stejskal, J., Holler, P., & Ćirić-Marjanović, G. (2006). Evolution of polyaniline nanotubes: The oxidation of aniline in water. *The Journal of Physical Chemistry B, 110*(19), 9461-9468.

Umeshbabu, E., Rajeshkhanna, G., Justin, P., & Rao, G. R. (2015a). Synthesis of mesoporous $NiCo_2O_4$-rGO by a solvothermal method for charge storage applications. *RSC Advances, 5*(82), 66657-66666.

Vellacheri, R., Zhao, H., Mühlstädt, M., Al-Haddad, A., Jandt, K. D., & Lei, Y. (2017). Rationally engineered electrodes for a high-performance solid-state cable-type supercapacitor. *Advanced Functional Materials, 27*(18), Article#1606696.

Vello, T. P., de Oliveira, R. F., Silva, G. O., de Camargo, D. H. S., & Bufon, C. C. B. (2017). A simple capacitive method to evaluate ethanol fuel samples. *Scientific Reports, 7*, 43432.

Venancio, E. C., Wang, P.-C., & MacDiarmid, A. G. (2006). The azanes: A class of material incorporating nano/micro self-assembled hollow spheres obtained by aqueous oxidative polymerization of aniline. *Synthetic Metals, 156*(5), 357-369.

Wallace, G., & Spinks, G. (2007). Conducting polymers - bridging the bionic interface. *Soft Matter, 3*(6), 665-671.

Wang, G., Zhang, L., & Zhang, J. (2012). A review of electrode materials for electrochemical supercapacitors. *Chemical Society Reviews, 41*(2), 797-828.

Wang, H., Lin, J., & Shen, Z. X. (2016). Polyaniline (PANi) based electrode materials for energy storage and conversion. *Journal of Science: Advanced Materials and Devices, 1*(3), 225-255.

Wang, H. T., Liu, Y. N., Kang, X. H., Wang, Y. F., Yang, S. Y., Bian, S. W., & Zhu, Q. (2018). Flexible hybrid yarn-shaped supercapacitors based on porous nickel cobalt sulfide nanosheet array layers on gold metalized cotton yarns. *Journal of Colloid and Interface Science, 532*, 527-535.

Wang, L., Yang, H., Pan, G., Miao, L., Chen, S., & Song, Y. (2017). Polyaniline-carbon nanotubes@zeolite imidazolate framework-67-carbon cloth hierarchical nanostructures for supercapacitor Electrode. *Electrochimica Acta, 240*, 16-23.

Wang, N., Song, H., Ren, H., Chen, J., Yao, M., Huang, W., . . . Komarneni, S. (2019a). Partly nitrogenized nickel oxide hollow spheres with multiple compositions for remarkable electrochemical performance. *Chemical Engineering Journal, 358*, 531-539.

Wang, W., Bai, J., Wang, J., & Li, C. (2019b). Self-assembly 3D needle-like nickel nanostructure growth on carbon fibers by regulating prepare conditions and exploited as bifunctional material. *Applied Surface Science, 465*, 82-92.

Wang, X., Deng, J., Duan, X., Liu, D., Guo, J., & Liu, P. (2014). Crosslinked polyaniline nanorods with improved electrochemical performance as electrode material for supercapacitors. *Journal of Materials Chemistry A, 2*(31), 12323-12329.

Wei, M., Li, B., Zang, X., Chen, W., Chu, Y., Sanghadasa, M., & Lin, L. (2017). *Flexible Harsh environment micro supercapacitors using direct-write 2D transition metal carbides.* Paper presented at the TRANSDUCERS 2017 - 19th International Conference on Solid-State Sensors, Actuators and Microsystems.

Wei, W., Cui, X., Chen, W., & Ivey, D. G. (2011). Manganese oxide-based materials as electrochemical supercapacitor electrodes. *Chemical Society Reviews, 40*(3), 1697-1721.

Wong, J. Y., Langer, R., & Ingber, D. E. (1994). Electrically conducting polymers can noninvasively control the shape and growth of mammalian cells. *Proceedings of the National Academy of Sciences, 91*(8), Article#3201.

Wu, M.-S., Huang, Y.-A., Jow, J.-J., Yang, W.-D., Hsieh, C.-Y., & Tsai, H.-M. (2008). Anodically potentiostatic deposition of flaky nickel oxide nanostructures and their electrochemical performances. *International Journal of Hydrogen Energy, 33*(12), 2921-2926.

Xia, X.-h., Tu, J.-p., Wang, X.-l., Gu, C.-d., & Zhao, X.-b. (2011). Hierarchically porous NiO film grown by chemical bath deposition via a colloidal crystal template as an

electrochemical pseudocapacitor material. *Journal of Materials Chemistry, 21*(3), 671-679.

Xia, Y., MacDiarmid, A. G., & Epstein, A. J. (1994). Camphorsulfonic acid fully doped polyaniline emeraldine salt: In situ observation of electronic and conformational changes induced by organic vapors by an ultraviolet/visible/near-infrared spectroscopic method. *Macromolecules, 27*(24), 7212-7214.

Xiao, H., Yao, S., Liu, H., Qu, F., Zhang, X., & Wu, X. (2016). NiO nanosheet assembles for supercapacitor electrode materials. *Progress in Natural Science: Materials International, 26*(3), 271-275.

Xiao, L., Kerry, J. G., Simon, E. M., & Gordon, G. W. (2009). Electrical stimulation promotes nerve cell differentiation on polypyrrole/poly (2-methoxy-5 aniline sulfonic acid) composites. *Journal of Neural Engineering, 6*(6), Article#065002.

Xin, L., M., E. A., Cao, G., & John, W. (2017). Metal phosphides and phosphates‐based electrodes for electrochemical supercapacitors. *Small, 13*(39), Article#1701530.

Xing, W., Li, F., Yan, Z.-f., & Lu, G. Q. (2004). Synthesis and electrochemical properties of mesoporous nickel oxide. *Journal of Power Sources, 134*(2), 324-330.

Xiong, R., Chen, H., Wang, C., & Sun, F. (2018). Towards a smarter hybrid energy storage system based on battery and ultracapacitor - A critical review on topology and energy management. *Journal of Cleaner Production, 202*, 1228-1240.

Xu, C., Xu, B., Gu, Y., Xiong, Z., Sun, J., & Zhao, X. S. (2013). Graphene-based electrodes for electrochemical energy storage. *Energy & Environmental Science, 6*(5), 1388-1414.

Xu, H., Zhang, J., Chen, Y., Lu, H., & Zhuang, J. (2014). Electrochemical polymerization of polyaniline doped with Cu^{2+} as the electrode material for electrochemical supercapacitors. *RSC Advances, 4*(11), 5547-5552.

Xu, X., Tian, X., Li, X., Yang, T., He, Y., Wang, K., . . . Liu, Z. (2019a). Structural and chemical synergistic effect of $NiCo_2S_4$ nanoparticles and carbon cloth for high performance binder-free asymmetric supercapacitors. *Applied Surface Science, 465*, 635-642.

Xu, Z., Chen, J., Zhang, X., Song, Q., Wu, J., Ding, L., . . . Cui, H. (2019b). Template-free preparation of nitrogen-doped activated carbon with porous architecture for high-performance supercapacitors. *Microporous and Mesoporous Materials, 276*, 280-291.

Xue, M., Li, F., Zhu, J., Song, H., Zhang, M., & Cao, T. (2012). Structure-based enhanced capacitance: In situ growth of highly ordered polyaniline nanorods on reduced graphene oxide patterns. *Advanced Functional Materials, 22*(6), 1284-1290.

Yang, S., Yu, J., Jiang, T., Zhu, L., & Xu, X. (2018). High performance symmetric solid state supercapacitor based on electrode of Ru_xNi_1-xCo_2O_4 grown on nickel foam. *Journal of Alloys and Compounds, 764*, 767-775.

Yoo, Y. E., Park, J., & Kim, W. (2018). Understanding and controlling the rest potential of carbon nanotube-based supercapacitors for energy density enhancement. *Applied Surface Science, 433*, 765-771.

Yu, T., Zhu, P., Xiong, Y., Chen, H., Kang, S., Luo, H., & Guan, S. (2016). Synthesis of microspherical polyaniline/graphene composites and their application in supercapacitors. *Electrochimica Acta, 222*, 12-19.

Zhang, J., Jiang, J., Li, H., & Zhao, X. S. (2011). A high-performance asymmetric supercapacitor fabricated with graphene-based electrodes. *Energy & Environmental Science, 4*(10), 4009-4015.

Zhang, L., Zhao, G., & Wang, Y. (2013a). Polyaniline nanowire electrodes with high capacitance synthesized by a simple approach. *Materials Science and Engineering: C, 33*(1), 209-212.

Zhang, L., Zhao, G., & Wang, Y. (2013b). Polyaniline nanowire electrodes with high capacitance synthesized by a simple approach. *Materials science & engineering. C, Materials for biological applications, 33*(1), 209-212.

Zhang, L. L., & Zhao, X. S. (2009). Carbon-based materials as supercapacitor electrodes. *Chemical Society Reviews, 38*(9), 2520-2531.

Zhang, M., Song, X., Ou, X., & Tang, Y. (2019). Rechargeable batteries based on anion intercalation graphite cathodes. *Energy Storage Materials, 16*, 65-84.

Zhang, S., Brahim, S., & Maat, S. (2018a). High-voltage operation of binder-free CNT supercapacitors using ionic liquid electrolytes. *Journal of Materials Research, 33*(9), 1179-1188.

Zhang, W., Xu, J., Hou, D., Yin, J., Liu, D., He, Y., & Lin, H. (2018b). Hierarchical porous carbon prepared from biomass through a facile method for supercapacitor applications. *Journal of Colloid and Interface Science, 530*, 338-344.

Zhang, Y., Feng, H., Wu, X., Wang, L., Zhang, A., Xia, T., . . . Zhang, L. (2009). Progress of electrochemical capacitor electrode materials: A review. *International Journal of Hydrogen Energy, 34*(11), 4889-4899.

Zhang, Y., Ji, T., Hou, S., Zhang, L., Shi, Y., Zhao, J., & Xu, X. (2018c). All-printed solid-state substrate-versatile and high-performance micro-supercapacitors for in situ fabricated transferable and wearable energy storage via multi-material 3D printing. *Journal of Power Sources, 403*, 109-117.

Zhang, Y. Q., Xia, X. H., Tu, J. P., Mai, Y. J., Shi, S. J., Wang, X. L., & Gu, C. D. (2012). Self-assembled synthesis of hierarchically porous NiO film and its application for electrochemical capacitors. *Journal of Power Sources, 199*, 413-417.

Zhao, B., Song, J., Liu, P., Xu, W., Fang, T., Jiao, Z., . . . Jiang, Y. (2011). Monolayer graphene/NiO nanosheets with two-dimension structure for supercapacitors. *Journal of Materials Chemistry, 21*(46), 18792-18798.

Zhao, G.-Y., & Li, H.-L. (2008). Preparation of polyaniline nanowire arrayed electrodes for electrochemical supercapacitors. *Microporous and Mesoporous Materials, 110*(2), 590-594.

Zheng, H., Tang, F., Jia, Y., Wang, L., Chen, Y., Lim, M., . . . Lu, G. (2009a). Layer-by-layer assembly and electrochemical properties of sandwiched film of manganese oxide nanosheet and carbon nanotube. *Carbon, 47*(6), 1534-1542.

Zheng, Y.-z., Ding, H.-y., & Zhang, M.-l. (2009b). Preparation and electrochemical properties of nickel oxide as a supercapacitor electrode material. *Materials Research Bulletin, 44*(2), 403-407.

Zhou, M., Chai, H., Jia, D., & Zhou, W. (2014a). The glucose-assisted synthesis of a graphene nanosheet-NiO composite for high-performance supercapacitors. *New Journal of Chemistry, 38*(6), 2320-2326.

Zhou, Y.-k., He, B.-l., Zhou, W.-j., Huang, J., Li, X.-h., Wu, B., & Li, H.-l. (2004). Electrochemical capacitance of well-coated single-walled carbon nanotube with polyaniline composites. *Electrochimica Acta, 49*(2), 257-262.

Zhou, Z., Zhang, X., Lu, C., Lan, L., & Yuan, G. (2014b). Polyaniline-decorated cellulose aerogel nanocomposite with strong interfacial adhesion and enhanced photocatalytic activity. *RSC Advances, 4*(18), 8966-8972.

Zou, Z., Zhou, W., Zhang, Y., Yu, H., Hu, C., & Xiao, W. (2019). High-performance flexible all-solid-state supercapacitor constructed by free-standing cellulose/reduced graphene oxide/silver nanoparticles composite film. *Chemical Engineering Journal, 357*, 45-55.

LIST OF PUBLICATIONS

Razali, S. A., & Majid, S. R. (2018). Electrochemical performance of binder-free NiO-PANI on etched carbon cloth as active electrode material for supercapacitor. *Materials & Design*, 153, 24-35.

Razali, S. A., Rusi, & Majid, S. R. (2018). Fabrication of polyaniline nanorods on electro-etched carbon cloth and its electrochemical activities as electrode materials. *Ionics*, *25*(6), 2575-2584.